A Phase Field Model for the Gallium Permeation of Aluminum Grain Boundaries

by

Raghav Aggarwal

Submitted to the Department of Mechanical Engineering
in partial fulfillment of the requirements for the degree of

Doctor of Science in Mechanical Engineering

at the

MASSACHUSETTS INSTITUTE OF TECHNOLOGY

February 2018

Signature redacted

Author .....
Department of Mechanical Engineering
Jan 20, 2018

Certified by ..... Signature redacted
Michael J. Demkowicz
Associate Professor
Thesis Supervisor

Certified by ..... Signature redacted .....
Youssef M. Marzouk
Associate Professor
Thesis Supervisor

Accepted by ..... Signature redacted
Rohan Abeyaratne
Chairman, Department Committee on Graduate Theses

A Phase Field Model for the Gallium Permeation of Aluminum Grain Boundaries

by

Raghav Aggarwal

Submitted to the Department of Mechanical Engineering
on Jan 20, 2018, in partial fulfillment of the
requirements for the degree of
Doctor of Science in Mechanical Engineering

Abstract

Interfaces, such as grain boundaries, solid-liquid interfaces and solid-solid heterophase interfaces, are important features found in materials. Material properties such as fracture toughness, corrosion susceptibility and high temperature creep are influenced by grain boundary physics. The structure of grain boundaries affects their properties. In this thesis, we have developed a predictive model for a particular grain boundary structure-property relationship: the permeation of liquid gallium through aluminum grain boundaries.

Liquid gallium is known to permeate through aluminum grain boundaries. The reduction in interface energy by the replacement of one Al-Al grain boundary interface with two Al-Ga interfaces drives the permeation. The speed of permeation depends on factors which affect the Al-Al grain boundary energy, such as grain boundary crystallography, applied stress, and temperature. Literature suggests two major hypotheses for the permeation mechanism: front propagation, and diffusion and coalescence.

We have used phase field methods to develop a predictive model for the permeation of gallium through individual aluminum grain boundaries. The model uses location dependent grain boundary energy (LDGBE) distributions for aluminum grain boundaries to predict permeation velocities. Importantly, by changing the model's parameters, its behavior can be adjusted smoothly from front propagation, to diffusion and coalescence.

We have used experimental data collected by Hugo and Hoagland, along with LDGBE maps computed by our collaborators, to infer the parameters of the phase field model. The inference has been done in a Bayesian framework, which gives us estimates of the model parameters with quantifiable uncertainty.

The inferred model parameters strongly support the front propagation hypothesis. We discuss the implications of this inference and potential limitations of our methodology.

Thesis Supervisor: Michael J. Demkowicz

Title: Associate Professor of Materials Science and Engineering, TAMU

Thesis Supervisor: Youssef M. Marzouk
Title: Associate Professor of Aeronautics and Astronautics, MIT

Acknowledgments

I would like to thank my advisers, Prof. Michael J. Demkowicz and Prof. Youssef M. Marzouk for their guidance through my PhD.

I would like to acknowledge my committee members, Prof. Nicolas G. Hadjiconstantinou and Prof. Alexie M. Kolpak for the helpful comments and recommendations I received from them in my committee meetings.

I would like to acknowledge my collaborators, Dr. Richard C. Hugo and Dr. Sanket S. Navale. Dr. Hugo provided us with valuable unpublished transmission electron microscopy data from his research study, which we built this study on top of. He was also kind enough to take the time out to discuss my calculation of grain boundary crystallography from his data over the phone. Sanket and I started out PhD's together in the fall of 2012, in the Demkowicz group. He played an invaluable role in calculating location dependent grain boundary energy maps for this study.

I would also like to thank two other lab mates, Dr. Dina Yuryev and Dr. Abishek Kashinath. Dina introduced me to the software library `MOOSE`, helped me get started with it, and pointed me in the correct direction whenever I was stuck on something. Abishek was a good friend and a mentor in the lab.

I could not have finished this journey without the support of my family and friends. My parents, Chaitanya Aggarwal and Veena Aggarwal, and my sister Kaveri Aggarwal have been incredibly supportive in these last five years. In this time, I have visited my home in India twice; my family has always been supportive and understanding. My friends in the Boston area have been my family away from family. They never let me feel homesick.

I would like to thank my girlfriend, Ariel Shapiro, for being so incredibly loving, kind, patient, and supportive as I worked on finishing my research and thesis. She has been my bedrock, and my source of resilience in this last year.

I would like to acknowledge my funding sources. This project was funded by the Department of Energy, Office of Science. I would also like to acknowledge the developers behind `MOOSE`, for developing an incredibly functional and useful software

library, and providing it to the world free of charge.

Contents

List of Figures

List of Tables

Chapter 1

Introduction

Materials of engineering importance, such as steel, aluminum and many ceramics, are polycrystalline in nature [43]. Their bulk is composed of many individual crystals, or grains, with grain boundaries at the interface between individual grains. These grain boundaries are interconnected and form a grain boundary network. Grain boundaries are a planar interface between two crystalline grains. They can be described by the misoriention of two grains, and the orientation of grain boundary plane. Collectively, the grain misorientation and grain boundary plane orientation describe grain boundary crystallography.

Grain boundary crystallography strongly affects grain boundary structure and properties. For instance, the fracture toughness of molybdenum [38] and zinc [67] grain boundaries have been shown to be strongly dependent on the misorientation of the grain boundary. Further, the properties of bulk polycrystals depend on distribution of grain boundaries within the grain boundary network. These properties can be controlled by controlling the grain boundary character distribution (GBCD). Lim and Wantanabe have shown that the toughness of 3-D grain boundary networks can be improved by increasing the relative frequency of fracture resitant grain boundaries, and above a certain critical frequency, the network transitions from brittle to ductile failure [41]. Further, Wantanabe *et al.* have shown that it is possible to *engineer* the ductility of Fe-6.5%mass Si alloy by controlling the GBCD [66]. Other examples of material properties controlled by grain boundary structure-property relationships

include creep [40] and hydrogen embrittlement [5].

In order to engineer polycrystalline materials, we need predictive models of grain boundary structure-property relationships. In this thesis, we develop a predictive model for a particular grain boundary structure-property relationship: the permeation of liquid gallium through aluminum grain boundaries, with the aim to developing techniques which are broadly applicable. This is a good model problem to study as:

1. Gallium permeation of aluminum has all the characteristics of a multi-scale grain boundary physics problem. The permeation velocity through individual grain boundaries is a function of the grain boundary crystallography and structure. The permeation rates of gallium through a bulk aluminum samples are dependent of the distribution of grain boundaries within the sample.

2. It is a well studied problem, both experimentally [28, 29, 30, 57, 42, 63, 51, 52, 17] and through simulation [44, 45, 46]. Experimentally, gallium permeation of aluminum has been studied at the individual grain boundary scale, as well as the grain boundary network scale. As a result, there is existing published data for the inference of model parameters.

In chapter 2, we have review the existing literature on gallium permeation of aluminum. In chapter 3, we develop a phase field model approach to simulating the gallium permeation of aluminum. We show that the Cahn-Hilliard equation can In chapter 4

We have used phase field methods to simulate the permeation of gallium through individual aluminum grain boundaries. Our model uses location dependent grain boundary energy (LDGBE) distributions as an input, and predicts permeation velocity. We have used the data set collected by Hugo and Hoagland [30], along with LDGBE distributions calculated by our collaborators, to infer model parameter of the phase field model in a Bayesian framework [60].

Chapter 2

Literature review

2.1 Grain boundary crystallography and structure

Grain boundaries are formed at the interface between two grains. They can be characterized by the amount of misorientation between the two grains that form them, as well as the orientation of the grain boundary plane. To characterize the crystallography of an arbitrary grain boundary, a total of five degrees of freedom are needed [31]. This can be visualized in the cartoon depicting the construction of a grain boundary shown in figure 2-1. To construct the grain boundary, we start with two identical grains, and rotate one of them with respect to the other. This arbitrary three dimensional rotation g_{AB} is defined by three degrees of freedom. These three degrees of freedom can either be parameterized as three Euler angles, or as an axis of rotation and an angle. The angle is referred to as the misorientation angle θ. Then, both grains are cut along a common plane, and fused to form the grain boundary. The common plane, defined by its normal unit vector $\hat{n}$, has two degrees of freedom associated with it.

Grain boundaries can have complex structure, which influences their properties. Figure 2-2 shows the structure of a low angle twist boundary. The grain boundary surface is composed of coherent patches, which are regions of good atomic fit, and misfit dislocations. The coherent patches have low surface energy, whereas the misfit dislocations have high surface energy. The nature and spacing of misfit dislocations

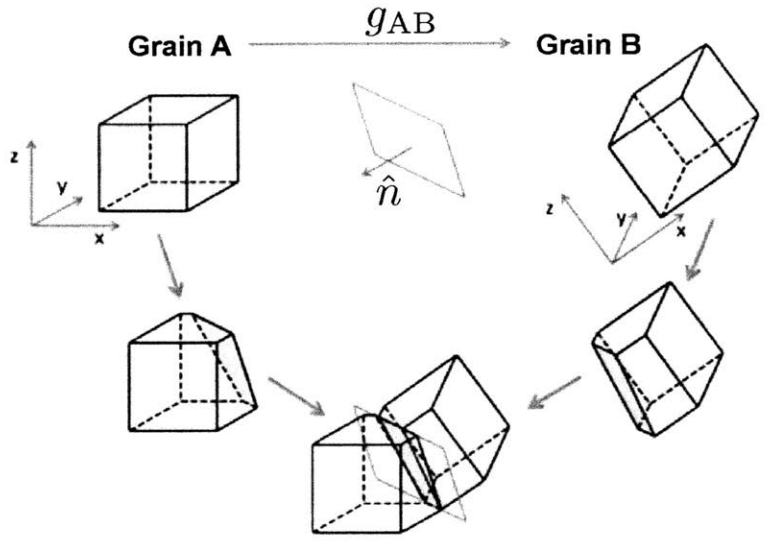

Figure 2-1: The construction of an arbitrary grain boundary. The first grain, shown on the left, is rotated through an arbitrary rotation g_{AB} to obtain the second grain, shown on the right. This arbitrary rotation in three dimensional space is characterized by three parameters. Both grains are cut along a common plane $\hat{n}$ and fused together to form the grain boundary. Image credit: Michael J. Demkowicz (Unpublished)

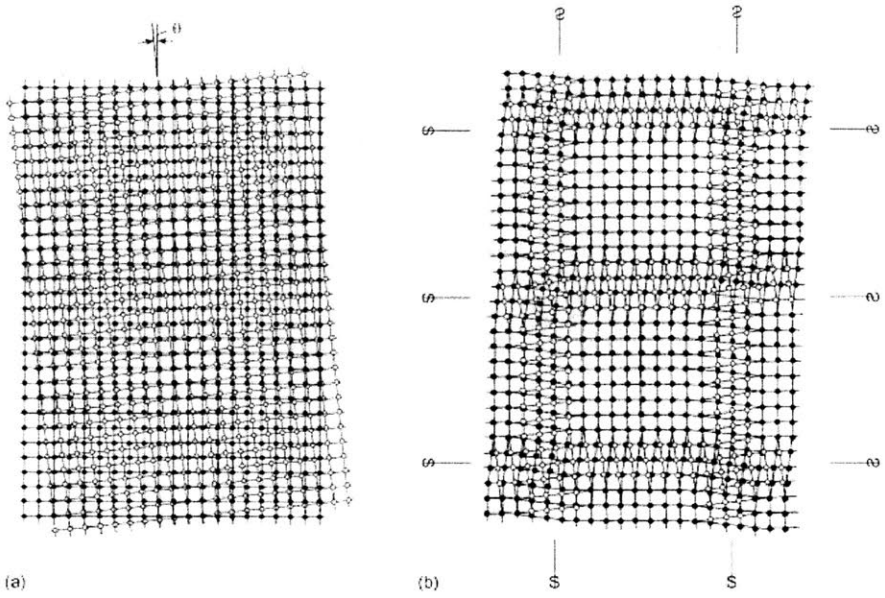

Figure 2-2: The structure of a low angle twist boundary. The grain boundary is being viewed normal to its plane. The superimposed atoms on the left 'snap' into a low energy configuration shown on the right. The structure is composed of coherent patches, which have good atomic fit, separated by misfit dislocations. In the case of this boundary, the dislocations are of screw type. [31]

depends on the crystallography of the grain boundary. A study of the relationship between grain boundary crystallography and grain boundary structure can be found in [10]

2.2 Gallium permeation of aluminum

2.2.1 Computational studies

Computations studies of gallium permeation can complement experimental studies by overcoming the two key limitations: The lack of atomic resolutions and difficulty in controlling factors such as stress, grain boundary crystallography, strain rate etc. Computational studies are performed using a family of techniques known as molecular dynamics (MD) [1, 25]. In molecular dynamics, the positions and velocities of atoms are solved for using newton's laws of motion. The forces on the individual atoms are calculated using potential functions. Since both the positions and velocities of

the atoms are available at all simulation time steps, quantities such as stress, strain, temperature can be calculated. By imposing the right boundary conditions and initial conditions, stresses, strains, temperatures etc can be imposed. MD studies have been used to study the dependence of gallium permeation on factors such as stress, temperature, grain size [44, 45] and strain rate [46].

Nam and Srolovitz studied the permeation of gallium through a symmetric tilt grain boundary in aluminum [44]. The simulation cell had a volume of $40nm \times 66nm \times 2nm$, which corresponded to $\sim 350,000$ atoms. The simulations ran for $\sim 70ns$. The simulations were performed at high temperature ($600K$) and high elastic strains (0.65%, 1.3%), which corresponded to stresses of 250 Mpa and 500 Mpa in the bulk respectively. These high elastic strains and temperatures were necessary to obtain gallium permeation speeds that were large enough to be observed in the simulation time of $\sim 70ns$.

The researchers noted an increase in permeation speed with an increase in the applied stress. They also noted that the permeation speed was constant only for grain boundaries with high applied stress, and reduced with increasing permeation distance for grain boundaries with no applied stress. They investigated several mechanisms to explain this observation, such as increased solubility of aluminum in gallium, increased gallium diffusion in grain boundaries and gallium segregation to grain boundaries at high stress. None of these factors were found to explain the increase in permeation speed with stress. The researchers then investigated the distribution of stresses within the grain boundary, and noticed the presence of dislocations which climbed at a constant speed in the simulations with high applied stress. These dislocations were not present for the simulations with no applied stress.

In another study, Nam and Srolovitz studied the effect of stress, grain boundary crystallography, grain size and temperature on the permeation speed of gallium [45]. The researchers observed a dramatic increase in permeation speeds with increasing grain size. Doubling the grain size from $33nm$ to $66nm$ doubled the permeation speed for the same amount of applied stress. Increased grain size also reduced the critical stress needed to observe time independent permeation speeds.

The observations made by Nam and Srolovitz in these two studies are consistent with the experimental results of Hugo and Hoagland [30]. Both the studies observed permeation of gallium through aluminum at constant, time independent speeds. The speeds observed by Hugo and Hoagland ($\sim 1 - 10\mu m/s$) were 5 orders of magnitude slower than those observed by Nam and Srolovitz ($\sim 0.1m/s$). This difference can be attributed to the much higher temperature and stresses that Nam and Srolovitz performed their study at. Both studies support a dislocation climb model to explain permeation. Nam and Srolovitz observed that gallium permeated aluminum at speeds which reduced with time for simulations with no applied stress. Although no external stresses were applied by Hugo and Hoagland on their samples, small residual stresses of the order of a few Mpa from sample processing could have been enough to ensure time independent permeation speeds. This reduction in critical stress can be attributed to the much larger grain sizes that Hugo and Hoagland observed ($\sim 10\mu m$) as compared to the grains simulated by Nam and Srolovitz ($33nm$ and $66nm$)

MD studies can give deep insight into the atomic mechanism behind gallium permeation. However, they are limited by computational considerations. The largest length scales that can be simulated using MD are of the order of $10nm$, which makes the study of permeation through grain boundary networks infeasible. Additionally, simulations have to be performed at high temperatures and stresses to enable observation of permeation in a reasonable simulation time. This makes it infeasible to study permeation at room temperature, although insights gained from high temperature and stress studies can be used to explain qualitative trends observed in experimental studies at low temperatures and stresses.

2.2.2 Experimental studies

Gallium permeation of aluminum has been studied extensively using experimental methods such as transmission electron microscopy [28, 29, 30], X-ray microtomography [42] and microradiography [49, 51, 52, 50], and optical microscopy [63]. Gallium permeation of aluminum is amenable to easy experimental study due to a number of factors. The permeation speeds are fast, allowing for experiments which are

not long. Because gallium melts at $29.7°C$, experiments can be performed at relatively low temperatures, allowing for simple experimental setups. Experiments can be broadly classified into macroscopic and microscopic experiments. Macroscopic experiments observe permeation at the length scale of multiple grain boundaries to entire grain boundary networks, while microscopic experiments can resolve the permeation through individual grain boundaries. We will discuss a subset of the experimental studies performed on the gallium-aluminum permeation system, and the insight they have produced.

Hugo and Hoagland have studied the relationship between permeation speed of gallium and the structure of aluminum grain boundaries using transmission electron microscopy (TEM) and atomistic simulations [28, 29, 30]. They studied the permeation velocity of gallium through 40 grain boundaries, all of which had their crystallography measured using TEM Kikuchi diffraction patterns. The researchers correlated the grain boundary permeation speeds with four characteristics of the grain boundaries; Σ value, misorientation angle θ, average grain boundary energy γ_{gbm}, and grain boundary excess volume V^E. The Σ value and θ were calculated from grain boundary crystallography obtained from the Kikuchi diffraction patterns. To calculate γ_{gbm} and V^E, atomic models of the grain boundaries were constructed using molecular statics.

For each of the four characteristics studied, the researchers found similar correlations. Low values of Σ, θ, γ_{gbm}, and V^E correlated with low permeation speeds or no permeation at all. However, large values of the characteristics did not imply fast permeation. This can be seen in figure 2-3, where many grain boundaries with large value of V^E were permeated slowly.

To explain this lack of correlation at large values of Σ, θ, γ_{gbm}, and V^E, the researchers looked into the distribution of voids in the grain boundaries, instead of just an aggregate excess volume. The distribution of voids in the grain boundary surface was identified through the inter-atomic spacing in the atomic model of the grain boundary. The grain boundary surfaces were segregated into voids and regions with good 'fit'. One such distribution can be seen in figure 2-4. The researchers

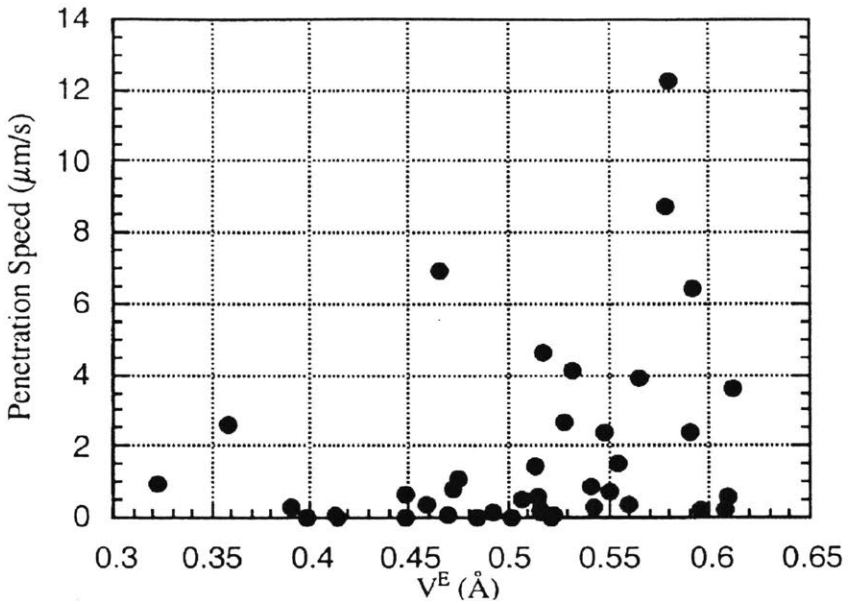

Figure 2-3: The relationship between permeation velocity and grain boundary excess volume V^E [30]. It can be seen that low values of V^E results in slow permeation. However, large values of V^E do not always result in fast permeation.

found a qualitative correlation between the distribution of voids in grain boundaries and permeation speed of gallium. They found that gallium permeated rapidly through grain boundaries which had large voids and no ordered regions, and slowly through grain boundaries with small voids which were not connected. This suggests that the voids acted as a passage through which the gallium flowed. However, it was found that 'fit-misfit' grain boundaries, or gain boundaries which had both regions of good fit as well as voids, were also permeated slowly. This suggested that the rate limiting step was the presence of regions of good fit. These regions acted as obstacles to the flow of gallium. The researchers concluded that the gallium does not diffuse through aluminum as individual atoms. Instead, the gallium front acts as a line defect, similar to a climbing edge dislocation. The gallium front has a line tension, and can get pinned at the obstacles formed by fit regions, despite the presence of void channels.

Pereiro Lopez *et al.* studied gallium permeation through aluminum polycrystals using synchrotron radiation X-ray microradiography [51]. By exploiting the large difference in X-ray attenuation coefficients of gallium and aluminum, the researchers

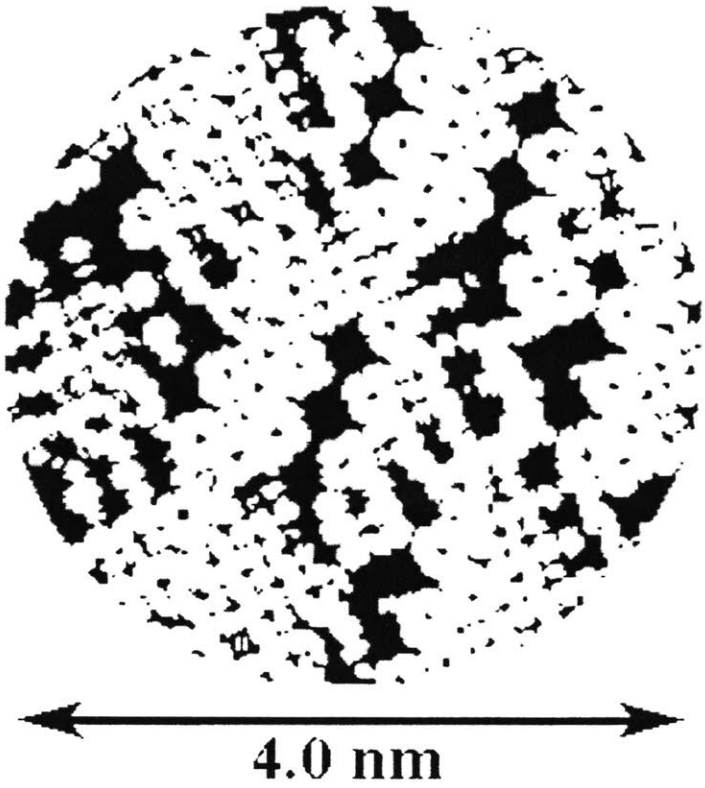

Figure 2-4: The distribution of voids within a grain boundary. The voids are depicted in black, and the remaining white areas are areas of good atomic fit. Image from [30]

were able to calculate the thickness of the gallium layer between the aluminum grains as a function of time. The researchers observed a monotonic growth in the thickness of the gallium layer, which could be divided into 3 phases. In the first phase, gallium films penetrated certain grain boundaries and simultaneously grew in thickness, up to a few hundred nanometers. In the second phase, the gallium film thickness along percolation pathways increased rapidly. In the final phase, the gallium film saturated at thicknesses up to a few microns. The researchers hypothesized that the sudden increase in gallium thickness is due to cracking of the sample, followed by rapid flow of gallium into the crack due to capillary action. The cracking is driven by internal stresses due elastic incompatibility of the individual grains as well as external stresses due to clamping. The weakening of grain boundaries due to gallium permeation allows even small stresses to cause cracks.

To investigate the sensitivity of the gallium permeation process to stresses, the researchers compared results from two different clamping methods. The samples were either 'gently screwed together' between two metallic plates, or were fixed using silver paint. The first method gave rise to higher stresses. The researchers observed a larger probability of permeation in samples that were screwed together (11 out of 16 samples), as compared to samples fixed using paint (1 out of 6 samples). Although the amount of applied stress was not quantified, it still demonstrated the sensitivity of the permeation process to small applied stresses.

Tanaka *et al.* observed the permeation of gallium through thin aluminum sheets using optical and atomic force microscopy [63]. The films were fabricated through vacuum deposition on glass plates, and were between $100nm$ to $1000nm$ in thickness. The size of individual grains was estimated to be on the order of the thickness of the films. Some of the films had been annealed, and the grains in these films were expected to be larger than those in the non-annealed samples. However, no direct characterization of grain size was performed. Gallium was introduced to the aluminum samples by placing a small drop of known weight in the center of sample held on a heating element.

The researchers observed two distinct effects. They observed a spider web like

network through which the gallium permeated the aluminum samples. This network extended out radially from the location of the gallium drop. Atomic force microscopy of the sample showed the surface of the sample was raised along this permeation network. Additionally, they noted a radially expanding region of the aluminum sample which had lost its metallic luster, again originating from the gallium drop. The speed at which both these regions grew were characterized under controlled conditions of film thickness, temperature and size of the gallium drop.

Although this study could not collect data at the scale of individual grain boundaries, the researchers were nevertheless able to observe some interesting aspects of gallium permeation in a grain boundary network. The permeation process took place in two phases. In the first phase, the web like permeation network and the dull region grew at the same speed. The speeds were between $2.3\mu m/s$ and $9.1\mu m/s$. In the second phase, the web like network stopped growing, but the the dull region continued to grow at a lower speed of $.83\mu m/s$. The speed of growth of the dull region in the second phase was unaffected by experimental parameters such as temperature, film thickness and quantity of gallium. The rate of growth of the web like network and the dull region during the first phase increased with an increasing in both temperature and film thickness. The annealed samples had slower speed of permeation in the first phase as compared to the non-annealed samples. The size that the web like network grew to before it stopped growing increased with an increase in size of the gallium drop, suggesting that this size was limited by the amount of gallium available.

As we have seen, experiments can be performed at a variety of length scales on the gallium aluminum system, ranging form $10^{-6}m$ to $10^{-3}m$. Some of these experiments have pointed towards particular mechanisms for gallium permeation, such as edge dislocation climb [30] and cracking induced by internal and external stresses [51]. However, experimental studies have their limitations. The smallest length scales at which *in-situ* permeation of gallium can be observed are of the order of $10^{-6}m$, making it difficult to study the atomic mechanisms behind gallium permeation. Although the amount of stress in experimental samples can be qualitatively controlled using different clamping mechanisms, quantification of the exact stress at individual grain

boundaries can be difficult due to the presence of internal stresses from material processing. This makes it difficult to study the relationship between permeation speeds and grain boundary stress.

Chapter 3

Phase field methods

Phase field methods are a class of computational methods which are used to simulate multi-phase physics [55]. Phase field methods simplify the treatment of multi-phase physics by representing the spatial distribution of the phases with an auxiliary scalar field called the order parameter field $\phi(\mathbf{x})$. The order parameter field $\phi(\mathbf{x})$ can have values within a range, say $[-1, 1]$, for all points $\mathbf{x}$. The extreme values of $\phi(\mathbf{x})$ represent regions of pure phase, and intermediate value represent the interface between the two phases. The order parameter field simplifies the simulation of multi-phase physics by eliminating the need to track moving boundaries between phases.

Phase field methods have been used extensively in the field of materials science. They have been to simulation the solidification of pure metals [36, 35, 11], solidification of alloys [65, 7, 8], and grain growth [21, 20, 37]. For a review of the use of phase field models in materials science, see [16].

In section 3.1, we discuss the order parameter field and the energy functional, and what parameters control their behavior. We derive two equations of evolution of the order parameter field in section 3.2. In section 3.3, we show the simulation of spinodal decomposition with the Cahn-Hilliard equation. This simulation shows us the salient features of the phase interface described by the Cahn-Hilliard equation; the interface thickness and the interface tension. In section 3.4, we see how the parameters of the energy functional control the interface thickness and interface tension.

3.1 Order parameter field and the energy functional

Figure 3-1 shows an example order parameter field. The scalar field $\phi(\mathbf{x}), \mathbf{x} \in \Omega$ shows the spatial arrangement of two phases, say A and B. The spatial domain can be partitioned into three sets,

$$\Omega_A = \{\mathbf{x} | \phi(\mathbf{x}) = 1\}, \tag{3.1}$$

$$\Omega_B = \{\mathbf{x} | \phi(\mathbf{x}) = -1\}, \tag{3.2}$$

$$\Omega_I = \{\mathbf{x} | -1 < \phi(\mathbf{x}) < 1\}. \tag{3.3}$$

Ω_A and Ω_B are regions which contain pure phases A and B respectively. These regions are shown in figure 3-1 as the white and black regions respectively. Ω_I contains all regions which are part of the interface between phase A and phase B. In figure 3-1, these are all the regions which are of a shade of gray.

The order parameter field implicitly encodes topological information about the distribution of the phases. For instance, in figure 3-1, we can multiple topological features. There is an island of phase A, centered at $(x, y) = (50, 50)$, surrounded by phase B. Also, there is a curvilinear interface between phase B to the left and phase A to the right. The order parameter field does not need any additional book keeping to encode this information. This is especially beneficial, since topological *changes* no longer need to be tracked. Events such as mergers, splits, precipitation etc are handled implicitly by the order parameter field.

The behavior of the two phases represented by the order parameter field $\phi(\mathbf{x})$ is governed by an associated energy functional

$$E(\phi) = \int_{\Omega} \left(g\left(\phi\left(\mathbf{x}\right)\right) + \frac{\epsilon}{2} \nabla\phi(\mathbf{x}).\nabla\phi(\mathbf{x}) \right) d\mathbf{x}, \quad \epsilon > 0. \tag{3.4}$$

The energy functional is composed of two components: A potential function $g(\phi)$ and a gradient penalty term $\epsilon\nabla\phi.\nabla\phi/2$.

The potential function dictates the relative energetic favorability of the different phases represented by $\phi(\mathbf{x})$. A double well potential, shown in figure 3-2 is a commonly

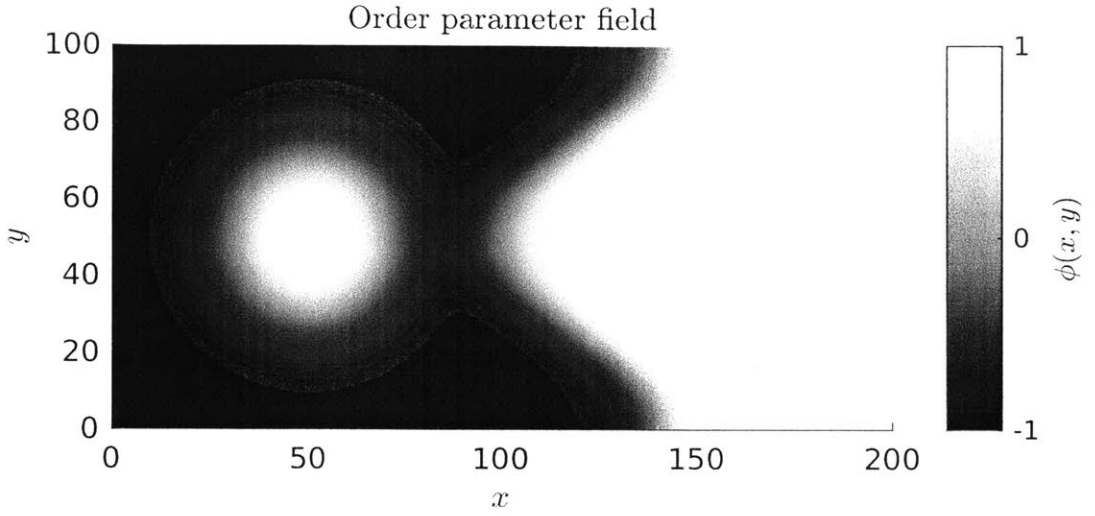

Figure 3-1: An example of an order parameter field $\phi(\mathbf{x})$. The order parameter varies between -1 and 1 at all location.The order parameter field partitions the spatial domain into regions of pure phase ($\phi(\mathbf{x}) = \pm 1$), and the interfaces between them ($-1 < \phi(\mathbf{x}) < 1$)).

used potential function. This potential function has two energy wells situated at $\phi = \pm 1$, separated by an energy barrier. 4^{th} order polynomial are commonly used to construct double well potentials. The potential shown in figure 3-2 is

$$g(\phi) = \frac{\phi^4}{4} - \frac{\phi^2}{2} + \frac{1}{4}. \tag{3.5}$$

This potential function has two minima at $\phi = \pm 1$ and a maximum at $\phi = 0$. As a result, the potential function penalizes phase mixing, and favors phase separation. The magnitude of the penalty for phase mixing can be controlled by the size of the energy barrier between the two phases. A measure of the size of the barrier is area between the potential function and the common tangent between the two wells, calculated as

$$\alpha = \int_{\phi_1}^{\phi_2} [g(\phi) - l(\phi)]\, d\phi. \tag{3.6}$$

where $l(\phi)$ is the common tangent, and ϕ_1 and ϕ_2 are the points of common tangency. For the potential shown in equation 3.5, the value of $\alpha = 4/15$.

The term $\epsilon \nabla\phi.\nabla\phi/2$ penalizes sharp gradients in the order parameter field. Larger

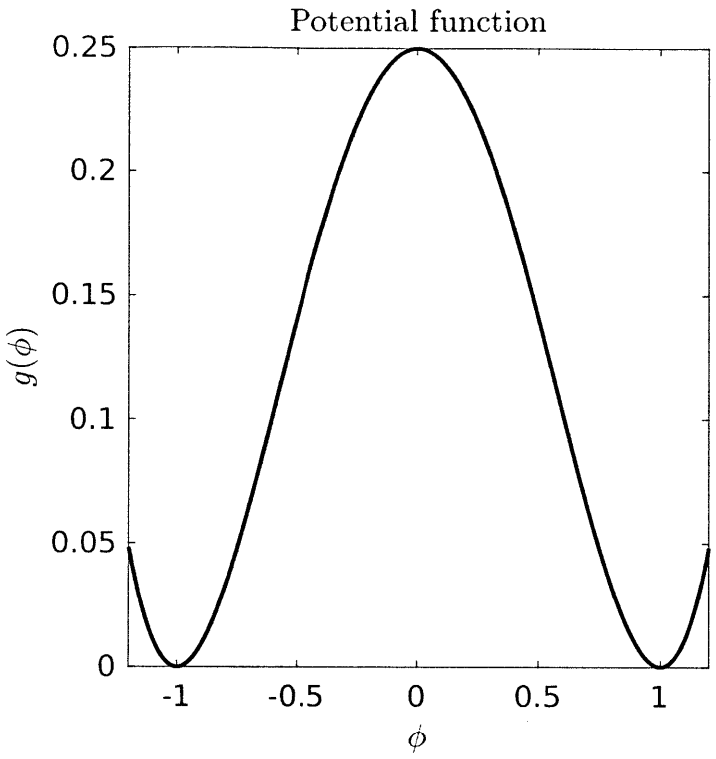

Figure 3-2: Double well potential function. The function $g(\phi)$ is a 4^{th} order polynomial with minima at $\phi = \pm 1$ and a maximum at $\phi = 0$.

values of ϵ produce a larger gradient penalty, which in turn produces a smoother order parameter field.

3.2 Equations of evolution of order parameter field

To derive the equations of evolution of the order parameter field, we first define a chemical potential μ, which is the variational derivative of the energy functional E with respect to the order parameter field ϕ, given by the relation

$$\int_{\Omega} \frac{\delta E}{\delta \phi} \zeta d\mathbf{X} = \lim_{\eta \to 0} \frac{E(\phi + \eta\zeta) - E(\phi)}{\eta}, \tag{3.7}$$

where $\delta E/\delta\phi$ is the variational derivative, and ζ is an arbitrary function. We can calculate the functional derivative by calculating $E(\phi+\eta\zeta)$.

$$\begin{aligned} E(\phi+\eta\zeta) &= \int_{\Omega}\left(g(\phi+\eta\zeta)+\frac{\epsilon}{2}\nabla(\phi+\eta\zeta).\nabla(\phi+\eta\zeta)\right)d\mathbf{x} \\ &= \int_{\Omega}\left(g(\phi)+\eta\zeta\frac{\partial g}{\partial\phi}+\frac{\epsilon}{2}\nabla\phi.\nabla\phi+\epsilon\eta\nabla\phi.\nabla\zeta+\cancel{\frac{\epsilon}{2}\eta^2\nabla\zeta.\nabla\zeta}\right)d\mathbf{x}. \\ &= E(\phi)+\eta\int_{\Omega}\left(\zeta\frac{\partial g}{\partial\phi}+\epsilon\nabla\phi.\nabla\zeta\right)d\mathbf{x} \end{aligned} \tag{3.8}$$

By using the divergence theorem on the term $\int_{\Omega}\epsilon\nabla\phi.\nabla\zeta d\mathbf{x}$, we get

$$E(\phi+\eta\zeta)=E(\phi)+\eta\left[\int_{\Omega}\zeta\left(\frac{\partial g}{\partial\phi}-\epsilon\nabla^2\phi\right)d\mathbf{x}+\cancel{\oint_{\partial\Omega}\epsilon\zeta(\nabla\phi.\hat{n})ds}\right]. \tag{3.9}$$

Here, $\partial\Omega$ is the boundary of the computational domain Ω, and $\hat{n}$ is the outward normal vector. The surface integral $\oint_{\partial\Omega}\epsilon\zeta(\nabla\phi\cdot\hat{n})ds=0$ when either the Dirichlet or the Neumann boundary conditions are applied to $\phi(\mathbf{x},t)$. This is because applying the Dirichlet boundary condition enforces

$$\zeta=0 \qquad \forall\mathbf{x}\in\partial\Omega, \tag{3.10}$$

and the Neumann boundary condition enforces

$$\nabla\phi\cdot\hat{n}=0 \qquad \forall\mathbf{x}\in\partial\Omega. \tag{3.11}$$

We can thus calculate the limit

$$\lim_{\eta\to0}\frac{E(\phi+\eta\zeta)-E(\phi)}{\eta}=\int_{\Omega}\zeta\left(\frac{\partial g}{\partial\phi}-\epsilon\nabla^2\phi\right)d\mathbf{x}. \tag{3.12}$$

By comparing equations 3.7 and 3.12, we get

$$\mu=\frac{\delta E}{\delta\phi}=\frac{\partial g}{\partial\phi}-\epsilon\nabla^2\phi. \tag{3.13}$$

3.2.1 Allen-Cahn equation for the non-conservative evolution of the order parameter field

The Allen-Cahn equation simulates the non-conservative evolution of the order parameter field $\phi(\mathbf{x}, t)$ [2, 15, 3, 27]. The equation is given by

$$\begin{aligned} \frac{\partial \phi}{\partial t} &= -M\mu \\ &= M\left(\epsilon \nabla^2 \phi - \frac{\partial g}{\partial \phi}\right). \end{aligned} \tag{3.14}$$

We can see that the energy functional $E(\phi)$ decreases monotonically by calculating

$$\begin{aligned} \frac{\partial E}{\partial t} &= \int_{\Omega} \frac{\delta E}{\delta \phi} \frac{\partial \phi}{\partial t} d\mathbf{x} \\ &= \int_{\Omega} -M\mu^2 d\mathbf{x} \\ &\leq 0. \end{aligned} \tag{3.15}$$

3.2.2 Cahn-Hilliard equation for the conservative evolution of the order parameter field

The Cahn-Hilliard equation simulates the conservative evolution of $\phi(\mathbf{x}, t)$ [14, 27, 47, 18]. We first define a flux J

$$J = -M\nabla\mu. \tag{3.16}$$

If ϕ is conserved within then region Ω, then

$$\int_{\Omega} \frac{\partial \phi}{\partial t} d\mathbf{x} + \oint_{\partial\Omega} J \cdot \hat{n} ds = 0. \tag{3.17}$$

Using the divergence theorem, we get

$$\int_{\Omega} \left(\frac{\partial \phi}{\partial t} + \nabla \cdot J\right) d\mathbf{x} = 0. \tag{3.18}$$

Since ϕ is conserved, this equality has to be true for any arbitrary Ω. Therefore,

$$\frac{\partial \phi}{\partial t} + \nabla \cdot J = 0. \tag{3.19}$$

Combining equations 3.13,3.16, and 3.19, we get the Cahn-Hilliard equation

$$\frac{\partial \phi}{\partial t} = \nabla \cdot \left[M \nabla \left(\frac{\partial g}{\partial \phi} - \epsilon \nabla^2 \phi \right) \right] \tag{3.20}$$

The energy functional $E(\phi)$ reduces exponentially under the Cahn-Hilliard equation. The can be seen by calculating

$$\begin{aligned} \frac{dE}{dt} &= \int_{\mathbf{X}} \frac{\delta E}{\delta \phi} \frac{d\phi}{dt} d\mathbf{x} \\ &= \int_{\mathbf{X}} \mu M \Delta \mu d\mathbf{x} \\ &= \cancel{\oint_{\partial \Omega} \mu M (\nabla \mu \cdot \hat{n}) ds} - \int_{\mathbf{X}} M \nabla \mu \cdot \nabla \mu d\mathbf{x} \\ &\leq 0 \end{aligned} \tag{3.21}$$

The surface integral $\oint_{\mathbf{B}} \mu M (\nabla \mu \cdot \hat{n}) ds = 0$ under the Dirichlet condition

$$\mu = 0 \qquad \forall \mathbf{x} \in \partial \Omega, \tag{3.22}$$

and the Neumann condition

$$\nabla \mu \cdot \hat{n} = 0 \qquad \forall \mathbf{x} \in \partial \Omega, \tag{3.23}$$

3.3 Spinodal decomposition: A canonical example of the Cahn-Hilliard equation

Spinodal decomposition is the spontaneous separation of a thermodynamically unstable mixture of two or more immiscible substances [12, 13]. The initial mixing of the two substances can be accomplished by a variety of methods. The substances can be

mixed at elevated temperatures and then quenched, as in the case of metallic alloys [58]. The substances can be dissolved in a common solvent, which is then evaporated, which is a manufacturing technique for organic solar cells [69, 62].

In contrast with a mechanism such as nucleation and growth, there is no thermodynamic barrier to separation in spinodal decomposition [39]. Thus, the dynamics of spinodal decomposition are limited by diffusion. Spinodal decomposition can be numerically simulated using the Cahn-Hilliard equation. We will use spinodal decomposition as a model problem to study the effect the gradient penalty factor ϵ, and the potential barrier α, on the dynamics of the Cahn-Hilliard equation.

We used a spectral method to discretize the Cahn-Hilliard equation in space [64], and Eyre's scheme in time [19]. Figure 3-3 shows four snapshots from a spinodal decomposition simulation performed using the Cahn-Hilliard equation. Figure 3-3(a) shows the order parameter field $\phi(\mathbf{x})$ at time $t = 0$. The order parameter field is initialized with zero mean Gaussian random noise with a small variance ($\sigma^2 = 3e-4$). This small amount of noise is needed to initiate the spinodal decomposition. Periodic boundary conditions are imposed to conserve the total order parameter value.

The spinodal decomposition process is composed of three stages: phase separation, coarsening, and, in the case of finite computational domains, convergence.

Figure 3-3(b) shows the separation of the computational domain into regions of pure phase, separated by diffuse interfaces. The separation of the phases is driven by a reduction in the potential function contribution to the energy functional shown in figure 3.5. This reduction in energy is offset by and increase in the gradient penalty. The balance of reduction in potential function and increase in gradient energy sets the thickness of the interfaces separating the pure phases.

This can be seen clearly in figure 3-4, where the time evolution of the energy functional, as well as the contributions of the potential function and the gradient penalty is shown. From the initial condition at $t = 0$ to the phase separation at $t = 0.003$, there is a reduction in potential function energy, and an increase in the gradient penalty. However, the total energy functional monotonically reduces.

After the phases separate into spinodal regions in figure 3-3(b), the order param-

eter field coarsens in figure 3-3(c). This is energetically favorable, since it reduces the interface length between the two pure phases, which reduces both the potential function and gradient penalty contribution to the energy functional. This can be seen in figure 3-4, where there is a reduction in both the potential function, and the gradient penalty between $t = 0.003$ and $t = 0.02$.

Finally figure 3-3(d) shows the convergence of the order parameter field. At convergence, a circular distribution of phase $\phi = 1$ minimizes the interface length, thereby minimizing the energy functional $E(\phi)$.

Through this simulation, we can conclude that the phase interface has two defining attributes. The first is the thickness δ. As we observed in figure 3-4, the phases separate from a mixed state due to a reduction in potential energy. The phases continue to separate, and the interface between them continues to sharpen, until any further reduction in potential energy is offset by the increase in gradient penalty. Hence the thickness δ of the interfaces is controlled by a balance between the potential energy and gradient penalty.

The second attribute is an interfacial tension τ. The interface between the pure phases behaves like a taut string. This is because of the fact that a decrease in the length of the interface has a corresponding energy reduction. The energy reduction comes from a reduction in *both* the potential energy, as well as the gradient penalty. This can be seen in figure 3-4 from $t = 0.003$ to convergence, where the reduction in total energy functional is caused by a reduction in both the potential energy and the gradient penalty.

Hence we can see that the values of interface thickness δ and the interface tension τ are dictated by the potential function and the gradient penalty, which are in turn controlled by the parameters α and ϵ. In the next section, we will calculate the functional dependence $\delta = \delta(\alpha, \epsilon)$ and $\tau = \tau(\alpha, \epsilon)$.

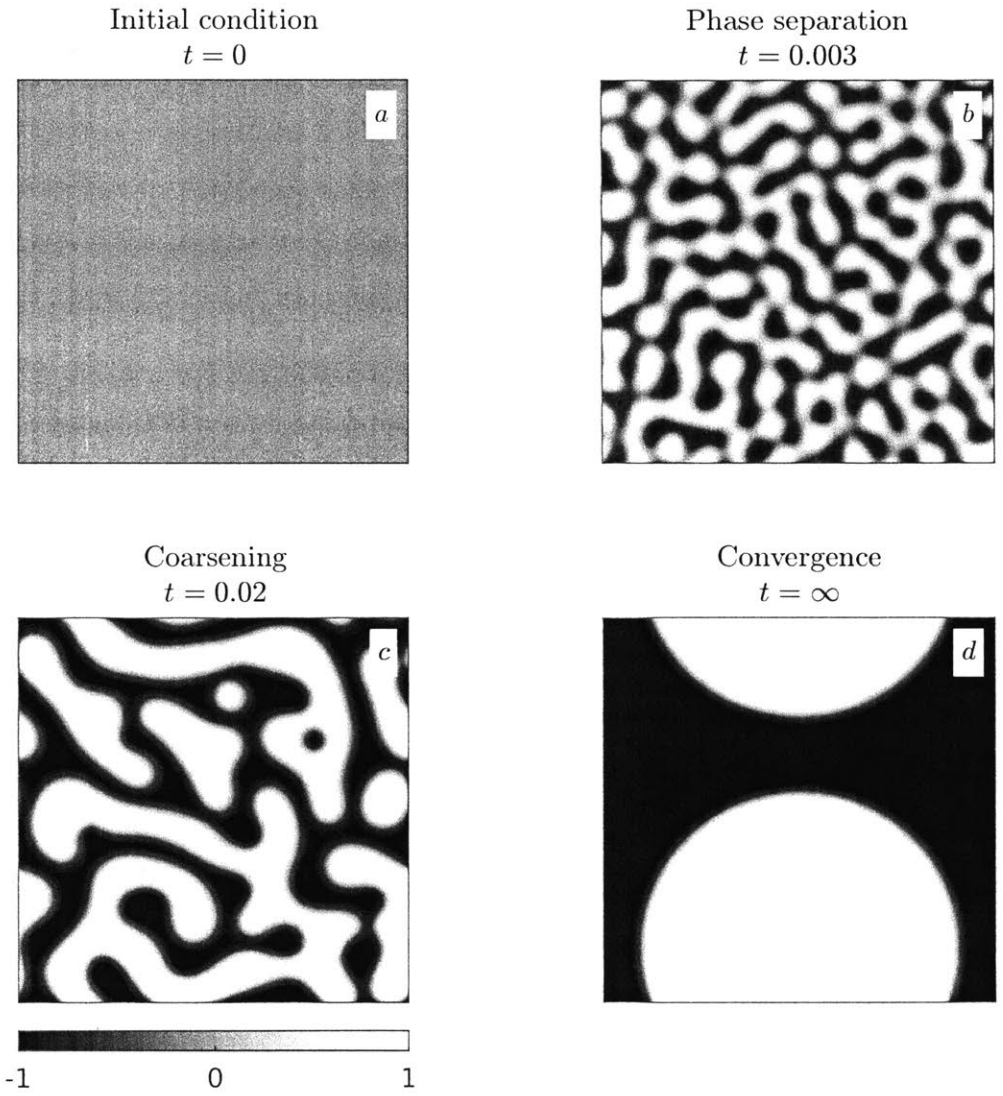

Figure 3-3: Montage showing various stages of spinodal decomposition. (a) Initial condition: the order parameter field is initialized with zero-mean Gaussian noise with variance $\sigma^2 = 3e-4$. (b) Phase separation: the order parameter field phase separates into regions of pure phase which are separated by diffuse interfaces. (c) Coarsening: phase coarsen as this reduces the total interface length, which reduces the value of the energy functional. (d) Convergence: the order parameter field converges to a form which minimizes interface length.

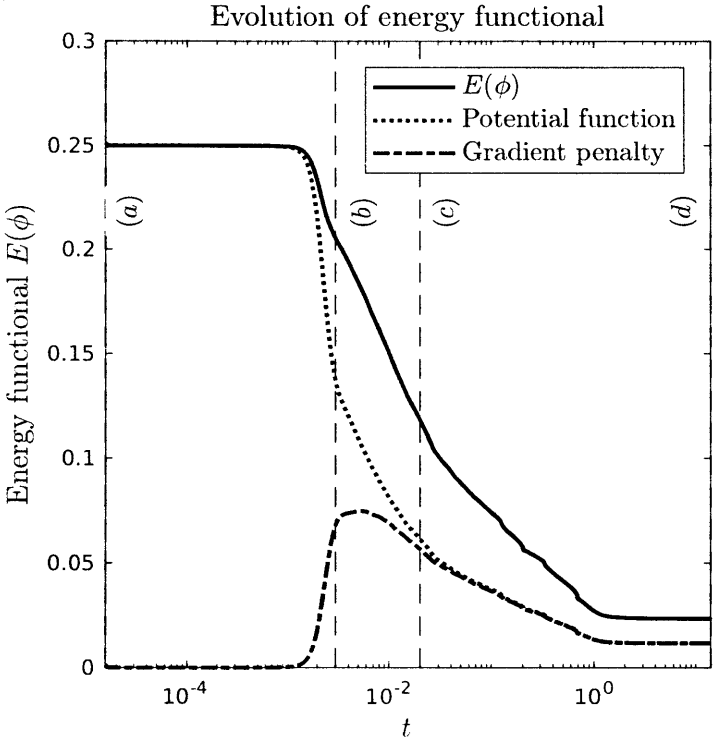

Figure 3-4: The solid line shows the time evolution of the energy functional $E(\phi)$. The dotted and dot-dash lines show the contribution of the potential function and gradient penalty terms to the energy functional, respectively. Snapshots shown in figure 3-3 correspond to time steps marked by vertical dashed lines. We can observe that the energy functional $E(\phi)$ decreases monotonically.

3.4 Effect of Cahn Hilliard parameters on interface thickness and tension

In order to calculate the dependence of interface tension δ and interface tension τ, it is useful to look at the solution of the Cahn Hilliard equation in one dimension. For a potential function of the type in equation 3.5, the solution is given by

$$\phi(x) = \tanh\left(\frac{x}{\delta}\right), \tag{3.24}$$

where δ is the thickness of the interface. This solution is shown with the solid line in figure 3-5. We can approximate this solution with a piecewise linear approximation

$$\tilde{\phi}(x) = \begin{cases} -1 & x \leq -\delta/2 \\ \frac{2x}{\delta} & -\delta/2 < x < \delta/2 \\ 1 & x \geq \delta/2 \end{cases}, \tag{3.25}$$

as shown by the dashed line in figure 3-5. The value of energy functional associated with the one dimensional solution is given by

$$\begin{aligned} E(\phi(x)) &= \int_{-\infty}^{\infty} \left(g(\phi) + \frac{\epsilon}{2}\nabla\phi.\nabla\phi\right) dx \\ &= \int_{-\infty}^{\infty} \left(g(\phi) + \frac{\epsilon}{2}\left(\frac{d\phi}{dx}\right)^2\right) dx. \end{aligned} \tag{3.26}$$

We can approximate the value of the energy functional as

$$\tilde{E} = \int_{-\infty}^{\infty} \left(g(\tilde{\phi}) + \frac{\epsilon}{2} \left(\frac{d\tilde{\phi}}{dx} \right)^2 \right) dx \tag{3.27}$$

$$\begin{aligned} &= \int_{-\infty}^{-\delta/2} \left(g(\tilde{\phi}) + \frac{\epsilon}{2} \left(\frac{d\tilde{\phi}}{dx} \right)^2 \right) dx \\ &+ \int_{-\delta/2}^{\delta/2} \left(g(\tilde{\phi}) + \frac{\epsilon}{2} \left(\frac{d\tilde{\phi}}{dx} \right)^2 \right) dx \\ &+ \int_{\delta/2}^{\infty} \left(g(\tilde{\phi}) + \frac{\epsilon}{2} \left(\frac{d\tilde{\phi}}{dx} \right)^2 \right) dx. \end{aligned} \tag{3.28}$$

Substituting the piecewise linear approximation $\tilde{\phi}(x)$ from equation 3.25, we get

$$\begin{aligned} \tilde{E} = &\int_{-\infty}^{-\delta/2} \left(g(-1) + \frac{\epsilon}{2} (0)^2 \right) dx \\ &+ \int_{-\delta/2}^{\delta/2} \left(g\left(\frac{2x}{\delta} \right) + \frac{\epsilon}{2} \left(\frac{2}{\delta} \right)^2 \right) dx \\ &+ \int_{\delta/2}^{\infty} \left(g(1) + \frac{\epsilon}{2} (0)^2 \right) dx. \end{aligned} \tag{3.29}$$

Since $g(\pm 1) = 0$,we are left with

$$\tilde{E} = \int_{-\delta/2}^{\delta/2} \left(g\left(\frac{2x}{\delta} \right) + \frac{\epsilon}{2} \left(\frac{2}{\delta} \right)^2 \right) dx. \tag{3.30}$$

By using variable substitution, and the definition of α in equation 3.6, we get

$$\tilde{E} = \frac{\delta}{2} \int_{-1}^{1} \left(g\left(\phi \right) \right) d\phi + \frac{2\epsilon}{\delta} \tag{3.31}$$

$$= \overbrace{\frac{\alpha\delta}{2}}^{\text{Potential energy}} + \overbrace{\frac{2\epsilon}{\delta}}^{\text{Gradient penalty}} \tag{3.32}$$

From equation 3.32, we can see the effect of δ on the potential energy and the gradient penalty. The potential energy increases with larger values of δ, while the gradient

penalty reduces. This is consistent with the behavior seen in figure 3-3 and figure 3-4. We can now argue that since the order parameter field is at equilibrium, the energy functional is at a local minimum. Therefore,

$$\frac{d\tilde{E}}{d\delta} = \frac{\alpha}{2} - \frac{2\epsilon}{\delta^2} = 0 \tag{3.33}$$

$$\Rightarrow \delta \sim \sqrt{\frac{\epsilon}{\alpha}}. \tag{3.34}$$

This relationship between ϵ,α, and δ can be seen in figure 3-6. We ran four Cahn-Hilliard simulation on a 1×1 computational domain. All simulations were initialized with the same boundary condition

$$\phi(x,y) = \begin{cases} -1 & x < 0.25 \\ 1 & 0.25 \leq x \leq 0.75 \\ -1 & x > 0.75 \end{cases}, \tag{3.35}$$

which allowed the use of periodic boundary conditions for numerical simplicity. The four simulations were run with values of $(\epsilon, \alpha) = (0.01, 1), (0.001, 1), (0.01, 10), (0.001, 10)$, shown in figure 3-6$(a)$, (b), (c), and (d) respectively. We can observe that decreasing ϵ from 0.01 to 0.001 while keeping α the same reduces the thickness δ by a factor of $\sim \sqrt{10}$. Increasing the value of α from 1 to 10 while keeping the value of ϵ constant produces the same effect. However, from figure 3-6(b) and (c), we can see the interface thickness remains unchanged when the ratio ϵ/α is the same.

To calculate the approximate energy functional $\tilde{E}$, we use the value of δ calculated in equation 3.34 into equation 3.32, giving us

$$\begin{aligned} \tilde{E} &= \frac{\alpha}{2}\sqrt{\frac{\epsilon}{\alpha}} + 2\epsilon\sqrt{\frac{\alpha}{\epsilon}} \\ &= \frac{5\sqrt{\epsilon\alpha}}{2}. \end{aligned} \tag{3.36}$$

Since the interface tension τ is the energy penalty per unit length of the phase

interface, we can conclude that

$$\tau \sim \sqrt{\epsilon\alpha} \tag{3.37}$$

We can see the effect of τ on the evolution of the order parameter field in figure 3-7. We have compared two spinodal decomposition simulations with identical initial conditions, boundary conditions and phase interface thickness δ, but different $\tau = 0.03$ and 0.3. On the left, we can see that the simulation with $\tau = 0.3$ has a higher value of $E(\phi)$ at all times, as compared to the simulation with $\tau = 0.03$. On the right, we have normalized the value of the energy functional with the value of the energy functional at $t = 0$, in order to compare the speed of spinodal decomposition. We can see that the simulation with $\tau = 0.3$ is ~ 10 times faster the simulation with $\tau = 0.03$.

These results can be explained by rewriting potential function as

$$g(\phi, \alpha) = \frac{15\alpha}{4}\left(\frac{\phi^4}{4} - \frac{\phi^2}{2} + \frac{1}{4}\right). \tag{3.38}$$

This allows to rewrite the Cahn-Hilliard equation in terms of δ and τ.

$$\begin{aligned}
\frac{\partial\phi}{\partial t} &= \nabla.M\nabla\left(\frac{\partial g(\phi,\alpha)}{\partial\phi} - \epsilon\nabla^2\phi\right) \\
&= \nabla.M\nabla\left(\alpha\frac{\partial g(\phi,1)}{\partial\phi} - \epsilon\nabla^2\phi\right) \\
&= \sqrt{\epsilon\alpha}\nabla.M\nabla\left(\sqrt{\frac{\alpha}{\epsilon}}\frac{\partial g(\phi,1)}{\partial\phi} - \sqrt{\frac{\epsilon}{\alpha}}\nabla^2\phi\right) \\
\frac{\partial\phi}{\partial t} &= \tau\nabla.M\nabla\left(\frac{1}{\delta}\frac{\partial g(\phi,1)}{\partial\phi} - \delta\nabla^2\phi\right).
\end{aligned} \tag{3.39}$$

We can now see that increasing τ while keeping δ the same effectively rescales time. This is consistent with the results shown in figure 3-7(b), where the order parameter field with the larger interface tension $\tau = 0.3$ decomposes faster than the order parameter field with interface tension $\tau = 0.03$.

In chapter 5, we use a modified potential function and the Cahn-Hilliard equation to simulate the permeation of gallium through aluminum grain boundaries. The modified potential function incorporates the location dependent energy of aluminum

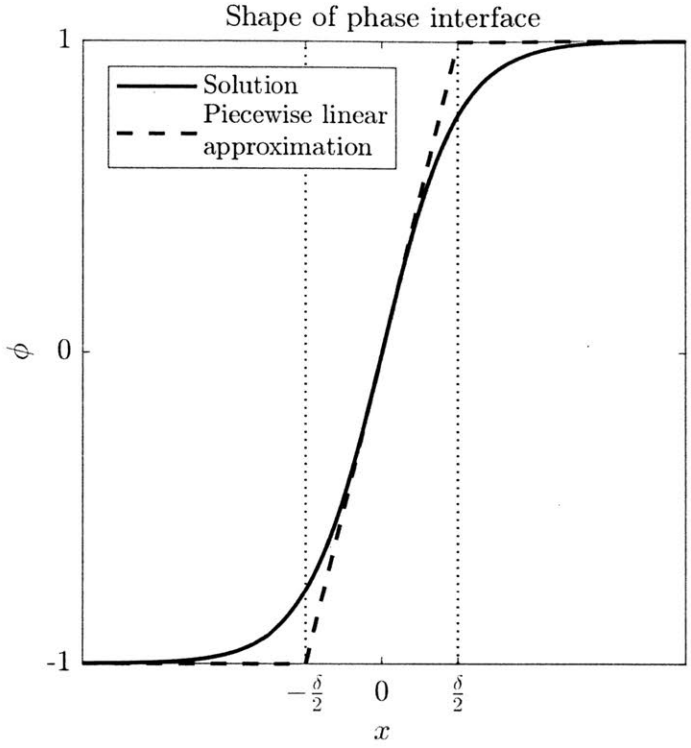

Figure 3-5: One dimensional solution of the Cahn Hilliard equation. The exact solution is shown by the solid line, and a piecewise approximation is shown with a dashed line.

grain boundaries. By controlling the interface thickness δ and the interface tension τ, as explored in this chapter, we will smoothly vary the behavior of the model from a front propagation model to a diffusion and precipitation model. A front propagation model has a large interface tension, which causes the front to be pinned by non-connected obstacles in the grain boundary plane. On the other hand, a diffusion and precipitation model has low interface tension and high interface thickness, allowing gallium to diffuse through gaps between obstacles.

In the next chapter, we will calculate location dependent grain boundary energy maps, which are used as inputs to the modified potential function.

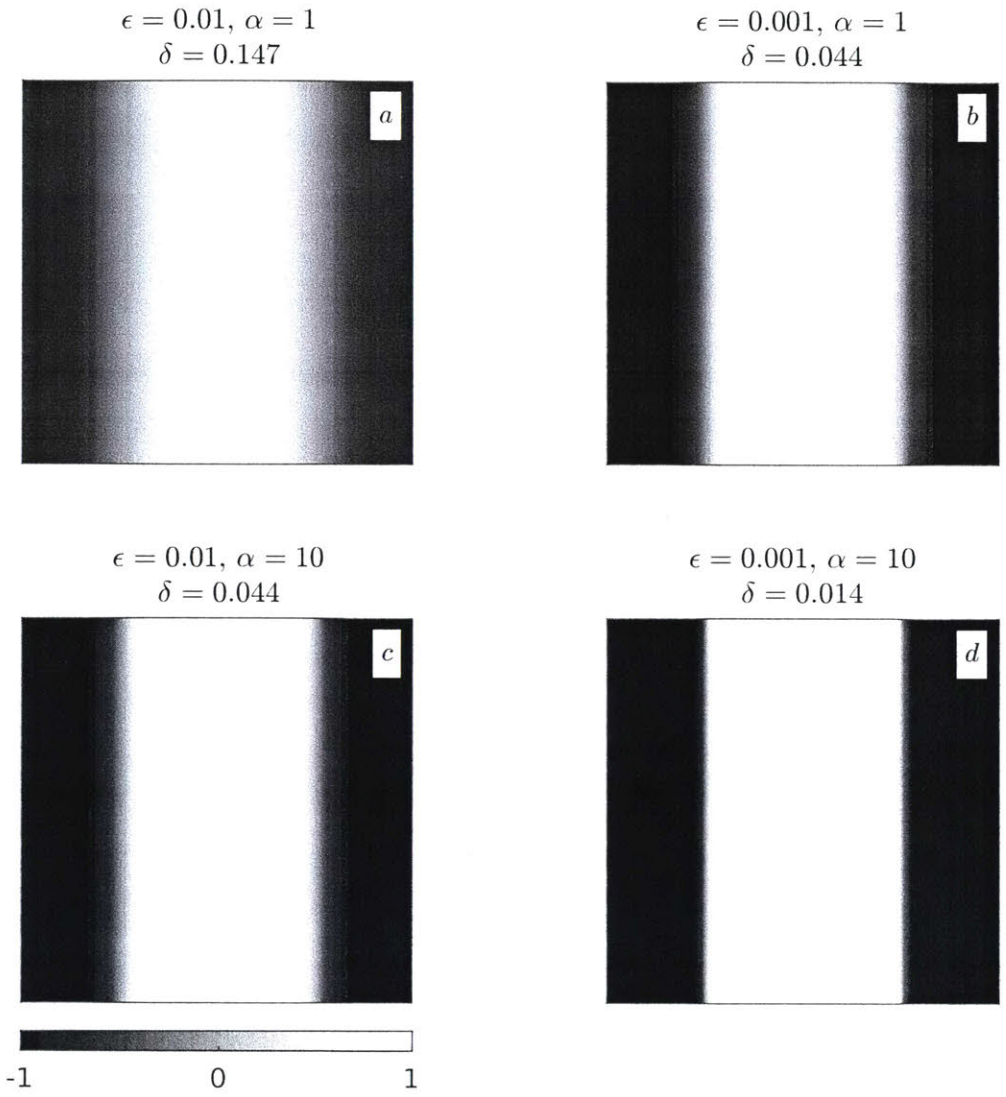

Figure 3-6: The effect of ϵ and α on the thickness of the interface between phases. Reducing ϵ from 0.01 in (a) and (c), to 0.001 in (b) and (d) reduces the thickness of the interface. The same effect can be seen by *increasing* α from 1 in (a) and (b), to 10 in (c) and (d). However, when the ratio ϵ/α stays constant, as in (b) and (c), the interface thickness remains unchanged.

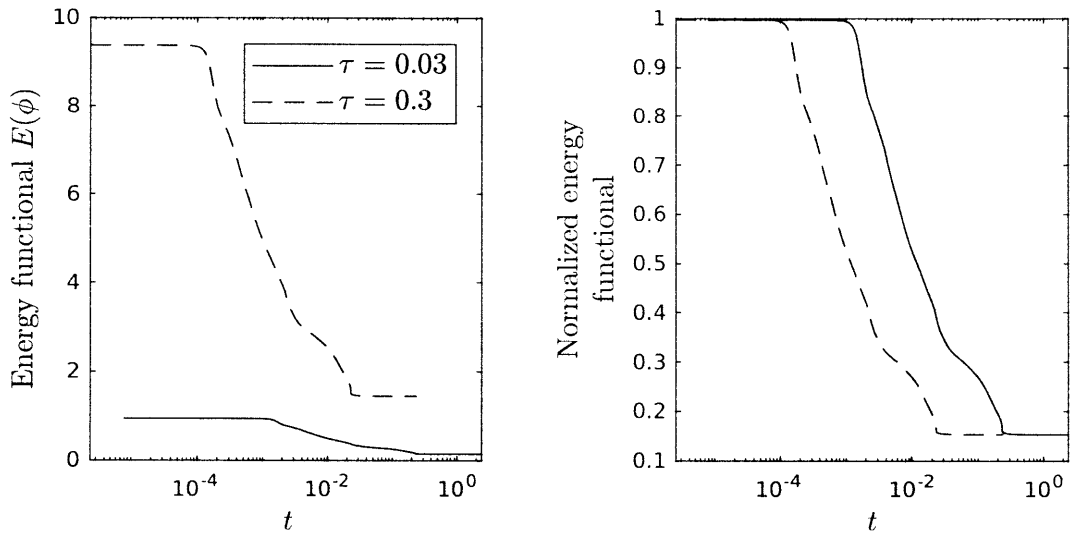

Figure 3-7: The effect of interface tension on spinodal decomposition dynamics. We are comparing the dynamics of two spinodal decomposition simulation, with identical initial conditions, boundary conditions, interface thickness, but with differing interface tension. On the left, we can see that the simulation with $\tau = 0.03$, has a lower energy functional as compared to the simulation with $\tau = 0.3$ at all times. On the right, we can observe the faster dynamics of the simulation with $\tau = 0.3$ by comparing the normalized energy functionals.

Chapter 4

Calculation of location dependent grain boundary energy

When an aluminum grain boundary is permeated by gallium, the aluminum grain boundary, which is an aluminum-aluminum interface, is replaced by two gallium-aluminum interfaces. This results in an interfacial energy change given by

$$\Delta\gamma = 2\gamma_{Ga,Al} - \gamma_{Al,Al}(\mathbf{x}), \tag{4.1}$$

where $\gamma_{Ga,Al}$ is the gallium-aluminum interfacial energy, and $\gamma_{Al,Al}(\mathbf{x})$ is the *location dependent* aluminum-aluminum interfacial energy. The permeation is energetically favorable if there is a net reduction in energy. We can define a permeability map

$$\beta(\mathbf{x}) = \gamma_{Al,Al}(\mathbf{x}) - 2\gamma_{Ga,Al}. \tag{4.2}$$

Permeation of gallium is energetically favorable when $\beta(\mathbf{x}) > 0$.

This permeability map will be used as an input to the Cahn-Hilliard equation in chapter 5. In order to calculate the permeability map, we need to calculate the location dependent grain boundary energy $\gamma_{Al,Al}(\mathbf{x})$.

$\gamma_{Al,Al}(\mathbf{x})$ is an intrinsic property of a grain boundary, and depends on the crystallography of the grain boundary. The crystallography consists of the misorientation

matrix g_{AB}, describing the relative orientation of the two grains forming the grain boundary, and the grain boundary plane normal vector $\hat{\mathbf{n}}$. In order to calculate $\gamma_{Al,Al}(\mathbf{x})$, we have to first calculate the grain boundary crystallography. Also, in general, $\gamma_{Al,Al}(\mathbf{x})$ is an anisotropic distribution of energy. Therefore the speed of permeation of gallium through an aluminum grain boundary, with an associated $\gamma_{Al,Al}(\mathbf{x})$ distribution, is dependent on the direction of permeation in the grain boundary plane, which needs to be determined.

In section 4.1, we use previously unpublished transmission electron microscopy data provided to us by Dr. Richard Hugo[1] to calculate both the grain boundary crystallography, as well as the direction of permeation of gallium in the grain boundary plane.

The grain boundary crystallography was used as an input to a atomistic simulation to calculate the location dependent grain boundary energy $\gamma_{Al,Al}(\mathbf{x})$. This work was done by Dr. Sanket S. Navale[2] as part of his PhD at MIT. In section 4.2, we will briefly discuss the construction of the atomistic model and extraction of the grain boundary energy.

Atomistic simulations are limited in the number of atoms they can simulate due to computational considerations. As a result, the location dependent grain boundary energy maps computed using atomistic methods were limited to 200Å$\times$200Å in size. To overcome this limitation, we statistically extrapolated the grain boundary energy maps using a Gaussian process approximation. We will discuss this extrapolation in section 4.2.

In section 4.3, we calculate the permeability maps $\beta(\mathbf{x})$ for different grain boundaries and different values of $\gamma_{Ga,Al}$.

[1]Dr. Richard Hugo: hugo@pdx.edu
[2]Dr. Sanket S. Navale: sanket@mit.edu

4.1 Calculation of grain boundary crystallography using TEM data

Figure 4-1 show one set of TEM images collected by Hugo and Hoagland as part of their experimental study of gallium permeation of aluminum [28, 29, 30]. The data set contains two Kikuchi diffraction pattern captured from the two grains forming the grain boundary, shown in figures 4-1(a) and (e). The data set also contains one bright field image of the trace of the grain boundary, shown in figure 4-1(c).

The Kikuchi diffraction patterns contain all information needed to calculate the orientation of the grains with respect to the lab frame of reference. Figures 4-1(b) and (f) show the unit cells of the two grains in the lab frame of reference. The calculation of orientation information from Kikuchi diffraction patterns was done using the techniques described by Heilmann *et al.* [26]. By knowing the orientation of the two grain with respect to the lab frame of reference, we can calculate the rotation matrix g_{AB} which with respect to each other.

At the time of capturing these images, Hugo and Hoagland aligned each grain boundary sample such that the electron beam traveled parallel to the grain boundary plane. This can be seen in figure 4-1(c), where the grain boundary plane is visible as a single trace. Had the electron beam direction not been parallel to the grain boundary plane, we would have observed two grain boundary traces, one for the top surface of the sample, and one for the bottom surface of the sample. Due to this alignment, the image of the grain boundary trace allows us to calculate the orientation of the grain boundary plane normal $\hat{\mathbf{n}}$, as well as the permeation direction of gallium within the grain boundary plane.

4.1.1 Physics of formation of Kikuchi lines

Kikuchi diffraction patterns are created by the diffraction of inelastically scattered electron by the lattice planes of the crystal sample [68]. Each set of lattice planes produce a corresponding set of parallel lines on the viewing screen of the microscope.

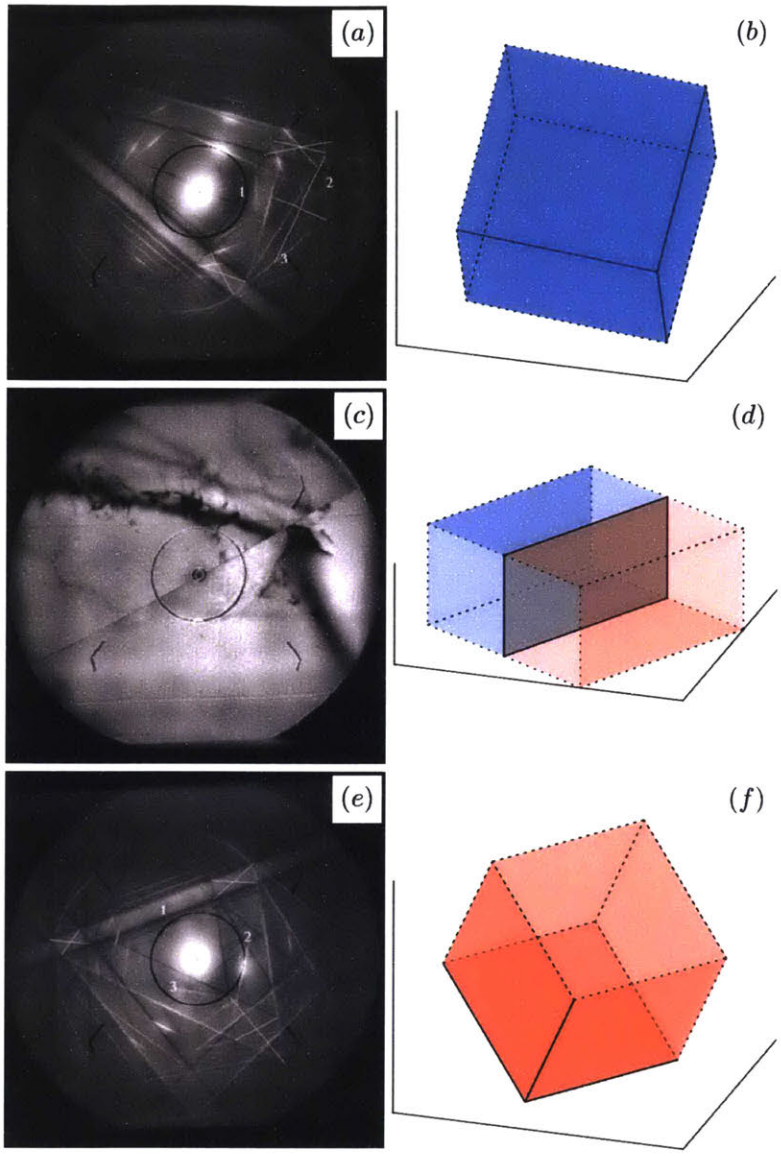

Figure 4-1: One set of TEM images, and the crystallography information obtained from them. (a) and (e) Kikuchi diffraction patterns collected from grain boundary number 27. Images collected by Hugo and Hoagland. (b) and (f) The orientations information obtained from the Kikuchi diffraction patterns. The unit cell for the two grains are plotted in the lab frame of reference. (c) Bright field image showing the grain boundary trace. The electron beam is in the plane of the grain boundary, hence only a single trace is visible. (d) The grain boundary, shown in gray, is formed at the intersection of the two grains, shown in blue and red. The short side is aligned with the electron beam. The long side is along the direction of permeation.

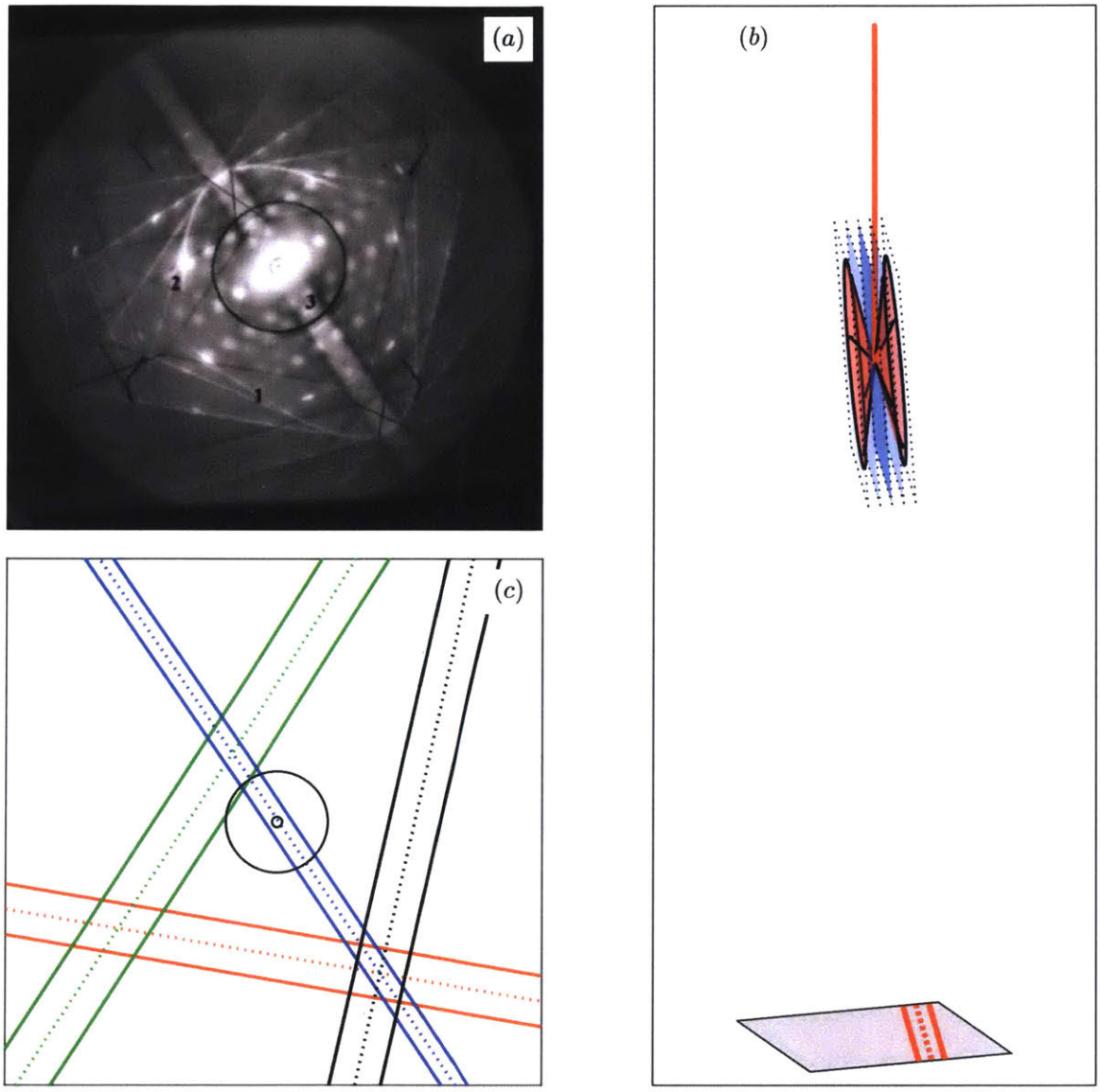

Figure 4-2: Formation of kikuchi lines. (a) Kikuchi pattern captured by Hugo and Hoagland, and used in this work. Note that multiple pairs of Kikuchi lines are visible at the same time. (b) The incoming electron beam gets diffracted by crystal planes along two cones. The angle of the cones is dictated by the Bragg condition. The projection of the cones onto the viewing screen creates Kikuchi lines, marked by the solid red lines. The dotted red line is the center line between the Kikuchi lines, which is the projection of the grain boundary planes onto the viewing screen. (c) Simulated Kikuchi pattern, showing four of the Kikuchi line pairs observed in part (b).

Figure 4-2(a) shows a Kikuchi diffraction pattern, where a number of Kikuchi line pairs are visible. The undiffracted electron beam is visible as the bright spot at the center of the image.

Figure 4-2(c) shows four of the kikuchi line pairs visible in figure 4-2(a), as well as the undiffracted electron beam in the center. Additionally, the center lines of each Kikuchi line pair is shown by a dotted line. Note that these center lines are not visible is experimental Kikuchi patterns, but can be inferred from them. Kikuchi line pairs are characterized by the following parameters.

- Δ: The spacing between the kikuchi lines.
- D: The perpendicular distance of the center line from the point of incidence of the electron beam.
- γ: The angle between the x-axis of the image, and the perpendicular from the origin to the center line.

Figure 4-2(b) shows the formation of one pair of Kikuchi lines. The electron beam, shown by the vertical red line, is scattered by a set of lattice planes, with the Miller index (h,k,l). The scattered electrons are diffracted along two cones, shown in red. The included angle γ between the surface of the cones and the lattice planes is given by Bragg's condition

$$\sin(\alpha) = \frac{\lambda}{2d}, \tag{4.3}$$

where λ is the electron beam wavelength, and d is the distance between the lattice planes. For a cubic lattice, planes with Miller indices (h,k,l) are separated by,

$$d = \frac{a}{\sqrt{h^2+k^2+l^2}}, \tag{4.4}$$

where a is lattice constant. $a = 404.95pm$ for aluminum. The Kikuchi diffraction patterns were collected with an electron beam energy $= 200KeV$, with an associated DeBroglie wavelength $\lambda = 2.5pm$. Since $\lambda << a$, the small angle approximation is valid:

$$\alpha = \frac{\lambda\sqrt{h^2+k^2+l^2}}{2a}. \tag{4.5}$$

The two diffracted cones intersect the image plane separated by the microscope length L, producing two parabolic lines. For sufficiently large value of L, the two parabolas appear to be straight, parallel lines. The spacing of the lines is given by

$$\Delta = 2L\tan(\alpha) \tag{4.6}$$

$$= \frac{\lambda L}{a}\sqrt{h^2+k^2+l^2}. \tag{4.7}$$

In figure 4-2(b), the Kikuchi lines are shown as solid red lines on the gray image plane.

For the lines to appear straight and parallel, the condition $\delta_k << L$ needs to be satisfied. This condition was satisfied by all Kikuchi diffraction patterns collected by Hugo and Hoagland. They collected their data with microscope lengths $L = 600mm$ and $L = 800mm$. The most widely separated lines are separated by $\delta_k \sim 20mm$.

Not all lattice planes produce Kikuchi lines. The presence, absence, and intensity of Kikuchi lines are governed by the structure factor. For FCC lattices, such as aluminum, the three Miller indices need to have the same parity to produce Kikuchi lines. That is, either h, k, l need to be all odd, or all even. More details about the structure factor can be found in [68].

4.1.2 Calculating the misorientation matrix using Kikuchi patterns

From the construction of Kikuchi lines, we can see that the imaginary center line is a projection of the lattice plane with Miller indices (h, k, l) onto the image plane. To calculate the orientation of the grain, we need to index at least three Kikuchi line pairs. The values of Δ, D and γ for the Kikuchi line pairs are calculated by tracing the lines manually.

To index the Kikuchi line pairs, we first compared the line separations Δ.

$$\frac{\Delta_i}{\Delta_j} = \frac{\sqrt{h_i^2+k_i^2+l_i^2}}{\sqrt{h_j^2+k_j^2+l_j^2}}, \qquad i,j \in \{1,2,3\}. \tag{4.8}$$

We used a brute force search to find Miller indices which satisfy equation 4.8 to within a tolerance of 0.1. Since the sign and order of the Miller indices don't affect the ratio of line spacings, we limited our search to

$$9 \geq h \geq k \geq l \geq 0 \qquad (h,k,l) \text{ have same parity.} \tag{4.9}$$

At the end of this search, we are left with sets of 3 Miller indices, which satisfy the spacing of the Kikuchi lines.

Lattice planes with Miller indices (h,k,l) have a normal vector $h\hat{e_1} + k\hat{e_2} + l\hat{e_3}$, where $\hat{e_1}$,$\hat{e_2}$, and $\hat{e_3}$ are the unit vectors in the crystal frame of reference. Thus, the angle between the lattice planes (h_1,k_1,l_1) and (h_2,k_2,l_2) is given by

$$cos(\alpha_{ij}) = \frac{h_i h_j + k_i k_j + l_i l_j}{\sqrt{h_i^2 + k_i^2 + l_i^2}\sqrt{h_j^2 + k_j^2 + l_j^2}} \tag{4.10}$$

Since the Kikichi center lines are projections of the lattice planes on to the image plane, the angle between Kikuchi lines is also given by equation 4.10. We compared angles measured between the Kikuchi lines with all rearrangement and sign combinations of the Miller indices found by matching the spacing constraint in equation 4.8. For each triplet of valid Miller indices

$$[(h_1,k_1,l_1),(h_2,k_2,l_2),(h_3,k_3,l_3)]\,,$$

we can in general find $(3! \times 2^3)^3 = 110592$ combinations. Each index h,k, and l can take a positive sign, or a negative sign, giving $2^3 = 8$ possibilities. Sets of signed Miller indices (h,k,l) have $3! = 8$ rearrangements. Redundant combinations were eliminated wherever found in the interest of computational time.

We used a brute force search to find a combination of Miller indices which satisfies the angle constraint in equation 4.10 to within 0.1 radians. Solutions found to be identical to within FCC crystal symmetry were eliminated. In case a unique solution was not found at this point, we introduced more Kikuchi lines pairs to the constraints to eliminate solutions.

Next, we need to calculate the orientation of the electron beam in the crystal frame of reference. To do this, we use the perpendicular distance D. Figure 4-3 shows the cross section of the electron microscope, in the plane formed by the beam direction unit vector **BD** and the lattice plane normal unit vector

$$\mathbf{hkl} = \frac{h\hat{e_1} + k\hat{e_2} + l\hat{e_3}}{\sqrt{h^2 + k^2 + l^2}}. \tag{4.11}$$

The geometric relation between D, L, **BD**, and **hkl** is given by

$$\begin{aligned} \mathbf{BD.hkl} &= -|\mathbf{BD}||\mathbf{hkl}|\frac{D}{\sqrt{L^2 + D^2}} \\ &= -\frac{D}{\sqrt{L^2 + D^2}} \end{aligned} \tag{4.12}$$

If we have a triplet of Kikuchi lines indexed, we can solve for **BD** and L by solving the system of equations

$$\mathbf{BD.h_1k_1l_1} = -\frac{D_1}{\sqrt{L^2 + D_1^2}} \tag{4.13}$$

$$\mathbf{BD.h_2k_2l_2} = -\frac{D_2}{\sqrt{L^2 + D_2^2}} \tag{4.14}$$

$$\mathbf{BD.h_3k_3l_3} = -\frac{D_3}{\sqrt{L^2 + D_3^2}} \tag{4.15}$$

$$\mathbf{BD.BD} = 1 \tag{4.16}$$

We used the method described by Heilmann *et al.* to solve this system of equations [26]. The actual microscope length L used to capture the Kikuchi diffraction patterns is known to us as part of the data set provided by Dr. Richard Hugo. We can use the value of L calculated by solving equations 4.13 - 4.16 to further eliminate incorrect Kikuchi line matchings.

Upon calculating the beam direction unit vector **BD**, the rotation matrix between the crystal frame of reference and the lab frame of reference can be calculated in two steps. First, the crystal is rotated such that the beam direction lines up with the z-axis of the lab frame of reference, and **hkl** lies in the xz-plane. This rotation matrix

is given by

$$R_{CP} = \begin{pmatrix} (\mathbf{BD} \times \mathbf{hkl}) \times \mathbf{BD} \\ \mathbf{BD} \times \mathbf{hkl} \\ \mathbf{BD} \end{pmatrix}. \tag{4.17}$$

We can see that this matrix is the correct matrix by calculating $R_{CP}.\mathbf{BD}$

$$\begin{aligned} R_{CP}.\mathbf{BD} &= \begin{pmatrix} (\mathbf{BD} \times \mathbf{hkl}) \times \mathbf{BD} \\ \mathbf{BD} \times \mathbf{hkl} \\ \mathbf{BD} \end{pmatrix}.\mathbf{BD} \\ &= \begin{pmatrix} ((\mathbf{BD} \times \mathbf{hkl}) \times \mathbf{BD}).\mathbf{BD} \\ (\mathbf{BD} \times \mathbf{hkl}).\mathbf{BD} \\ \mathbf{BD}.\mathbf{BD} \end{pmatrix} \\ &= [0,0,1]^T \end{aligned} \tag{4.18}$$

and $R_{CP}.\mathbf{hkl}$.

$$\begin{aligned} R_{CP}.\mathbf{hkl} &= \begin{pmatrix} (\mathbf{BD} \times \mathbf{hkl}) \times \mathbf{BD} \\ \mathbf{BD} \times \mathbf{hkl} \\ \mathbf{BD} \end{pmatrix}.\mathbf{hkl} \\ &= \begin{pmatrix} ((\mathbf{BD} \times \mathbf{hkl}) \times \mathbf{BD}).\mathbf{hkl} \\ (\mathbf{BD} \times \mathbf{hkl}).\mathbf{hkl} \\ \mathbf{BD}.\mathbf{hkl} \end{pmatrix} \\ &= \begin{pmatrix} ((\mathbf{BD} \times \mathbf{hkl}) \times \mathbf{BD}).\mathbf{hkl} \\ 0 \\ \mathbf{BD}.\mathbf{hkl} \end{pmatrix} \end{aligned} \tag{4.19}$$

In the second step, the crystal frame of reference is rotated by angle γ around the

z-axis. This rotation matrix is given by

$$R_{PL} = \begin{pmatrix} \cos(\gamma) & -\sin(\gamma) & 0 \\ \sin(\gamma) & \cos(\gamma) & 0 \\ 0 & 0 & 1 \end{pmatrix} \tag{4.20}$$

The rotation matrix relating the crystal frame of reference and lab frame of reference can be calculated as

$$R = R_{PL} R_{CP} \tag{4.21}$$

By calculating the rotation matrices between both grains and the lab frame of reference, we can calculate the misorientation g_{AB} between grains A and B as

$$g_{AB} = R_B^{-1} R_A \tag{4.22}$$

4.1.3 Calculating grain boundary plane orientation and permeation direction

We used the bright field image of the grain boundary trace to calculate both the grain boundary plane orientation $\hat{n}$, and the permeation direction **PD**. We measured the angle θ between the grain boundary trace and the x-axis of the lab frame of reference manually. Gallium permeates along the grain boundary trace. Therefore, in the lab frame of reference, the permeation direction

$$\mathbf{PD} = [\cos(\theta), \sin(\theta), 0]^T. \tag{4.23}$$

From the orientation of the sample in the electron microscope, we know that the beam direction is in the grain boundary plane. In the lab frame of reference

$$\mathbf{BD} = [0, 0, 1]^T. \tag{4.24}$$

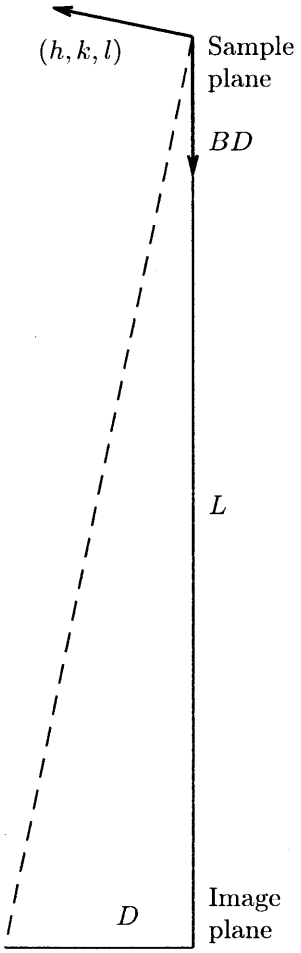

Figure 4-3: Cross section of the electron microscope in the plane formed by the beam direction and one (h, k, l) vector. The (h, k, l) vector is normal to the lattice plane, which is shown by a dashed line.

The grain boundary plane normal $\hat{n}$ can be calculated by taking the cross product of **BD** and **PD**.

$$\begin{aligned}\hat{\mathbf{n}} &= \mathbf{BD} \times \mathbf{PD} \\ &= [0,0,1]^T \times [\cos(\theta), \sin(\theta), 0]^T \\ &= [-\sin(\theta), \cos(\theta), 0]^T\end{aligned} \tag{4.25}$$

The vectors **PD** and $\hat{\mathbf{n}}$ can be rotated to the reference frames of the two grains using the rotation vectors R_A and R_B calculated previously.

We received 53 sets of raw TEM images from Dr. Richard Hugo, collected as part of their 2000 study [30]. Each set contained two Kikuchi diffraction patterns, and one bright field image of the grain boundary trace. Unfortunately, the information connecting individual TEM data-sets to the crystallography and permeation speeds reported in [30] had been lost. By recalculating the grain boundary crystallography $(g_{AB}, \hat{\mathbf{n}})$ and comparing with the values reported in [30], we were able to match 17 TEM data sets to their reported permeation speed values. The matched grain boundaries, their crystallography, gallium permeation direction, and permeation speeds are tabulated in table 4.1. The grain boundary numbers reported in table 4.1, as well as the remainder of this text, correspond to the data reported in [30].

Table 4.1: List of matched grain boundaries. The grain boundary numbers correspond to the numbers in the data set reported by Hugo and Hoagland [30]. The permeation direction is reported in the frame of reference of the lower crystal

GB#	Rotation axis	Rotation angle (^{o})	upper/lower plane normals	Permeation direction	Permeation speed ($\mu m/s$)
9	[0.7,0.7,0.11]	49	[0.76,0.58,0.3] [0.22,0.022,-0.98]	[0.22,-0.97,0.028]	0.28
10	[0.96,0.23,0.18]	44	[0.81,0.58,0.11] [-0.2,0.97,0.11]	[0.21,0.15,-0.97]	2.7

11	[0.74,0.66,0.1]	38	[0.72,0.68,0.11] [-0.7,0.56,0.45]	[-0.0041,0.63,-0.78]	2.4
13	[0.87,0.46,0.14]	40	[0.71,0.63,0.33] [0.34,-0.93,0.15]	[-0.085,0.13,0.99]	3.6
16	[0.75,0.58,0.31]	41	[0.8,0.57,0.17] [-0.17,-0.25,0.95]	[-0.5,0.86,0.13]	12
17	[0.74,0.6,0.31]	43	[0.96,0.22,0.15] [0.56,-0.2,-0.8]	[-0.037,-0.97,0.22]	0.57
20	[0.93,0.37,0.096]	38	[0.99,0.14,0.034] [-0.44,0.89,-0.14]	[0.12,-0.091,-0.99]	2.4
21	[0.79,0.61,0.033]	7.1	[0.82,0.54,0.16] [-0.55,0.83,-0.074]	[0.5,0.26,-0.83]	0
22	[0.99,0.11,0.082]	42	[0.84,0.53,0.088] [0.33,0.38,-0.86]	[0.59,-0.8,-0.13]	4.1
23	[0.99,0.14,0.069]	42	[0.93,0.38,0.036] [-0.17,0.25,0.95]	[-0.08,0.96,-0.26]	0.16
27	[0.94,0.28,0.2]	9.2	[0.83,0.45,0.33] [-0.37,0.83,0.41]	[-0.17,0.37,-0.91]	0.01
29	[0.78,0.52,0.36]	11	[0.96,0.28,0.0046] [-0.056,-0.22,0.97]	[-0.43,0.89,0.18]	0.66
31	[0.96,0.28,0.031]	11	[0.81,0.45,0.37] [-0.23,-0.88,0.41]	[-0.52,0.47,0.72]	0.07
32	[0.88,0.44,0.18]	8.7	[0.89,0.4,0.21] [0.28,-0.42,-0.87]	[0.28,-0.83,0.49]	0.18
34	[0.94,0.33,0.037]	23	[0.71,0.69,0.15] [0.49,-0.55,-0.68]	[-0.23,-0.83,0.51]	0.6
35	[0.99,0.12,0.043]	18	[0.92,0.3,0.27] [0.032,0.94,-0.34]	[0.43,-0.31,-0.84]	0.49

37	[0.75,0.56,0.34]	6.8	[0.94,0.35,0.022] [0.011,-0.31,0.95]	[-0.4,0.87,0.29]	0.001

4.2 Calculation of location dependent grain boundary energy maps

The crystallography information calculated in the previous section was used to construct atomistic models of grain boundaries by our collaborator, Dr. Sanket S. Navale, as part of his PhD thesis. Using these atomistic models, the location dependent grain boundary energy (LDGBE) was calculated. Two LDGBE maps, for grain boundaries 35 and 13 are shown in figures 4-5(a) and (c). The atomistic simulations used to calculate the LDGBE distributions are computationally intensive. This limits the calculated grain boundary energy maps to a maximum feasible size of 200Å$\times$200Å. We need a way to extrapolate the LDGBE distributions to larger dimensions to use in our phase field model for the permeation of gallium.

We can see that the LDGBE maps shown in figures 4-5(a) and (c) have a quasi-periodic structure: they have a periodic structure, with random variations superimposed. These random variations are a feature of the LDGBE distributions, and any extrapolation method we use needs to capture and generate this random variation.

We have used Gaussian process to model the LDGBE distributions calculated by the atomistic simulations. We have used these Gaussian process models to then extrapolate the distributions to larger dimensions, which we will use in the prediction of permeation velocities in chapter 5.

4.2.1 Gaussian process regression

A Gaussian process $f(\mathbf{x})$ is a stochastic process completely defined by a mean function $m(\mathbf{x})$ and a covariance function $k(\mathbf{x}, \mathbf{x}')$ [56].

$$m(\mathbf{x}) = \mathbb{E}[f(\mathbf{x})] \tag{4.26}$$

$$k(\mathbf{x}, \mathbf{x}') = \mathbb{E}[(f(\mathbf{x}) - m(\mathbf{x}))(f(\mathbf{x}') - m(\mathbf{x}'))] \tag{4.27}$$

$$f(\mathbf{x}) \sim \mathcal{GP}(m(\mathbf{x}), k(\mathbf{x}, \mathbf{x}')) \tag{4.28}$$

The Gaussian process $f(\mathbf{x})$ is a stationary process if the covariance function $k(\mathbf{x}, \mathbf{x}')$ is dependent only on $(\mathbf{x} - \mathbf{x}')$,

$$k(\mathbf{x}, \mathbf{x}') = cov(\mathbf{x} - \mathbf{x}'), \tag{4.29}$$

and the mean function $m(\mathbf{x})$ is a constant. Since the covariance function $k(\mathbf{x}, \mathbf{x}')$ is only dependent on the offset $(\mathbf{x} - \mathbf{x}')$, the Gaussian process $f(\mathbf{x})$ is unaffected by translations. The squared exponential covariance function, shown in figure 4-4(a), is a popular covariance function used in Gaussian process regression. It is given by the relation

$$k_{se}(\mathbf{x}, \mathbf{x}') = \sigma \exp\left(\frac{1}{2l^2}\|\mathbf{x} - \mathbf{x}'\|^2\right). \tag{4.30}$$

Any finite samples drawn from $f(\mathbf{x})$ at sample points $\mathbf{X}_*$ are jointly Gaussian. The samples are distributed as

$$f(\mathbf{X}_*) \sim \mathcal{N}(m(\mathbf{X}_*), K(\mathbf{X}_*, \mathbf{X}_*)) \tag{4.31}$$

where $K(\mathbf{X}_*, \mathbf{X}_*)$ is the covariance matrix.

$$K(\mathbf{X}_*, \mathbf{X}_*) = [k(\mathbf{x_i}, \mathbf{x_j})], \qquad \mathbf{x_i}, \mathbf{x_j} \in \mathbf{X}_* \tag{4.32}$$

Figure 4-4(b) shows three samples drawn from $f(\mathbf{x}) \sim \mathcal{GP}(0, k_{se}(\mathbf{x}, \mathbf{x}'))$, with $\sigma = 1$ and $l = 1$. $f(\mathbf{x})$ is sampled on a dense grid $\mathbf{X}_* = [-10, -9.9, \cdots, 9.9, 10]$. We

can observe that the samples are smooth, and that they vary over a characteristic length scale of ≈ 1. $f(\mathbf{x})$ is largely contained by the bounds $-2 < f(\mathbf{x}) < 2$. The length scale of variation and bounds can be changed by changing the value of σ and l.

If at sample points $\mathbf{X}_d$, we have data points $\mathbf{f_d}$, we can draw conditional samples from $f(\mathbf{x})$.

$$f(\mathbf{X}_*)|\mathbf{X_d}, \mathbf{f_d} \sim \mathcal{GP}(m(\mathbf{X}_*)|\mathbf{X_d}, \mathbf{f_d}, K(\mathbf{X}_*, \mathbf{X}_*)|\mathbf{X_d}, \mathbf{f_d}.) \tag{4.33}$$

$$m(\mathbf{X}_*)|\mathbf{X_d}, \mathbf{f_d} = K(\mathbf{X}_*, \mathbf{X_d})K(\mathbf{X_d}, \mathbf{X_d})^{-1}\mathbf{f_d} \tag{4.34}$$

$$K(\mathbf{X}_*, \mathbf{X}_*)|\mathbf{X_d}, \mathbf{f_d} = K(\mathbf{X}_*, \mathbf{X}_*) - K(\mathbf{X}_*, \mathbf{X_d})K(\mathbf{X_d}, \mathbf{X_d})^{-1}K(\mathbf{X_d}, \mathbf{X}_*) \tag{4.35}$$

In figure 4-4(c), we have sampled $f(\mathbf{x})$ on the same dense grid $\mathbf{X}_*$, but conditioned on three data points shown in red circles. The drawn samples have the same smoothness and length scale of variation as the samples in figure 4-4(b), with the difference being that they all pass through the three data points. Conceptually, these samples could be generated by generating a large number of unconditioned samples, and rejecting all samples which do not pass through the data points $(\mathbf{X_d}, \mathbf{f_d})$.

In general, a Gaussian process $f(\mathbf{x})$ defines a probability distribution over a space of functions [56]. The properties of the functions are controlled by the covariance function $k(\mathbf{x}, \mathbf{x}')$. We use this idea to extrapolate the LDGBE distributions $\gamma_{al,al}(\mathbf{x})$. We model the LDGBE distributions as realizations of a Gaussian process

$$\gamma_{al,al}(\mathbf{x}) \sim \mathcal{GP}(m(\mathbf{x}), k(\mathbf{x}, \mathbf{x}')) \tag{4.36}$$

We calculate the mean function $m(\mathbf{x})$ and covariance function $k(\mathbf{x}, \mathbf{x}')$ empirically using the results of the atomistic simulations in section ??. We then use the simulations as seeds for a recursive extrapolation of the energy maps.

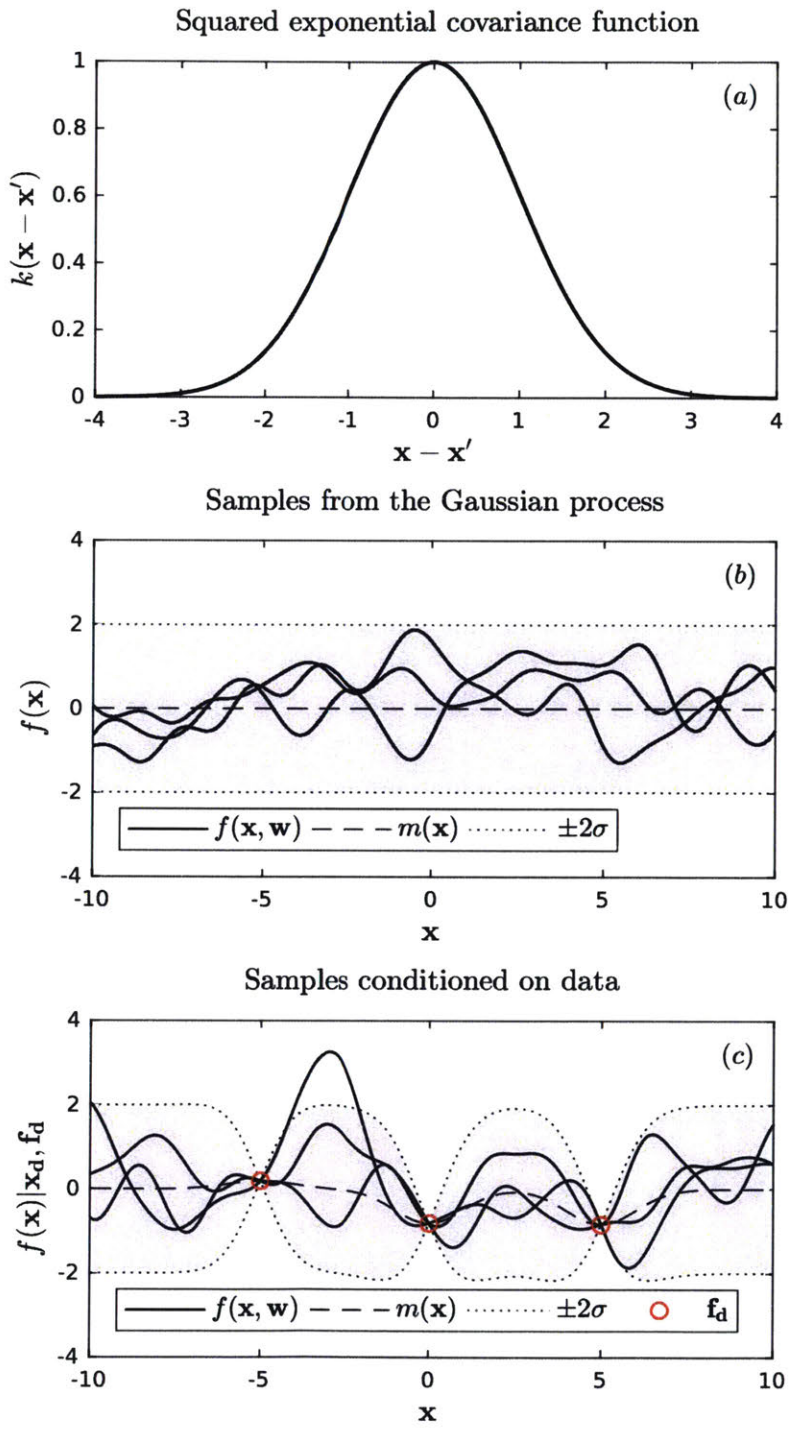

Figure 4-4: (*a*) Squared exponential covariance function with $\sigma = 1$ and $l = 1$. (*b*) Samples drawn from $f(\mathbf{x})$. The samples are smooth and have a length scale of variation of ≈ 1. (*c*) Samples drawn from $f(\mathbf{x})$ conditioned on the three data points marked by red circles.

4.2.2 Calculation of empirical mean and covariance function

The empirical mean and covariance functions are calculated using the LDGBE distributions calculated in section ??. The empirical mean function is simply defined as the arithmetic mean of the energy distribution $\gamma_{al,al}(x)$.

$$m(\mathbf{x}) = \mathbb{E}\left[\gamma_{al,al}(\mathbf{x})\right] \tag{4.37}$$

$$m \approx \frac{1}{N}\sum_{i=1}^{N}\gamma_{al,al}(\mathbf{x}_i), \tag{4.38}$$

where $\{\mathbf{x}_i\}$ are the grid points over which $\gamma_{al,al}(\mathbf{x})$ has been computed.

The empirical covariance function was calculated as the auto-covariance of $(\gamma_{al,al}(x) - m)$. Let $\mathcal{F}[.]$ be the Fourier transform, and $\mathcal{F}^{-1}[.]$ be the inverse Fourier transform. The auto-covariance of $(\gamma_{al,al}(\mathbf{x}) - m)$ was calculated as

$$k(\mathbf{x}-\mathbf{x}') = \mathcal{F}^{-1}\left[\|\mathcal{F}\left[\gamma_{al,al}(.) - m\right]\|^2\right](\mathbf{x}-\mathbf{x}'). \tag{4.39}$$

In practice, the FFT and inverse FFT functions built into `MATLAB` were used to calculate $k(\mathbf{x}-\mathbf{x}')$.

Figures 4-5(a) and (c) show the LDGBE distributions for grain boundaries 35 and 13. The energy distributions have a size of 200Å×200Å, with a grid spacing of 1Å. The corresponding auto-covariance functions are shown in figures 4-5(b) and (d). We can see that the auto-covariance functions capture the quasi-periodic nature of the energy distributions. The covariance is highest for offset $(\mathbf{x}-\mathbf{x}') = 0$, and falls as the offset value increases. Points with offsets values which lie on the periodic grid of the grain boundary structure are more strongly correlated with each other than points which do not. The auto-covariance has a maximum offset value of $(\mathbf{x}-\mathbf{x}') = (\pm 100\text{Å}, \pm 100\text{Å})$

4.2.3 Generation of new energy landscape patches

We use a recursive algorithm to extrapolate the LDGBE maps calculated in section ??. We start by calculating the empirical mean energy m, and the auto-covariance

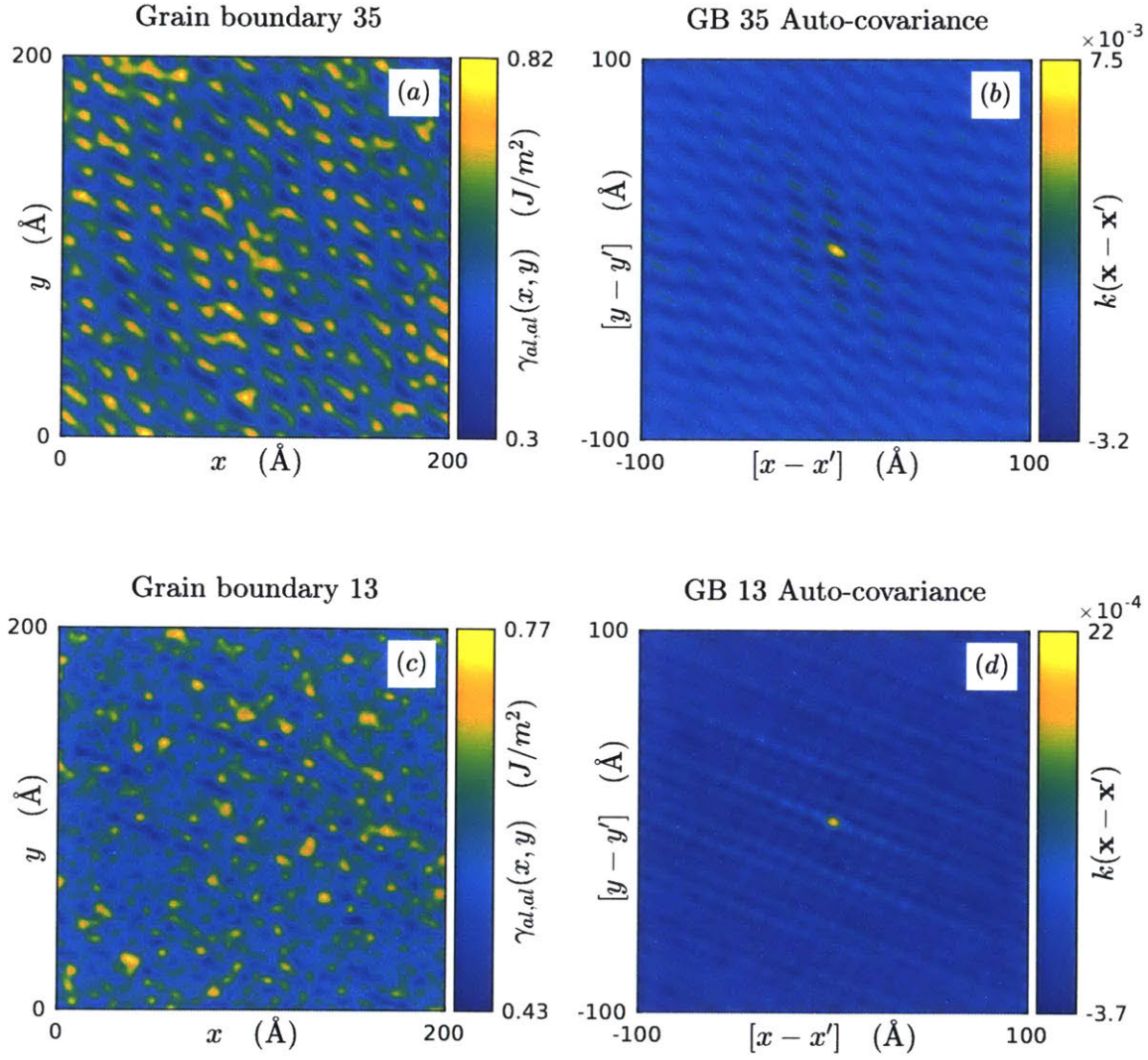

Figure 4-5: (*a*) LDGBE distribution $\gamma_{al,al}(\mathbf{x})$ for grain boundary 35. (*b*) Empirically calculated covariance function $k(\mathbf{x}-\mathbf{x}')$ for grain boundary 35. (*c*) LDGBE distribution $\gamma_{al,al}(\mathbf{x})$ for grain boundary 13. (*d*) Empirically calculated covariance function for $k(\mathbf{x}-\mathbf{x}')$ grain boundary 13. We can see that the quasi-periodic nature of the LDGBE distributions is captured in the covariance functions

$k(\mathbf{x} - \mathbf{x}')$. Then, the energy distribution $\gamma_{al,al}(\mathbf{x})$ is used as a seed to calculate new patches of the LDGBE distribution. The new patches are generated as samples from the Gaussian process approximation.

Figure 4-6 shows three steps of the recursive algorithm. Here, we are extrapolating an energy distribution of dimension 200Å×200Å to a final dimension 400Å×200Å. We start with the seed energy distribution $\gamma_{al,al}(\mathbf{x})$ being placed in the center of the larger domain. Points in the larger domain which lie on the seed are considered to be 'defined', and the points which are outside this seed area are considered 'undefined'. The 'undefined' points are shown with a solid blue patches. To generate a new segment of the energy map, we search for an 'undefined' point which has the largest number of 'defined' neighbors in a neighborhood with a maximum distance of ($\pm$100Å, $\pm$100Å). The neighborhood is marked with the red-dashed square.

The values of grain boundary energy at 'undefined' points within the selected neighborhood are generated as a sample from the Gaussian process approximation

$$\gamma_{al,al}(\mathbf{x}) \sim \mathcal{GP}(m, k(\mathbf{x}, \mathbf{x}')), \tag{4.40}$$

conditioned on the 'defined' data points within the neighborhood. The newly generated points are added to the list of 'defined' points, and the algorithm repeats till there are no more 'undefined' points.

Figures 4-6(b) and (c) show the second and third step of the extrapolation algorithm. We can see that the 'undefined' points from the previous steps are now 'defined'.

Figure 4-7 shows three extrapolated grain boundary energy maps which were generated using this algorithm. The central seed region, which was calculated using atomistic simulations, is outlined by a solid black line. We can visually see that the generated energy maps have the same quasi-periodic structure as the seeds.

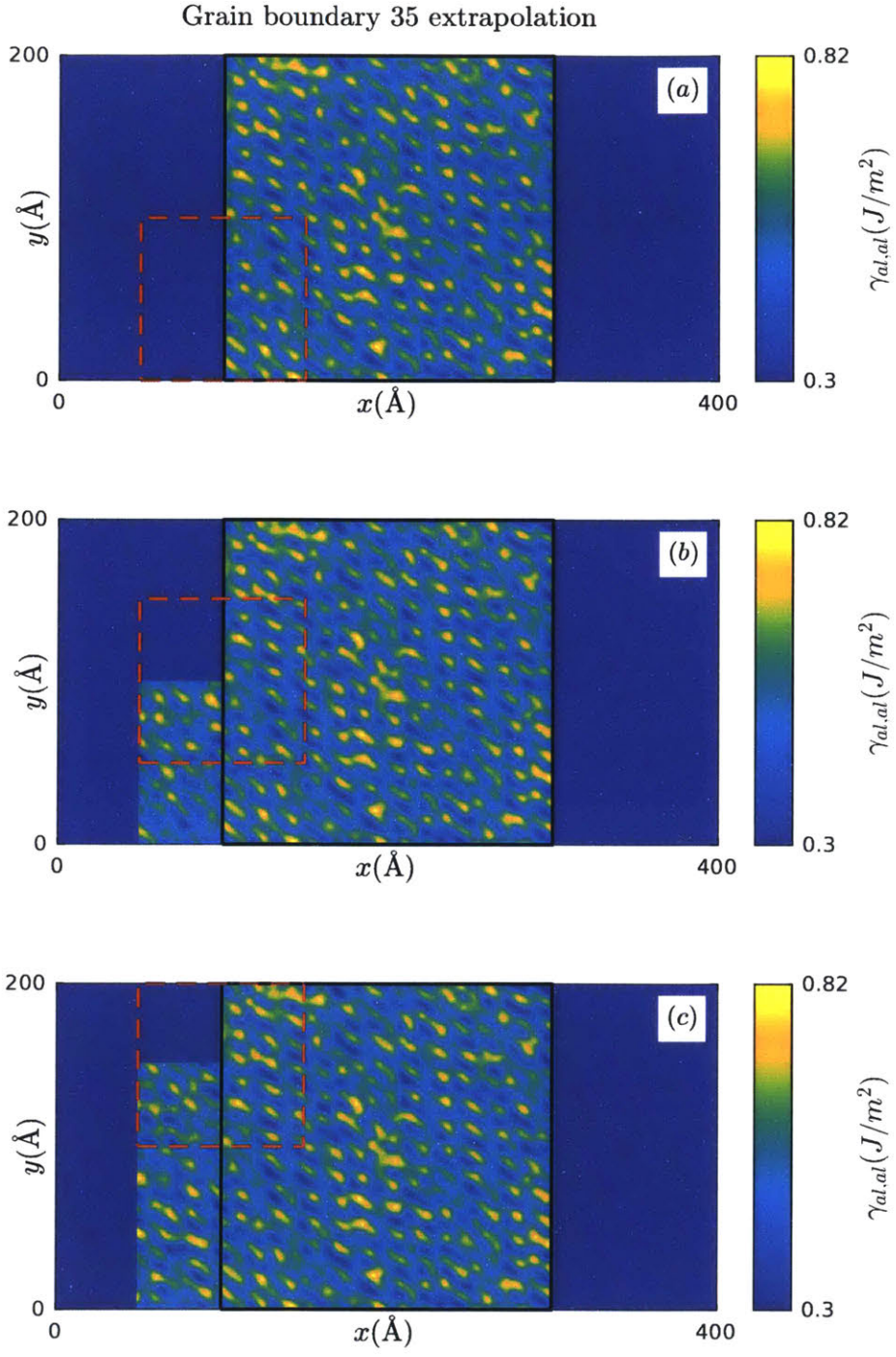

Figure 4-6: Three steps in the recursive extrapolation of the LDGBE distribution of grain boundary 35. (a) The initial step: The seed distribution is located in the center. The red-dashed square marks the extrapolation neighborhood. (b) LDGBE distribution after generation of first patch. The extrapolation neighborhood moves to the next location. (c) The energy distribution after two steps of extrapolation.

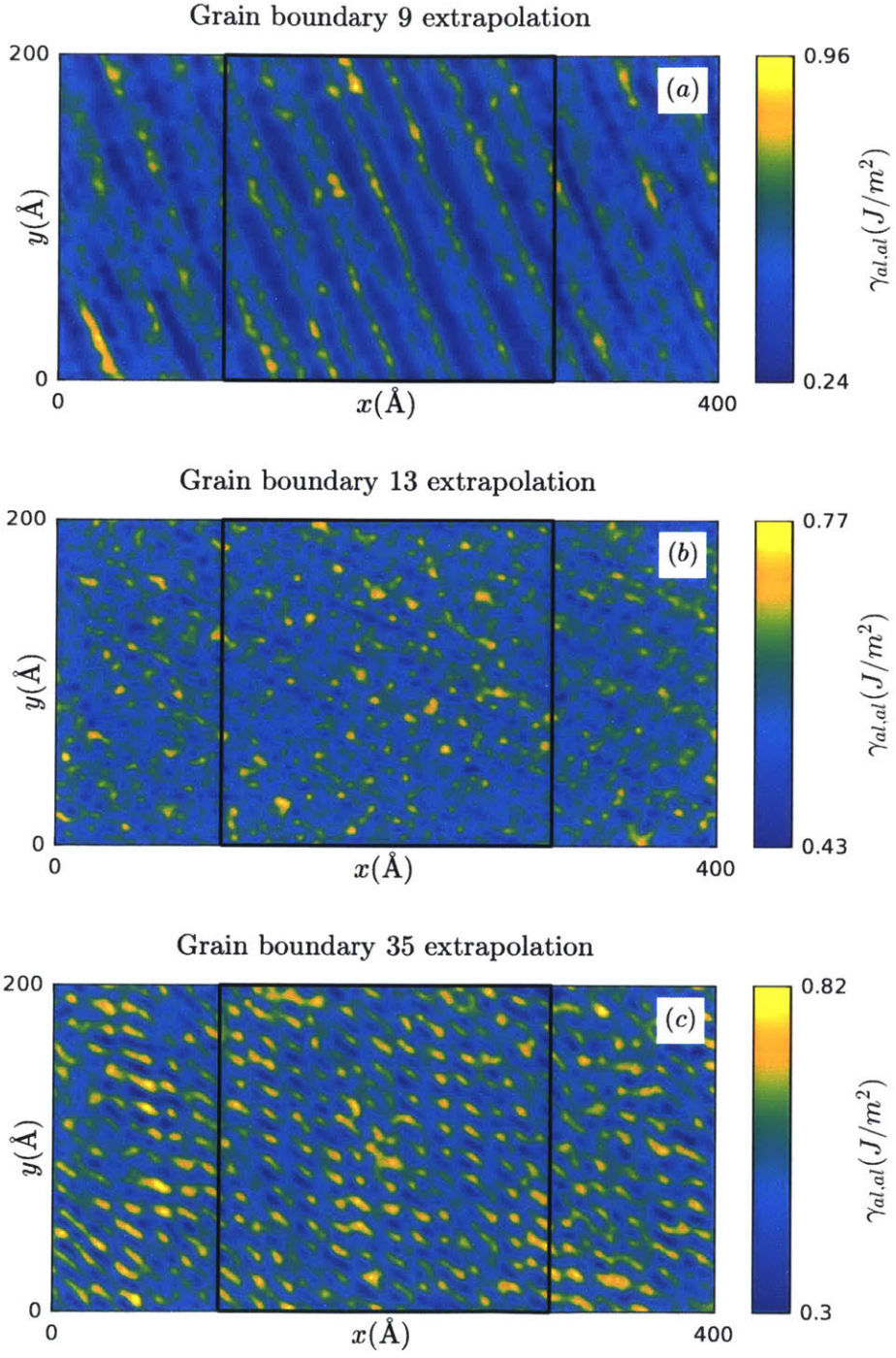

Figure 4-7: Extrapolated LDGBE distributions for (a) grain boundaries 9 ,(b) grain boundary 13, and (c) grain boundary 35. The sections of the distributions as calculated by atomistic simulations, and used as a seed for the extrapolation, are marked by black squares. The extrapolated sections of the LDGBE distributions have the same quasi-periodic structure as the seed.

4.3 Calculation of permeability map

The permeation of gallium through aluminum grain boundaries is driven by the reduction in interfacial energy when one aluminum-aluminum interface is replaced by two gallium-aluminum interfaces. We defined a permeability map $\beta(\mathbf{x})$ as

$$\beta(\mathbf{x}) = \gamma_{Al,Al}(\mathbf{x}) - 2\gamma_{Ga,Al}, \tag{4.41}$$

where $\gamma_{Al,Al}(\mathbf{x})$ is the location dependent grain boundary energy, and $\gamma_{Ga,Al}$ is the interfacial energy of gallium-aluminum interfaces. In section 4.2, we have constructed and extrapolated the LDGBE maps $\gamma_{Al,Al}(\mathbf{x})$.

Figures 4-8 and 4-9 show some of the permeation maps calculated as part of this study. The regions where $\beta(\mathbf{x}) > 0$, which serve as pathways for gallium permeation, are marked in red, with darked shades of red corresponding to larger positive values of $\beta(\mathbf{x})$. Regions where $\beta(\mathbf{x}) < 0$ serve as obstacles to the permeation of gallium. These areas are marked in blue, where darker shades of blue correspond to more negative values of $\beta(\mathbf{x})$.

Figure 4-8 shows the effect of the gallium-aluminum interfacial energy $\gamma_{Ga,Al}$ on the permeability map $\beta(\mathbf{x})$ for grain boundary 9. We can see that increasing the value of $\gamma_{Ga,Al}$ increases both the size, and the intensity of the obstacles. We can see that for $\gamma_{Ga,Al} = 0.15J/m^2$, the obstacles are *disconnected*. When $\gamma_{Ga,Al}$ increases to $0.2J/m^2$, the obstacles grow, and form *continuous* bands.

Figure 4-9 shows the permeability maps for grain boundaries 9, 13, and 35 at $\gamma_{Ga,Al} = 0.225J/m^2$. These grain boundaries were permeated at speeds $0.28\mu m/s$, $3.6\mu m/s$, and $0.49\mu m/s$, respectively. The grain boundaries have very different size, distribution, and intensity of obstacles. We can also see a qualitative relation between the distribution and size of obstacles, and the observed permeation velocities.

In chapter 5, we have developed a predictive phase field model, which simulates the permeation of gallium through aluminum for given permeability maps $\beta(\mathbf{x})$. In chapter 6, we will use the data collected by Hugo and Hoagland in [30] to infer the gallium-aluminum interfacial energy $\gamma_{Ga,Al}$, as well as the tension and thickness

parameters of the phase field model.

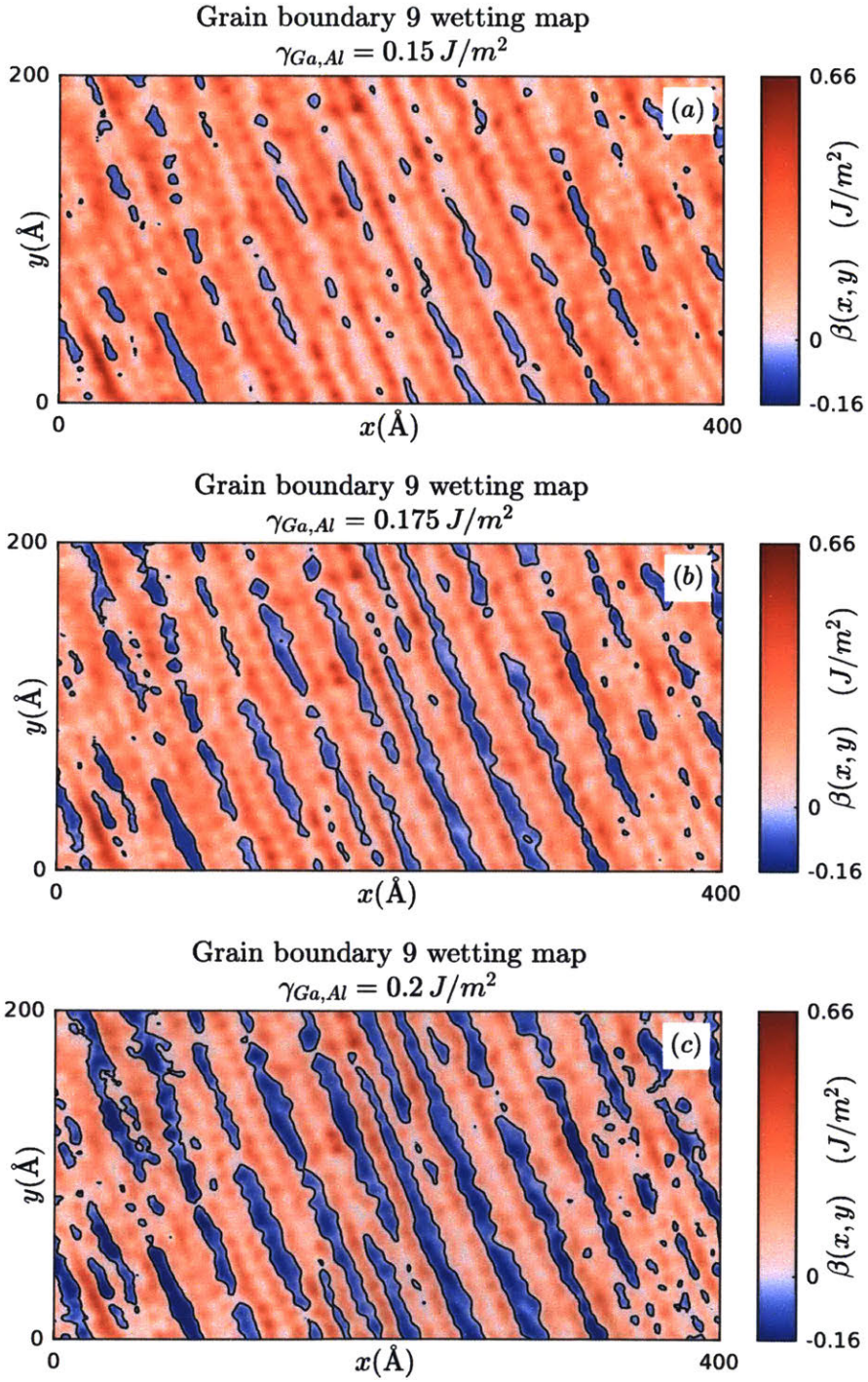

Figure 4-8: Effect of $\gamma_{Ga,Al}$ on permeability map $\beta(x, y)$ of grain boundary 9. (a) $\gamma_{Ga,Al} = 0.15J/m^2$, (b) $\gamma_{Ga,Al} = 0.175J/m^2$, and (c) $\gamma_{Ga,Al} = 0.2J/m^2$. Permeable regions of the grain boundary are shown in red, and the obstacles are shown in blue. The obstacles grow in size with $\gamma_{Ga,Al}$.

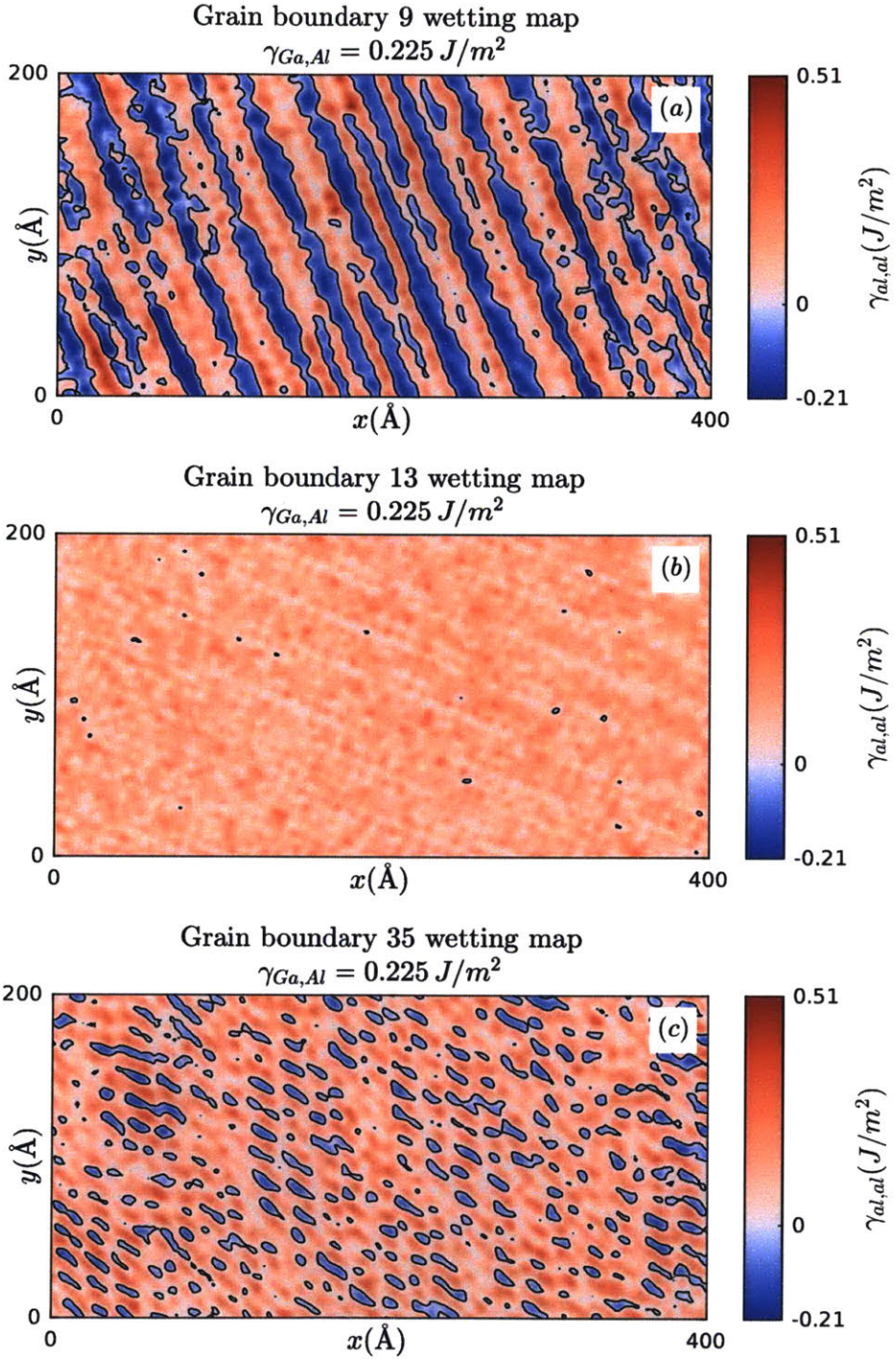

Figure 4-9: Permeability maps for (a) grain boundary 9, (b) grain boundary 13, and (c) grain boundary 35. The permeability maps were calculated for $\gamma_{Ga,Al} = 0.225 J/m^2$. The three grain boundaries have different size, distribution, and intensities of obstacles.

Chapter 5

Using phase field methods to simulate Ga permeation of Al

In chapter 3, we introduced and developed the phase field method. We showed that the Cahn-Hilliard equation can be used to model multi-phase physics, using spinodal decomposition as an example. Further, we showed that the parameters ϵ and α control the thickness δ and tension τ of the interface between the two phases being simulated.

In chapter 4 we calculated the location dependent grain boundary energy maps $\gamma_{Al,Al}(\mathbf{x})$ for 17 grain boundaries whose velocities were reported in [30]. Wetting maps $\beta(\mathbf{x})$, given by

$$\beta(\mathbf{x}) = \gamma_{Al,Al}(x) - 2\gamma_{Ga,Al} \tag{5.1}$$

drive the permeation of gallium through aluminum grain boundaries.

In this chapter, we will use the Cahn-Hilliard equation to simulate the permeation of gallium through aluminum grain boundaries. In section 5.1, we show the details of how we modified and solved the Cahn-Hilliard to simulate gallium permeation of aluminum grain boundaries. In section 5.2, we will show how we extracted permeation velocities from the results of the Cahn-Hilliard simulations. Finally, in section 5.3, we will discuss the effect of front thickness δ and front tension τ on the permeation speeds of gallium through different grain boundaries.

5.1 Cahn-Hilliard model

We use an order parameter field $\phi(\mathbf{x})$ to encode the state of permeation of the grain boundary being simulated. An example order parameter field is shown in figure 5-1. Regions of the grain boundary which have been permeated by gallium, shown in gray, have $\phi(\mathbf{x}) = -1$. Regions which are unpermeated by gallium, shown in red, have $\phi(\mathbf{x}) = 1$. The interfaces between these two regions, shown in white, have the order parameter value $-1 < \phi(\mathbf{x}) < 1$.

The behavior of the order parameter field $\phi(\mathbf{x})$ is controlled by the energy functional

$$E(\phi(\mathbf{x})) = \int_{\Omega} \left[g(\phi, \mathbf{x}) + \frac{\epsilon}{2} \|\nabla\phi\|^2 \right] d\mathbf{x}, \tag{5.2}$$

where Ω is the grain boundary region being simulated. The wetting map $\beta(\mathbf{x})$ is incorporated into the simulation using a location dependent potential function $g(\phi, \mathbf{x})$.

The evolution of the order parameter field $\phi(\mathbf{x})$ is dictated by the Cahn-Hilliard equation, given by

$$\frac{\partial\phi}{\partial t} = \nabla \cdot \left[M(\phi, \mathcal{M}) \nabla \left(\frac{\partial g(\phi, \mathbf{x})}{\partial\phi} - \epsilon\nabla^2\phi \right) \right]. \tag{5.3}$$

The use of the Cahn-Hilliard equation ensures that the order parameter field $\phi(\mathbf{x})$ remains conserved. The details of both the location dependent potential function, and the solution of the Cahn-Hilliard equation are presented below.

5.1.1 Modified potential function

The location dependent potential function $g(\phi, \mathbf{x})$ is a forth order polynomial with location dependent coefficients.

$$g(\phi, \mathbf{x}) = A(\mathbf{x})\phi^4 + B(\mathbf{x})\phi^3 + C(\mathbf{x})\phi^3 + D(\mathbf{x})\phi \tag{5.4}$$

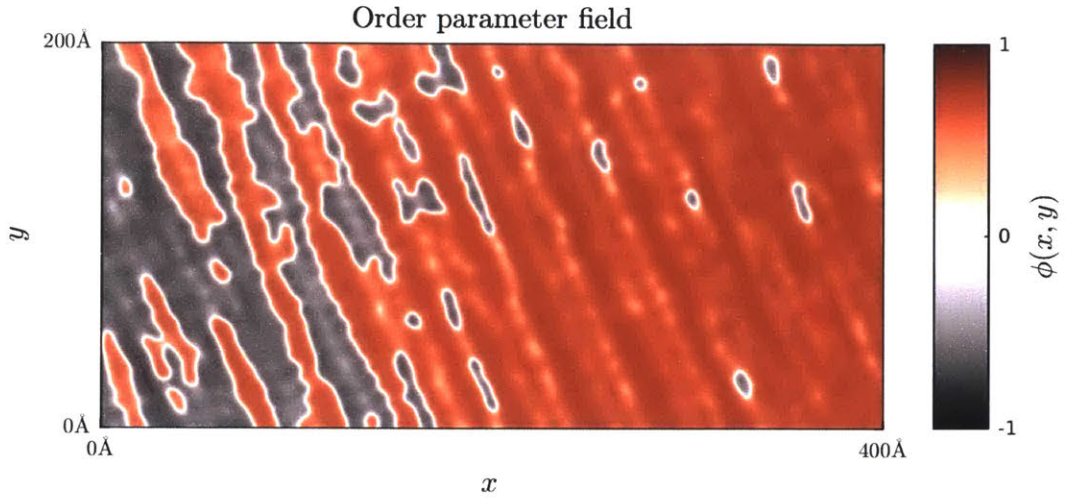

Figure 5-1: The order parameter field $\phi(x, y)$, representing the state of permeation of grain boundary 9. Regions of the grain boundary which have been permeated by gallium are shown in gray. Regions which are not permeated are shown in red. The permeated and unpermeated regions are separated by interfaces shown in white.

to calculate the coefficients $A(\mathbf{x}), B(\mathbf{x}), C(\mathbf{x})$, and $D(\mathbf{x})$, a non-linear curve-fitting problem is solved, with the following constraints.

$$g(1, \mathbf{x}) - g(-1, \mathbf{x}) = \beta(\mathbf{x}) \tag{5.5}$$

$$\int_{\phi_1}^{\phi_2} [g(\phi, \mathbf{x}) - l(\phi)]\, d\phi - = \alpha \tag{5.6}$$

$$\frac{\partial g(1, \mathbf{x})}{\partial \phi} = g'_{Al} \tag{5.7}$$

$$\frac{\partial g(-1, \mathbf{x})}{\partial \phi} = g'_{Ga} \tag{5.8}$$

Equation 5.5 controls the relative energetic favorability of the permeated phase ($\phi = -1$) and the unpermeated phase ($\phi = 1$). The permeated phase is energetically favorable as compared to the unpermeated phase in regions where $\beta(\mathbf{x}) > 0$.Conversely, the permeated phase is energetically less favorable than the unpermeated phase in regions where $\beta(\mathbf{x}) < 0$.

Equation 5.6 sets the energy barrier between the permeated and unpermeated phases. In this equation, ϕ_1 and ϕ_2 are the points of common tangency of the potential

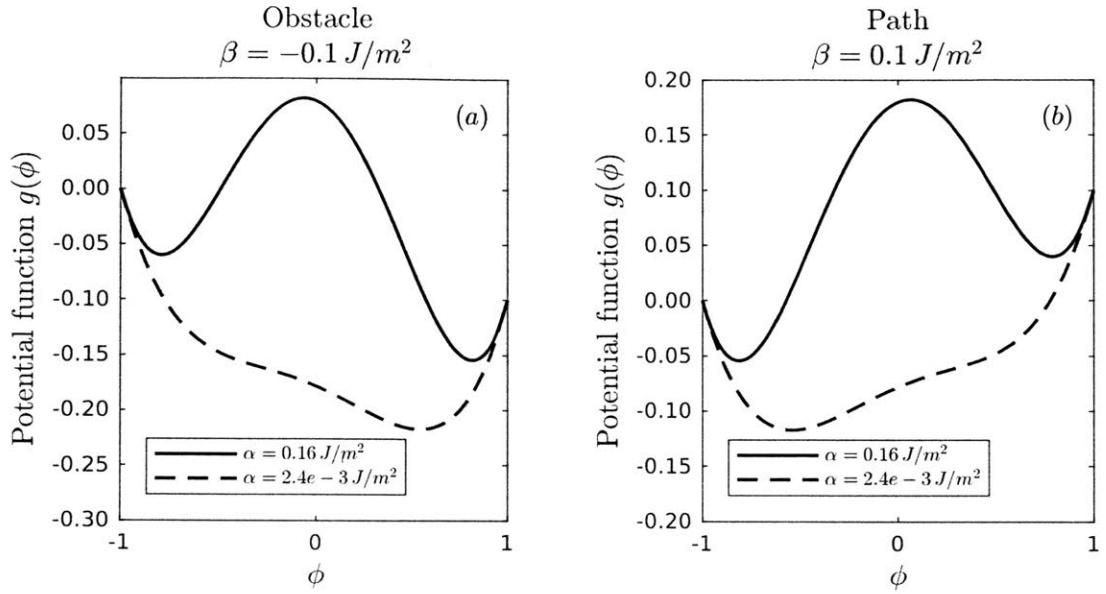

Figure 5-2: Modified potential function for different values of β and α. (a) The potential functions for $\beta = -0.1\,J/m^2$ are plotted with $\alpha = 0.16\,J/m^2$ and $\alpha = 2.4e-3\,J/m^2$. (b) The potential functions for $\beta = 0.1\,J/m^2$ are plotted with $\alpha = 0.16\,J/m^2$ and $\alpha = 2.4e-3\,J/m^2$. Potential functions with small values of α can be single welled.

$g(\phi, \mathbf{x})$, and $l(\phi)$ is the common tangent.

Figure 5-2(a) and (b) show the potential functions for $\beta = -0.1\,J/m^2$, and $\beta = 0.1\,J/m^2$ respectively. For each value of β, the potential functions are calculated with $\alpha = 0.16\,J/m^2$ and $\alpha = 2.4e-3\,J/m^2$. For negative values of β, the gallium phase $\phi = -1$ is less energetically favorable than the aluminum phase $\phi = 1$, as can be seen from figure 5-2(a). The converse can be seen in figure 5-2(b). We can see that the potential functions $g(\phi, \mathbf{x})$ are double welled for $\alpha = 0.16\,J/m^2$, that is, they have two local minima, separated by a local maximum. For $\alpha = 2.4e-3\,J/m^2$, the potential functions has a single minimum. However, the potential function still contains a common tangent, and a corresponding energy barrier. This is possible due to the prescribed gradient of the potential at $\phi = 1$ and $\phi = -1$, in equations 5.7 and 5.8. We have used values $g'_{Al} = 0.64\,J/m^2$ and $g'_{Ga} = -0.64\,J/m^2$ to calculate the location dependent potential functions.

5.1.2 Solving the Cahn-Hilliard equation

We have used the C++ library MOOSE to solve the Cahn-Hilliard equation. MOOSE, which stands for **M**ultiphysics **O**bject-**O**riented **S**imulation **E**nvironment, is a "... finite-element, multiphysics framework primarily developed by Idaho National Laboratory" [23, 61, 24]. MOOSE has been used as the simulation environment for diverse set of computional studies, such as the simulation of nuclear fuel rods [4, 22, 48], soil mechanics [54, 53, 9], and phase field models [34, 6, 59].

The Cahn-Hilliard equation is solved by splitting it into two coupled second order equations.

$$\frac{\partial \phi}{\partial t} = \nabla \cdot (M(\phi, \mathcal{M}) \nabla \mu) \tag{5.9}$$

$$\mu = \frac{\partial g(\phi, \mathbf{x})}{\partial \phi} - \epsilon \nabla^2 \phi \tag{5.10}$$

Both these equations were discretized on an adaptive spatial grid. We imposed the Dirichet boundary condition at the left edge ($x = 0$Å). The Dirichlet boundary condition is given by the equations

$$\phi = -1 \tag{5.11}$$

$$\mu = 0. \tag{5.12}$$

This boundary condition acts as a source of gallium. We imposed the Neumann boundary condition On the remaining boundaries, ($y = 0$Å), ($y = 200$Å), and ($x = 400$Å). The Neumann boundary condition is is given by the equations

$$\nabla \phi \cdot \hat{n} = 0 \tag{5.13}$$

$$\nabla \mu \cdot \hat{n} = 0. \tag{5.14}$$

We used a non-uniform phase dependent mobility

$$M(\phi, \mathcal{M}) = \mathcal{M} \left(5.5 + 4.5 \tanh \left(\frac{-0.6 - \phi}{0.1} \right) \right). \tag{5.15}$$

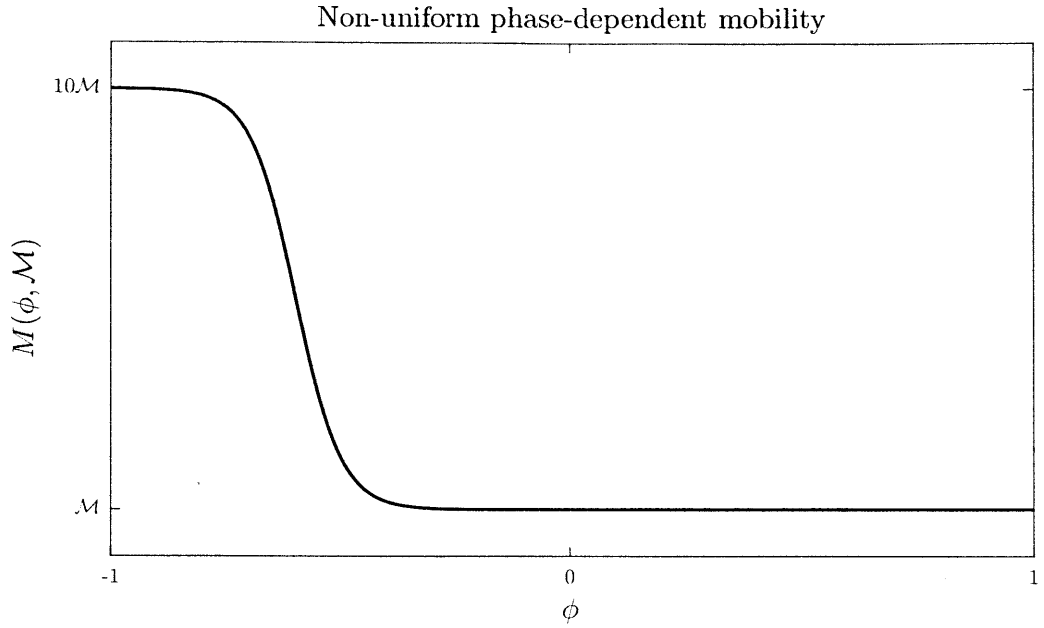

Figure 5-3: The non-uniform phase-dependent mobility used in this study. The mobility smoothly varies from $10\mathcal{M}$ to a baseline mobility of $\mathcal{M}$ as the phase changes from gallium to aluminum. This models the higher mobility of the liquid gallium compared to solid aluminum

Here, $\mathcal{M}$ is a baseline mobility for the system. Using the mobility function in equation 5.15 sets the mobility of the aluminum phase to $\mathcal{M}$, and that of the gallium phase to $10\mathcal{M}$, with a smooth variation in between. Doing so allows us to model the higher mobility of the liquid gallium phase compared to the solid aluminum phase. Changing the baseline mobility $\mathcal{M}$ is equivalent to rescaling time. Solving

$$\frac{\partial \phi}{\partial t} = \nabla \cdot \left[M(\phi, \mathcal{M}) \nabla \left(\frac{\partial g(\phi, \mathbf{x})}{\partial \phi} - \epsilon \nabla^2 \phi \right) \right] \tag{5.16}$$

is equivalent to solving

$$\frac{\partial \phi}{\partial \mathbf{t}^*} = \nabla \cdot \left[M(\phi, 1) \nabla \left(\frac{\partial g(\phi, \mathbf{x})}{\partial \phi} - \epsilon \nabla^2 \phi \right) \right] \tag{5.17}$$

where $\mathbf{t}^* = \mathcal{M} \times t$. Therefore, once a simulation has been conducted at a given value of $\mathcal{M}$, solutions for other values of $\mathcal{M}$ can be obtained by appropriately rescaling time.

Figures 5-5 and 5-7 show the simulation of gallium permeation through grain boundaries 9 and 35. The wetting maps $\beta(\mathbf{x})$, used for the simulations are shown in figures 6-12 and 5-6 respectively. Grain boundary 9 has large regions where $\beta(\mathbf{x}) < 0$. These regions act like obstacles to permeation. We can see that the gallium permeates only through the regions where $\beta(\mathbf{x}) > 0$, and forms islands of unpermeated aluminum in regions where $\beta(\mathbf{x}) < 0$. The permeated and unpermeated regions of the aluminum grain boundary are separated by interfaces of thickness

$$\delta = \sqrt{\frac{\epsilon}{\alpha}}, \tag{5.18}$$

and tension

$$\tau = \sqrt{\epsilon\alpha}. \tag{5.19}$$

For details on the calculation of the relation between thickness δ and tension τ, on the Cahn-Hilliard equation parameters ϵ and α, see section 3.4.

The simulation shown in 5-5 was performed with a low interface tension $\tau = 5e-12\,J/m$. The interface between the permeated regions and the unpermeated islands have an associated energy penalty $\approx \tau \times L$, where L is the total length of the interface region. As a result of the low value of τ, the additional energy penalty due to the formation of interface regions is small, and the gallium is able to permeate through the grain boundary, while leaving behind unpermeated islands.

Grain boundary 35 has smaller obstacles compared to grain boundary 9. We can see that the gallium permeates the grain boundary with a well defined front, and leaves behind no islands of unpermeated aluminum, unlike grain boundary 9. This simulation was run with a large interface tension $\tau = 1e-10\,J/m$. As a result, the energy penalty $\tau \times L$ is larger than the energy penalty of wetting the non-permeable regions $\beta(\mathbf{x}) < 0$. This allows the gallium to permeate without leaving behind unpermeated islands.

These two simulations show two qualitatively different gallium permeation mechanisms. The behavior seen in figure 5-5 can be described as diffusion and coalescence. The behavior seen in figure 5-7 can be defined as front propagation.

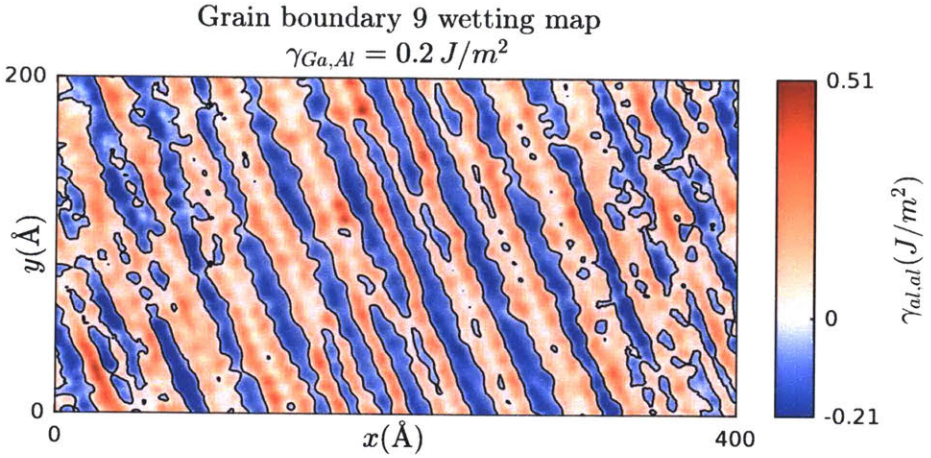

Figure 5-4: The grain boundary wetting map $\beta(\mathbf{x})$ used in figure 5-5.

5.2 Extraction of permeation velocity

We use the results of the Cahn-Hilliard equation to calculate the permeation velocity of gallium. To do so, we first spatially average the order parameter field at each time step. This gives us a time varying, average order parameter value $\bar{\phi}(t)$

$$\bar{\phi}(t) = \int_{\Omega} \phi(\mathbf{x}, t) \tag{5.20}$$

We run the Cahn-Hilliard simulation till convergence. In practice, we have found that running the simulation till $t = 10^9\ s$ is sufficient to achieve convergence for all grain boundaries. We use the converged value $\bar{\phi}(\infty)$ to determine if a grain boundary has been permeated or not. A grain boundary which has been completely permeated by gallium would have $\bar{\phi}(\infty) = -1$. However, as can be seen in figure 5-5, some grain boundaries have islands of unpermeated aluminum, which makes $\bar{\phi}(\infty) > -1$. To accommodate such cases, a grain boundary is determined to be permeated if

$$\bar{\phi}(\infty) < 0.3 \tag{5.21}$$

For grain boundaries which were determined to be permeated, the time varying location of gallium in the aluminum grain boundary was calculated using a linear

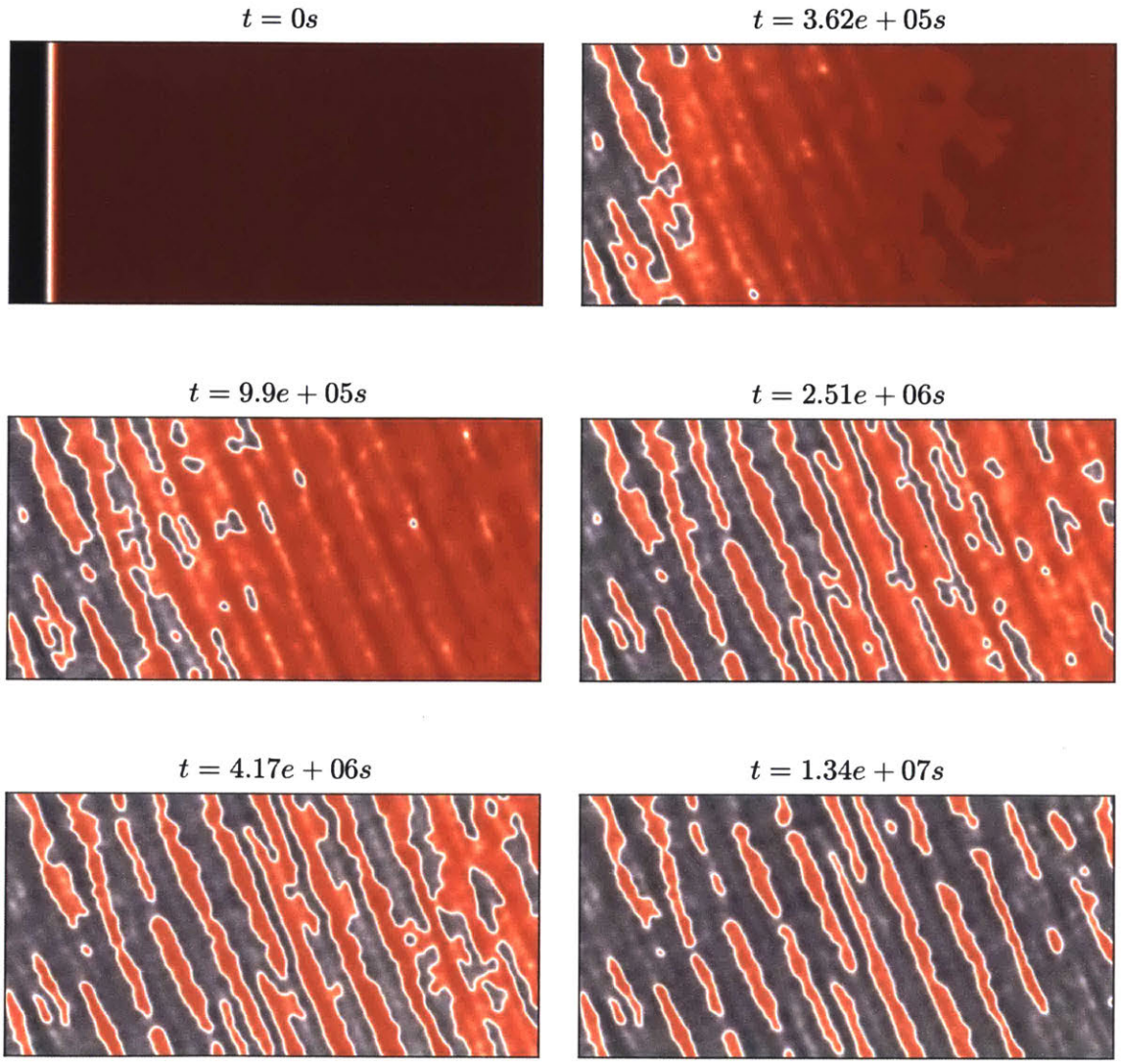

Figure 5-5: Permeation of gallium through grain boundary 9 for $\tau = 5e{-}12\ J/m$. The wetting map for this simulation is shown in figure 6-12. We can see that the gallium permeates the grain boundary without wetting the obstacles in the grain boundary.

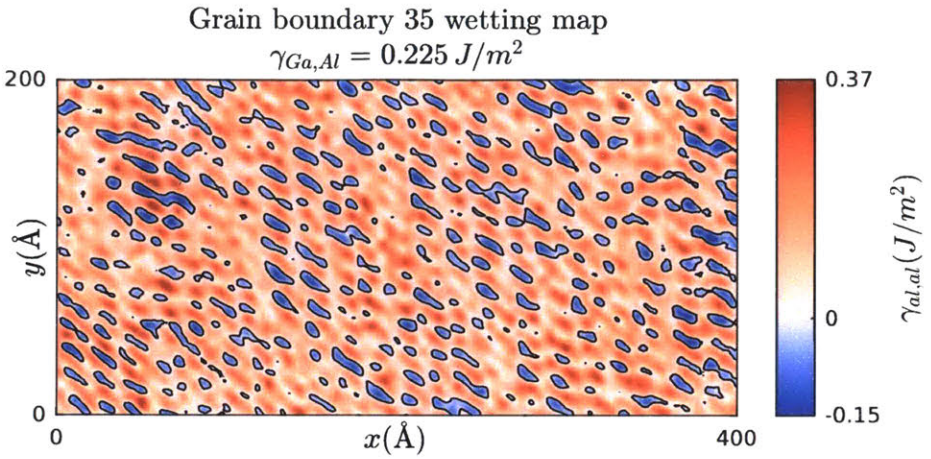

Figure 5-6: The grain boundary wetting map $\beta(\mathbf{x})$ used in figure 5-7.

relation between $\bar{\phi}(t)$ and the gallium location $X_{Ga}(t)$.

$$X_{Ga}(t) = \frac{1 - \bar{\phi}(t)}{1 - \bar{\phi}(\infty)} \times 400\text{Å} \tag{5.22}$$

This relation linearly maps $\bar{\phi} = 1$ to $X_{Ga} = 0$Å, and $\bar{\phi} = \bar{\phi}(\infty)$ to $X_{Ga} = 400$Å.

Figure 5-8 shows an example average order parameter $\bar{\phi}(t)$, and the computed gallium location $X_{Ga}(t)$. From the figure, we can see that the gallium permeates the aluminum grain boundary with a decreasing velocity. This is because the gallium permeation is limited by the diffusive transport of gallium from the Dirichlet boundary condition at $x = 0$Å.

We calculated the permeation velocity by fitting a straight line to the $X_{Ga}(t)$ curve for X_{Ga} satisfying

$$150\text{Å} < X_{Ga} < 250\text{Å}. \tag{5.23}$$

By using X_{Ga} values in this range, we are able to avoid any boundary effects caused by the boundary conditions at $x = 0$Å and $x = 400$Å.

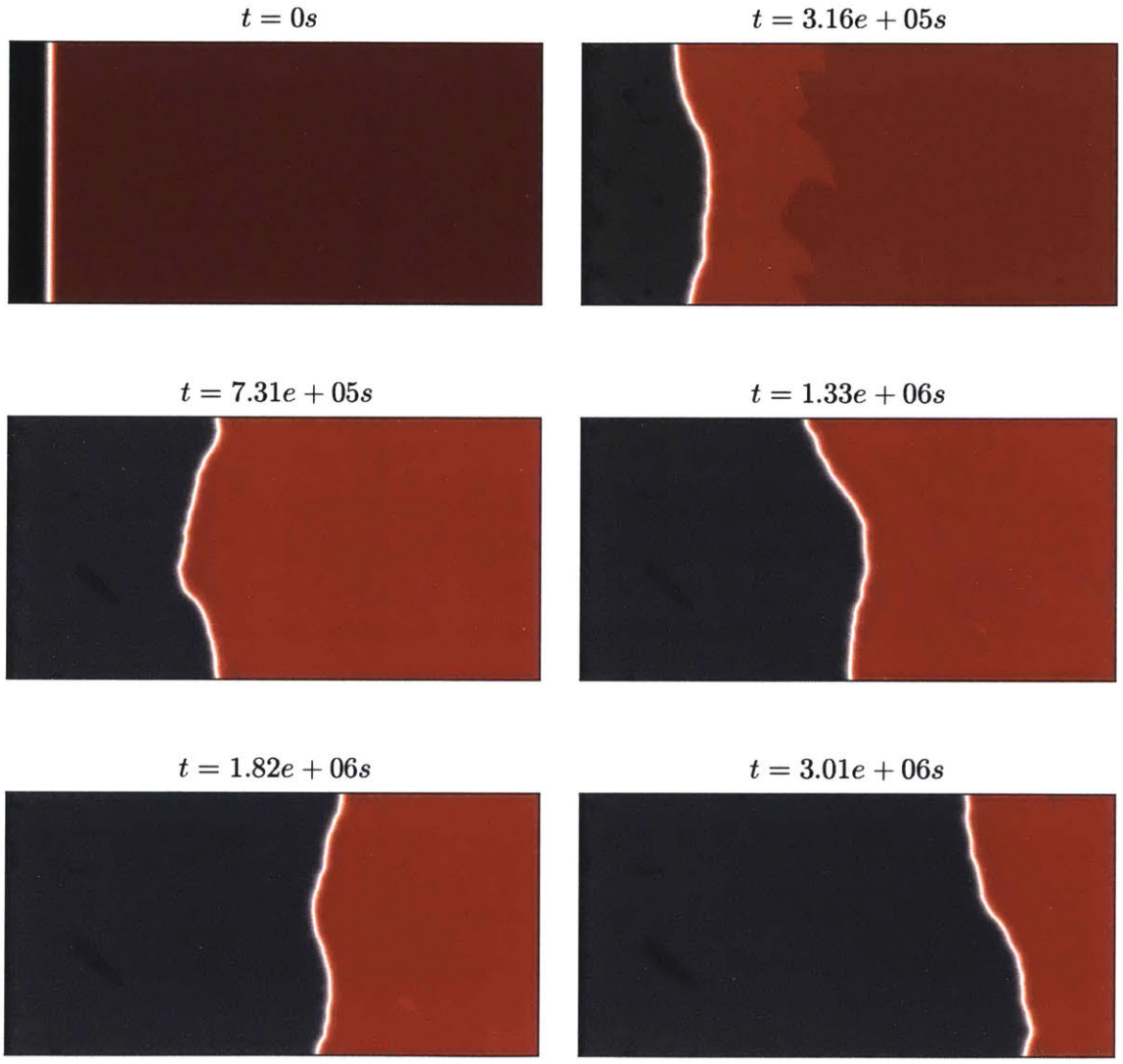

Figure 5-7: Permeation of gallium through grain boundary 35 for $\tau = 1e - 10\,J/m$. The wetting map for this simulation is shown in figure 5-6. The gallium permeated this grain boundary as a single front, without leaving behind any unpermeated islands.

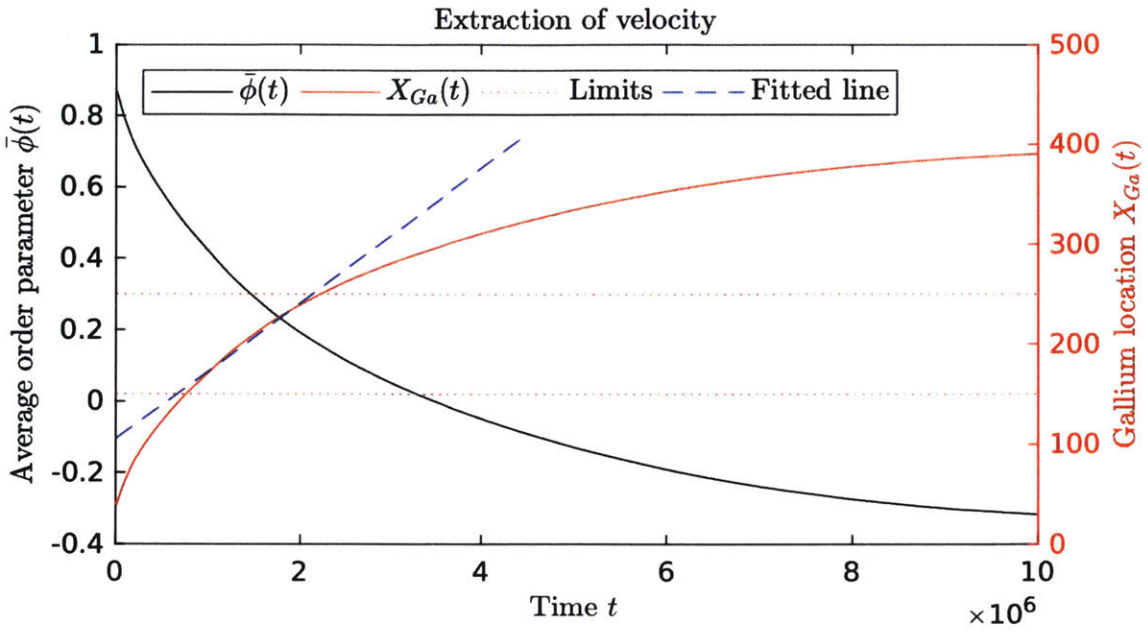

Figure 5-8: The calculation of velocity from the average order parameter $\bar{\phi}(t)$. The black solid line shows $\bar{\phi}(t)$. The position $X_{Ga}(t)$ is calculated by linearly mapping $\bar{\phi}(t)$ to locations along the simulation domain. The velocity is calculated by performing a linear fit on $X_{Ga}(t)$ for values of $X_{Ga}(t)$ between the limits 150Åand 250Å.

5.3 Effect of $\gamma_{Ga,Al}$, τ, and δ on permeation velocity

We now have a complete model for the gallium permeation of aluminum. The velocity of permeation V_{Ga} is calculated using a Cahn-Hilliard model.

$$V_{Ga} = F(\beta(\mathbf{x}), \delta, \tau, \mathcal{M}) \tag{5.24}$$

The Cahn-Hilliard model $F(.)$ has four inputs: a location dependent wetting map $\beta(\mathbf{x})$, interface thickness δ, interface tension τ, and a baseline mobility $\mathcal{M}$. The interface thickness δ and interface tension τ are controlled by the parameters ϵ and α. The location dependent wetting map $\beta(\mathbf{x})$ is calculated as

$$\beta(\mathbf{x}) = \gamma_{Al,Al}(\mathbf{x}) - \gamma_{Ga,Al}. \tag{5.25}$$

The gallium-aluminum interface energy $\gamma_{Ga,Al}$ is a third unknown parameter, along with δ and τ. The location dependent grain boundary energy $\gamma_{Al,Al}(\mathbf{x})$ was calculated

in chapter 4. It is a function of grain boundary crystallography $(g_{AB}, \hat{n})$.

$$\gamma_{Al,Al}(\mathbf{x}) = G(g_{AB}, \hat{n}) \tag{5.26}$$

Here, $G(.)$ is an atomistic simulation used to calculate $\gamma_{Al,Al}(\mathbf{x})$.

Figures 5-9 and 5-10 show the effect of $\gamma_{Ga,Al}$, tension τ, and thickness δ, on the permeation velocity V_{Ga} in grain boundaries 16 and 32 respectively. In figures 5-9(b), (d), and (f), we can see that grain boundary 16 has no obstacles, which are regions where $\beta(\mathbf{x}) < 0$, for any value $\gamma_{Ga,Al}$. On the other hand grain boundary 32 has obstacles in its wetting map, which can be seen in figures 5-10(b), (d), and (f). These obstacles grow in size with increasing values of $\gamma_{Ga,Al}$.

In figures 5-9(a), (c), and (e), we can see that the dependence of permeation velocity V_{Ga} on the thickness δ and tension τ is qualitatively similar for all value of $\gamma_{Ga,Al}$. The maximum permeation velocity is seen at low δ and moderate τ, and the minimum values are seen at high δ and low τ. The maximum permeation drops from $V_{Ga} = 1.87\,\mu m/s$ to $V_{Ga} = 1.50\,\mu m/s$, when $\gamma_{Ga,Al}$ is increased from $0.15\,J/m^2$ to $0.1875\,J/m^2$. This is due to a reduction in the wetting potential $\beta(\mathbf{x})$.

The relation between $\gamma_{Ga,Al}$, δ, and τ is more complicated for grain boundary 32. We can see from figures 5-10(a), (c), and (e), that the relation between thickness δ and tension τ, and the permeation velocity V_{Ga} is qualitatively different for different values of $\gamma_{Ga,Al}$. These qualitative differences arise from the change in size of obstacles in the wetting map $\beta(\mathbf{x})$ as a function of $\gamma_{Ga,Al}$, and the interaction of these obstacles with the permeating gallium.

For $\gamma_{Ga,Al} = 0.15\,J/m^2$, the highest permeation velocity occurs at $(\delta, \tau) = (26.4\text{Å}, 1.94e-10\,J/m)$. The permeation velocity is non-zero for all values of (δ, τ). Upon increasing the value of $\gamma_{Ga,Al}$ to $0.175\,J/m^2$, we see that the permeation velocity drops to zero for simulations with low thickness δ, and high tension τ. This is because in simulations with high tension τ, gallium gets pinned by the larger obstacles, and is not able to permeate the aluminum. The simulations with non-zero permeation velocities are those with low values of tension τ, where the gallium is able to permeate between

the obstacles, and for high values of thickness δ, where the gallium 'averages' over the obstacles in the wetting map. At $\gamma_{Ga,Al} = 0.1875\, J/m^2$, on simulation with low thickness δ and tension τ are able to permeate the grain boundaries.

Thus we can see that the parameter $\gamma_{Ga,Al}$, δ, and τ affect the permeation speed V_{Ga} differently for grain boundaries with obstacles, such as grain boundary 32, and grain boundaries without obstacles, such as grain boundary 16. The permeation speeds are a more sensitive to the thickness δ and tension τ in grain boundaries with large obstacles. In the next chapter, we will infer these parameters using the gallium permeation data experimentally observed by Hugo and Hoagland [29, 28, 30].

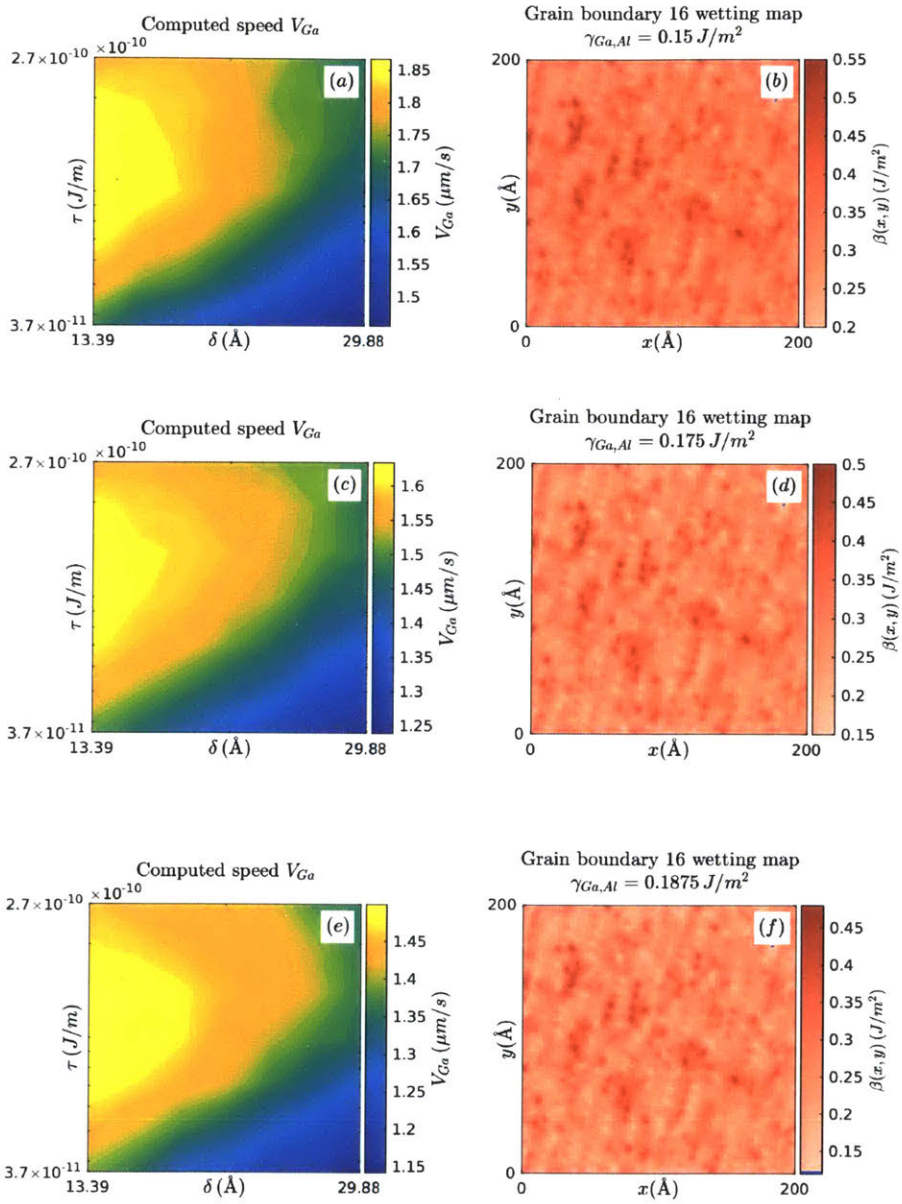

Figure 5-9: Wetting maps and permeation speeds for grain boundary 16. (a), (c), and (e) show the effect of $\gamma_{Ga,Al}$, δ, and τ on the permeation speed V_{Ga} for grain boundary 16. (b), (d), and (f) show the wetting maps $\beta(\mathbf{x})$ for the three values of $\gamma_{Ga,Al}$. We can see that there are no obstacles present in the wetting maps. As a result, the relation between V_{Ga}, and δ and τ is qualitatively similar for all values of $\gamma_{Ga,Al}$.

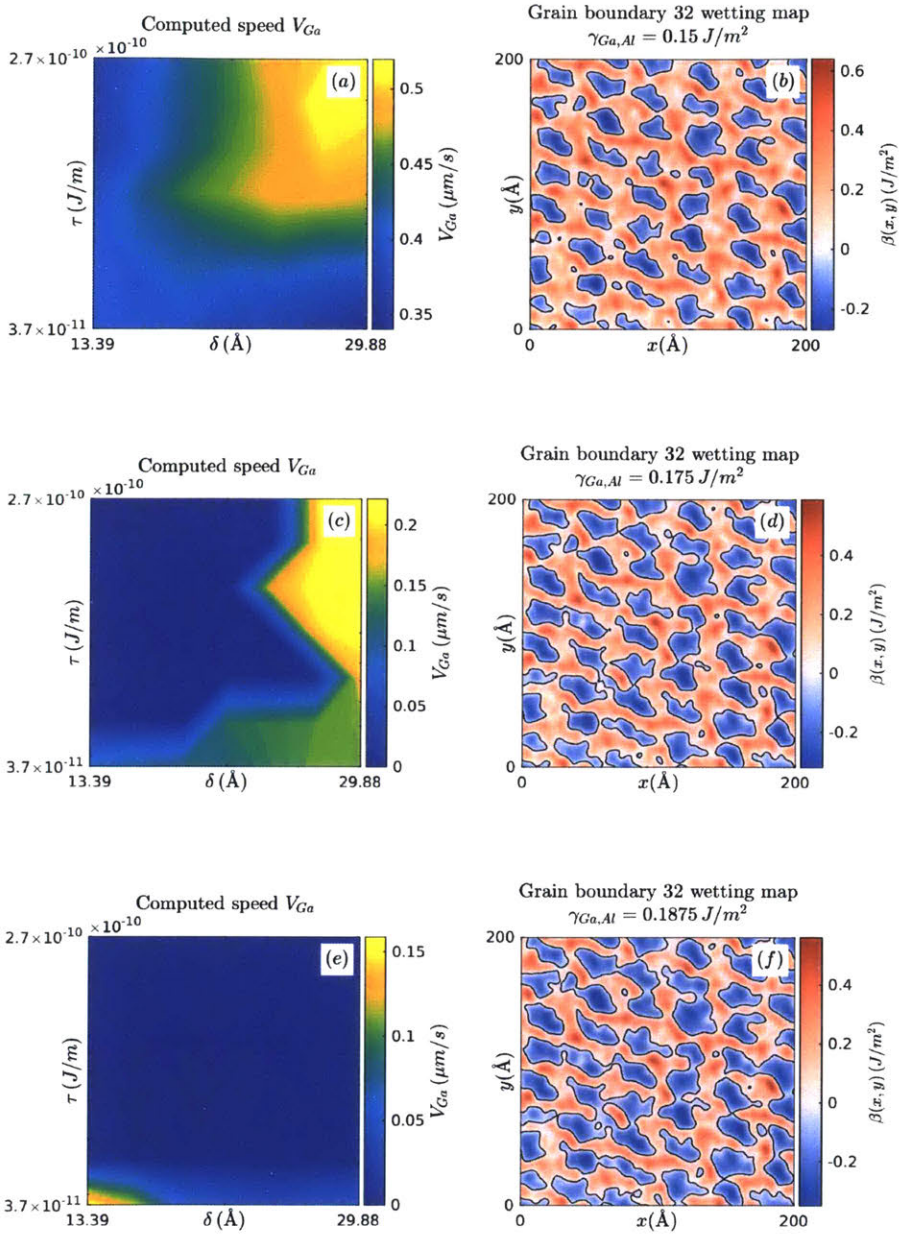

Figure 5-10: Wetting maps and permeation speeds for grain boundary 16. (a), (c), and (e) show the effect of $\gamma_{Ga,Al}$, δ, and τ on the permeation speed V_{Ga} for grain boundary 32. (b), (d), and (f) show the wetting maps $\beta(\mathbf{x})$ for the three values of $\gamma_{Ga,Al}$. The relationship between V_{Ga}, and δ and τ is qualitatively distinct for the different values of $\gamma_{Ga,Al}$. This is due to the presence of obstacles in the wetting maps.

Chapter 6

Inference of model parameters

We have developed a model for the gallium permeation of aluminum grain boundaries. The predicted velocity of permeation V_{Ga}^{P} for a given grain boundary is calculated using a Cahn-Hilliard model $F(.)$.

$$V_{Ga}^{P} = F(\beta(\mathbf{x}), \delta, \tau, \mathcal{M}) \tag{6.1}$$

The Cahn-Hilliard model takes in four inputs: a location dependent wetting map $\beta(\mathbf{x})$, interface thickness δ, interface tension τ, and a baseline mobility $\mathcal{M}$. The location dependent wetting map $\beta(\mathbf{x})$ is calculated as

$$\beta(\mathbf{x}) = \gamma_{Al,Al}(\mathbf{x}) - \gamma_{Ga,Al}. \tag{6.2}$$

The gallium-aluminum interface energy $\gamma_{Ga,Al}$ is a third unknown parameter, along with δ and τ. The location dependent grain boundary energy $\gamma_{Al,Al}(\mathbf{x})$ is a function of grain boundary crystallography, and is calculated using an atomistic model.

$$\gamma_{Al,Al}(\mathbf{x}) = G(g_{AB}, \hat{n}). \tag{6.3}$$

In this chapter, we will use Bayesian inference to infer the unknown parameters $\gamma_{Ga,Al}$, δ, τ, and $\mathcal{M}$ using experimental data collected by Hugo and Hoagland [30].

Bayesian inference is a statistical framework for inferring parameters θ of a model

$M(.)$ using experimental data $\mathcal{D}$. In Bayesian inference, unknown parameters are modeled as random variables [60]. The probability density function (PDF) of θ, $p(\theta)$ encodes our state of belief in the value of θ. Estimates of θ, and the uncertainty in those estimates can be calculated from the PDF.

To infer parameters θ using experimental data $\mathcal{D}$, we calculate the *conditional* PDF, $p(\theta|\mathcal{D})$. This conditional distribution, called the *posterior*, encodes our state of belief in the value of θ, *after* observing data $\mathcal{D}$. We can use Bayes' rule [1] to calculate the posterior as

$$\overbrace{p(\theta|\mathcal{D})}^{\text{Posterior}} = \frac{\overbrace{p(\mathcal{D}|\theta)}^{\text{Likelihood}}\overbrace{p(\theta)}^{\text{Prior}}}{\underbrace{p(\mathcal{D})}_{\text{Evidence}}} \tag{6.4}$$

The calculate the posterior, we need three distributions: The prior $p(\theta)$, the likelihood $p(\mathcal{D}|\theta)$, and the evidence $p(\mathcal{D})$. The evidence is simply a normalizing term

$$p(\mathcal{D}) = \int_{\Theta} p(\mathcal{D}|\theta)p(\theta)d\theta, \tag{6.5}$$

which ensures that the posterior is a proper PDF, that is,

$$\int_{\Theta} p(\theta|\mathcal{D})d\theta = 1 \tag{6.6}$$

The prior $p(\theta)$ encodes any belief we have about the parameter, before the observation of data $\mathcal{D}$. This prior belief can arise from a number of source, such as constraints that θ must obey, expert opinion, and even pre-existing data. For instance, if θ is a temperature measured in Kelvin, then θ has to be a non-negative number. This can be enforced by setting

$$p(\theta)|_{\theta<0} = 0 \tag{6.7}$$

The likelihood $p(\mathcal{D}|\theta)$ encodes the likelihood of observing data $\mathcal{D}$ at parameter value θ. The model $M(.)$ relates parameters θ with observed data $\mathcal{D}$ through the

[1] Hence *Bayesian* inference

relation

$$\overbrace{\mathcal{D}}^{\text{Observation}} = \overbrace{M(\theta)}^{\text{Prediction}} + \overbrace{\eta}^{\text{Uncertainty}} . \tag{6.8}$$

η is a random variable that accounts for sources of uncertainty in the model $M(.)$. These sources of uncertainty include noise in the experimental observations, unmodeled dynamics in the predictive model, and inherent stochasticity in the system being modeled. η is distributed according to

$$\eta \sim p_\eta(.) \tag{6.9}$$

Using the model $M(.)$ and the uncertainty model η, we can calculate the likelihood $p(\mathcal{D}|\theta)$ as

$$p(\mathcal{D}|\theta) = p_\eta(\mathcal{D} - M(\theta)). \tag{6.10}$$

In this study, the model parameters θ are the gallium-aluminum interface energy $\gamma_{Ga,Al}$, thickness δ, tension τ, and baseline mobility $\mathcal{M}$.

$$\theta = (\gamma_{Ga,Al}, \delta, \tau, \mathcal{M}) \tag{6.11}$$

The data $\mathcal{D}$ is the set of observed permeation velocities V_{Ga}^{O}, and the associated location dependent grain boundary energy $\gamma_{Al,Al}(\mathbf{x})$.

$$\mathcal{D} = \{(\gamma_{Al,Al}(\mathbf{x}), V_{Ga}^{O})_i\} \tag{6.12}$$

$$i = [9, 10, 11, 13, 16, 17, 20, 21, 22, 23, 27, 29, 31, 32, 34, 35, 37] \tag{6.13}$$

Here, i are the row numbers for the data used, as published by Hugo and Hoagland [30]. The permeation speeds V_{Ga}^{O} were directly reported, while the $\gamma_{Al,Al}(\mathbf{x})$ distributions were calculated from the crystallography data. In the remainder of this chapter, we will discuss the details of the Bayesian inference process used.

6.1 Likelihood

We have used a log-normal [33] noise model to construct our likelihood. In our model, the permeation velocity V_{Ga}^{P} predicted by the Cahn-Hilliard model, and the permeation velocity V_{Ga}^{O} observed experimentally by Hugo and Hoagland [30] are related to each other by the equation

$$\log(V_{Ga}^{O}/V_{Ga}^{P}) = \eta, \tag{6.14}$$

where η is normally distributed.

$$\eta \sim N(\mu, \sigma^2) \tag{6.15}$$

This noise model can be rewritten as an additive Gaussian noise model on the *logarithms* of observed and predicted velocities.

$$\log(V_{Ga}^{O}) = \log(V_{Ga}^{P}) + \eta \tag{6.16}$$

From this noise model, we can calculate the likelihood as

$$p(\mathcal{D}|\theta) = \frac{1}{\sqrt{2\pi\sigma^2}} \exp\left(-\frac{\left(\log(V_{Ga}^{0}) - \log(V_{Ga}^{P})\right)^2}{2\sigma^2}\right). \tag{6.17}$$

The likelihood is shown in figures 6-1(a) and (b). We have used a log-normal noise model with $\mu = 0$ and $\sigma^2 = 2.25$.

We picked this noise model for the following reasons:

1. Hugo and Hoagland observed permeation velocities which vary over four orders of magnitude. The lowest non-zero velocity observed is $0.001\,\mu m/s$ for grain boundary 37, and the highest velocity is $12.7\,\mu m/s$ for grain boundary 16. Using the logarithm of velocity for our noise model allows us to have sufficient resolution for all velocity values.

2. The log-normal distribution is a heavy-tail distribution, as can be seen in figure

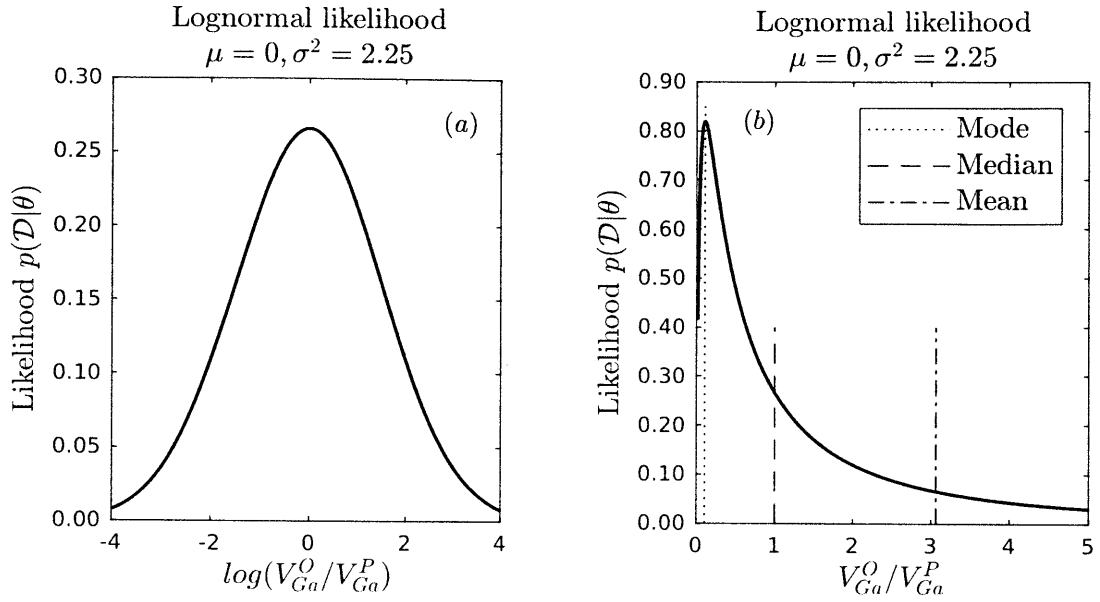

Figure 6-1: Log-normal likelihood function. (a) The log-normal likelihood is a additive Gaussian noise on the logarithm of the velocities. (b) The log-normal distribution is a heavy-tail distribution.

6-1(b). This property of the log-normal distribution makes the inference robust to the presence of outliers in the data.

6.2 Prior

The prior $p(\gamma_{Ga,Al}, \delta, \tau)$ was constructed as the product of three independent priors.

$$p(\gamma_{Ga,Al}, \delta, \tau, \mathcal{M}) = p(\gamma_{Ga,Al})p(\delta)p(\tau)p(\mathcal{M}) \tag{6.18}$$

Figures 6-2, 6-4, and 6-3 show the prior distributions for $\gamma_{Ga,Al}$, δ, and τ respectively.

We can easily argue that $\gamma_{Ga,Al}$ is a positive number. We know that the location dependent grain boundary energy $\gamma_{Al,Al}(\mathbf{x}) > 0$ for all grain boundaries, at all locations $\mathbf{x}$. This is because the grain boundary is a planar defect in a crystal, and has a positive associated energy. Hence, if the gallium-aluminum interface energy $\gamma_{Ga,Al} <= 0$, then the wetting potential $\beta(\mathbf{x}) > 0$ for all grain boundaries, at all locations $\mathbf{x}$. This would imply that there are no obstacles to gallium permeation in

any grain boundary, since obstacles to permeation exist in regions where $\beta(\mathbf{x}) < 0$. Hence, all grain boundaries would necessarily be permeated, albeit at different speeds. However, we know that this is not the case. Grain boundary 21 observed by Hugo and Hoagland was not permeated by gallium. Therefore, $\gamma_{Ga,Al} > 0$.

Using a similar argument, we can find an upper bound. $\gamma_{Ga,Al}$ is necessarily less than half the maximum value of $\gamma_{Al,Al}(\mathbf{x})$ across all grain boundaries.

$$\gamma_{Ga,Al} < \frac{1}{2}\max(\gamma_{Al,Al}(\mathbf{x})_i), \tag{6.19}$$

where i is the index of grain boundaries. This upper bound was found to be $0.537\ J/m^2$. If $\gamma_{Ga,Al} > 0.537\ J/m^2$, $\beta(\mathbf{x})$ will be a negative number for all grain boundaries, which would imply that *no* grain boundaries can be permeated by gallium. Again, we know from literature that this is not true.

These two arguments give us broad constraints on the range of values $\gamma_{Ga,Al}$ can take. We have used a uniform prior on the value of $\gamma_{Ga,Al}$, constrained between $0.15 J/m^2$ and $0.2 J/m^2$.

$$\gamma_{Ga,Al} \sim \mathcal{U}(0.15\ J/m^2, 0.2\ J/m^2) \tag{6.20}$$

$$p(\gamma_{Ga,Al}) = \begin{cases} 20, & 0.15\ J/m^2 < \gamma_{Ga,Al} < 0.2\ J/m^2 \\ 0, & \text{Otherwise} \end{cases} \tag{6.21}$$

We have used dimensional arguments to estimate the approximate value of the tension τ.

$$\mathcal{O}(\tau) \approx \mathcal{O}(\beta)\mathcal{O}(d), \tag{6.22}$$

where $\mathcal{O}(\beta)$ is the approximate wetting potential of obstacles and paths, and $\mathcal{O}(d)$ is approximate length scale of the obstacles and paths in the wetting map $\beta(\mathbf{x})$. Substituting $\mathcal{O}(\beta) \approx 0.1 J/m^2$ and $\mathcal{O}(d) \approx 10\text{Å}$ into equation 6.22, we can approximate that order of magnitude $\mathcal{O}(\tau) \approx 1e-10 J/m$.

We used a log-uniform prior distribution for the tension τ. This is a uniform

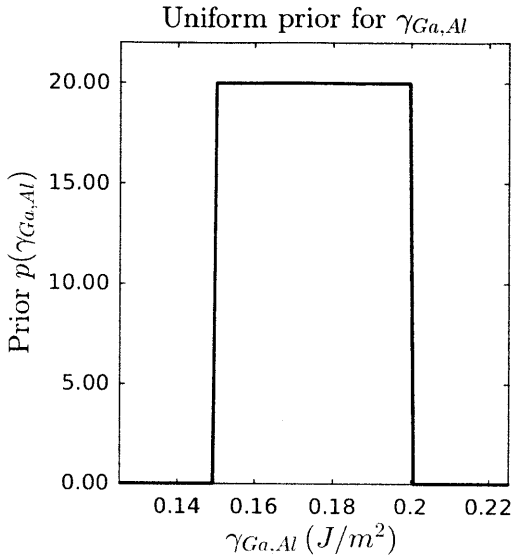

Figure 6-2: Prior distribution for the gallium-aluminum interface energy $\gamma_{Ga,Al}$.

distribution on the logarithm of τ.

$$\log(\tau) \sim \mathcal{U}(a, b) \tag{6.23}$$

$$p(\log(\tau)) = \begin{cases} \frac{1}{b-a}, & a < \log(\tau) < b \\ 0, & \text{Otherwise} \end{cases} \tag{6.24}$$

Here, a and b are the upper and lower limits of $\log(\tau)$. This distribution is a good prior distribution for variables that can vary over a large range of values. It allows us to constrain the values of τ considered, while assigning equal probability to each decade in the range specified. We have constrained τ in the range $[3.7e-11, 2.7e-10]\, J/m$. The probability density function for τ for these constraints is given by the expression

$$p(\tau) = \begin{cases} 0.5/\tau, & 3.7e-11\, J/m < \tau < 2.7e-10\, J/m \\ 0, & \text{Otherwise.} \end{cases} \tag{6.25}$$

The probability density functions for $\log(\tau)$ and τ are shown in figures 6-3(a) and (b)

respectively. We can see that the log-uniform prior assigns higher probability density to lower values of τ.

We assigned a log-uniform prior distributions to the thickness δ, which is constrained in the range $[13.3, 29.9]$Å. The probability density functions for $\log(\delta)$ and δ are shown in figures 6-4(a) and (b) respectively.

$$p(\delta) = \begin{cases} 1.25/\delta, & 13.3\text{Å} < \delta < 29.9\text{Å} \\ 0, & \text{Otherwise} \end{cases} \tag{6.26}$$

We used an improper log-uniform prior distribution for the baseline mobility $\mathcal{M}$. Like the prior distributions for δ and τ, this is a uniform distribution on the logarithm of the baseline mobility $\mathcal{M}$. However, unlike δ and τ, there are no constraints to the range of values that $\mathcal{M}$ can take. As a result, we know the PDF of $\mathcal{M}$ only up to a proportionality constant.

$$p(\log(\mathcal{M})) \propto 1 \tag{6.27}$$

$$p(\mathcal{M}) \propto 1/\mathcal{M} \tag{6.28}$$

We chose to use an improper distribution for $\mathcal{M}$ for two reasons:

- We do not have any information to make *a-priori* estimates of $\mathcal{M}$. Therefore, we would like to have a prior distribution which is as broad as possible.
- It is very inexpensive to explore a large range of values of $\mathcal{M}$. Changing $\mathcal{M}$ linearly rescales time. In this study, we have performed all simulations at $\mathcal{M} = 1\text{Å}^4/eVs = 6.242e-22m^4/Js$. Velocities at other values of $\mathcal{M}$ were calculated by rescaling time in the velocity calculation.

6.3 Posterior

To calculate the posterior, we ran simulations over a $5 \times 7 \times 7$ grid in the $(\gamma_{Ga,Al}, \delta, \tau)$ space. $\gamma_{Ga,Al}$ was sampled at 5 uniformly distributed points in the range $[0.15\ J/m^2, 0.2\ J/m^2]$.

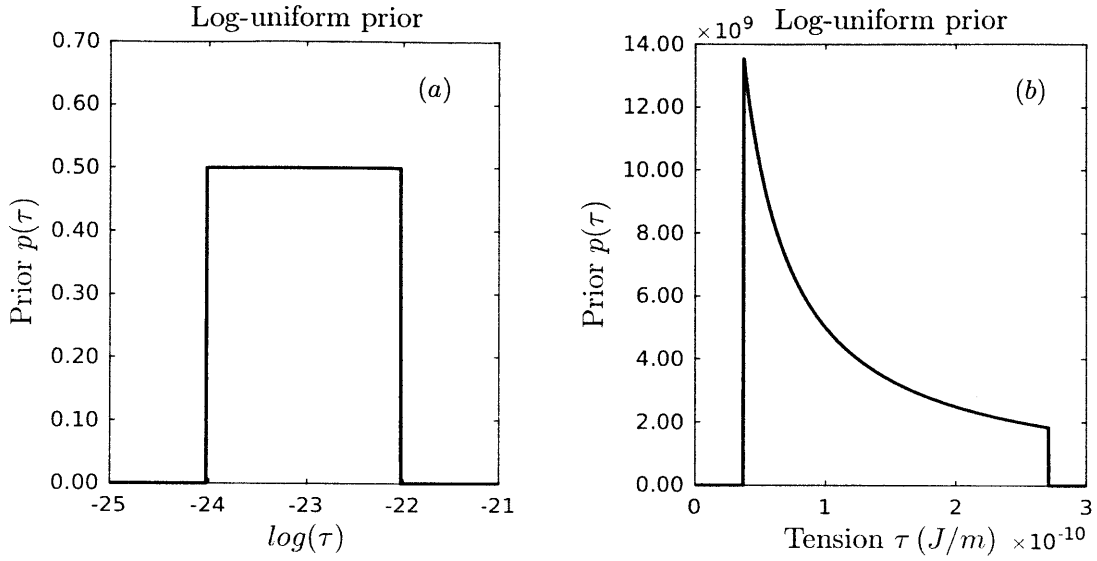

Figure 6-3: Log-uniform prior distribution for tension τ. The log-uniform prior assigns equal probability to each decade in the range of values that have non-zero probability.

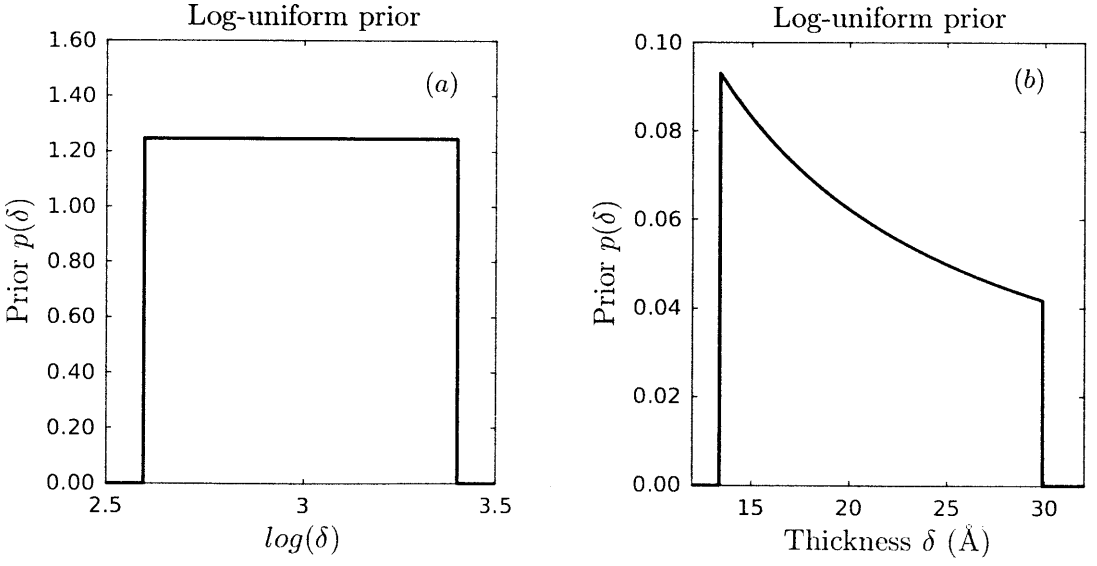

Figure 6-4: Log-uniform prior distribution for the thickness δ. The log-uniform prior assigns equal probability to each decade in the range of values that have non-zero probability.

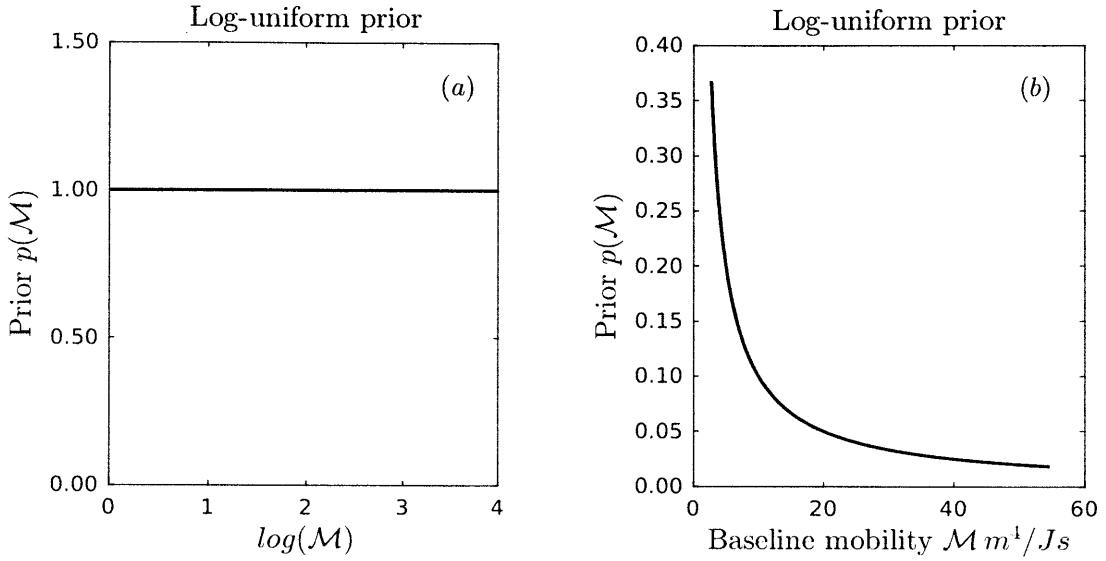

Figure 6-5: Improper log-uniform distribution for the baseline mobility $\mathcal{M}$. The probability distribution is known only to a multiplicative constant. The probability distribution assigns the same probability to each decade in $\mathcal{M}$.

δ was sampled at 7 *logarithmically* distributed points in the range [13.3Å, 29.9Å]. Similarly, τ was sampled at 7 logarithmically distributed points in the range $[3.7e-11\ J/m, 2.7e-10\ J/m]$. By sampling δ and τ with logarithmically distributed points, we assign eqal prior probability to each simulation. At each $(\gamma_{Ga,Al}, \delta, \tau)$, permeation of gallium was simulated through all 17 grain boundaries using the Cahn-Hilliard code, and the permeation speeds were calculated. All computations were carried out with a baseline mobility $\mathcal{M} = 1\text{Å}^4/eVs = 6.242e-22m^4/Js$.

We found that the velocities predicted by the Cahn-Hilliard code varied from $0\mu m/s$ to $3.28e-8\mu m/s$. In comparison, Hugo and Hoagland observed permeation velocities which varied from $0\mu m/s$ to $12.7\mu m/s$. This suggests that the value of the baseline mobility $\mathcal{M}$ is larger than $6.242e-22m^4/Js$. Therefore, we calculated the posterior on a *four* dimensional grid, consisting of the original $5 \times 7 \times 7$ grid in the $(\gamma_{Ga,Al}, \delta, \tau)$ space, plus an additional dimension for $\mathcal{M}$. We used a dense, logarithmically distributed grid for $\mathcal{M}$ in the range $[6.242 \times 10^{-16} - 6.242 \times 10^{-13}]\, m^4/Js$.

The posterior marginal of $p(\mathcal{M}|\mathcal{D})$ is calculated as

$$p(\mathcal{M}|\mathcal{D}) = \iiint p(\gamma_{Ga,Al}, \delta, \tau, \mathcal{M}|\mathcal{D}) d\gamma_{Ga,Al} d\delta d\tau \tag{6.29}$$

$$\propto \iiint p(\mathcal{D}|\gamma_{Ga,Al}, \delta, \tau, \mathcal{M}) p(\gamma_{Ga,Al}, \delta, \tau, \mathcal{M}) d\gamma_{Ga,Al} d\delta d\tau \tag{6.30}$$

$$\propto \iiint \left[\left[\left[p(\mathcal{D}|\gamma_{Ga,Al}, \delta, \tau, \mathcal{M}) p(\mathcal{M}) \right] p(\gamma_{Ga,Al}) d\gamma_{Ga,Al} \right] p(\delta) d\delta \right] p(\tau) d\tau. \tag{6.31}$$

Because we have used logarithmically distributed grids for δ, τ, and $\mathcal{M}$, the prior probability mass $p(\theta)d\theta$ for each point in the four dimensional grid is the same. Hence, the integral in 6.31 reduces to a summation. The posterior marginal is shown in figure 6-6. We can see that the posterior PDF of $\mathcal{M}$ peaks at $\sim 2.3 \times 10^{-14} m^4/Js$.

To obtain the posterior marginal of $(\gamma_{Ga,Al}, \delta, \tau)$, we marginalized out $\mathcal{M}$ from the four dimensional posterior calculation.

$$p(\gamma_{Ga,Al}, \delta, \tau|\mathcal{D}) = \int p(\gamma_{Ga,Al}, \delta, \tau, \mathcal{M}|\mathcal{D}) d\mathcal{M} \tag{6.32}$$

Figures 6-7 - 6-11 show the three dimensional posterior marginal $p(\gamma_{Ga,Al}, \delta, \tau|\mathcal{D})$. Each figure shows the posterior marginal conditioned at a one of the five values of $\gamma_{Ga,Al}$ sampled. We can see that there is a peak in the posterior distribution at $\gamma_{Ga,Al} = 0.175\, J/m^2$, $\delta = 22.8$Å, $\tau = 1.4e-10 J/m$. In figures 6-13, we have shown the permeation of gallium through grain boundary 32 at these values of $\gamma_{Ga,Al}$, δ, and τ. Figure 6-12 shows the corresponding wetting map $\beta(\mathbf{x})$.

We can see from these figures that the mechanism for the permeation of gallium through aluminum grain boundaries is front propagation. The gallium front moves through the aluminum grain boundary like a taut string, without leaving behind any islands of unpermeated aluminum. The front is able to wet all the obstacles in the wetting map $\beta(\mathbf{x})$ because the obstacles are small and disconnected. The lowest value of $\beta(\mathbf{x}) = -0.32\, J/m^2$, as compared to the largest value, $\beta(\mathbf{x}) = 0.59\, J/m^2$. Hence, it is energetically favorable for the gallium to wet the obstacles and the paths, instead of just the paths.

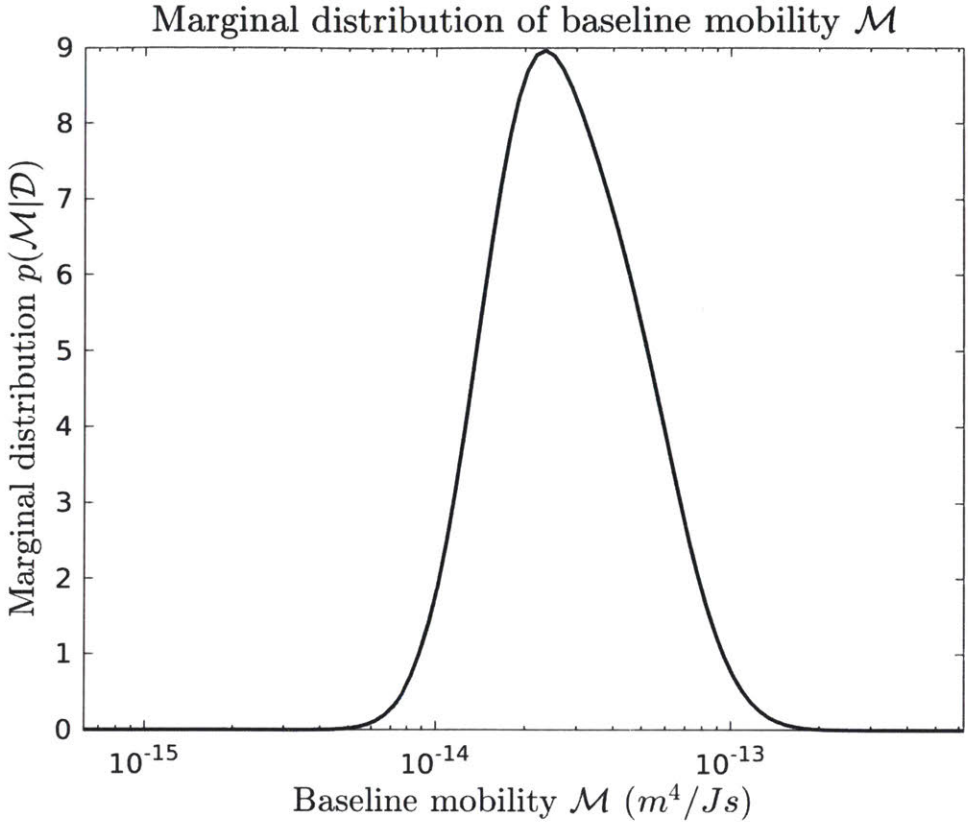

Figure 6-6: Posterior marginal for the baseline mobility $\mathcal{M}$. The posterior marginal has a single peak at $\mathcal{M} = 2.3 \times 10^{-14} m^4/Js$.

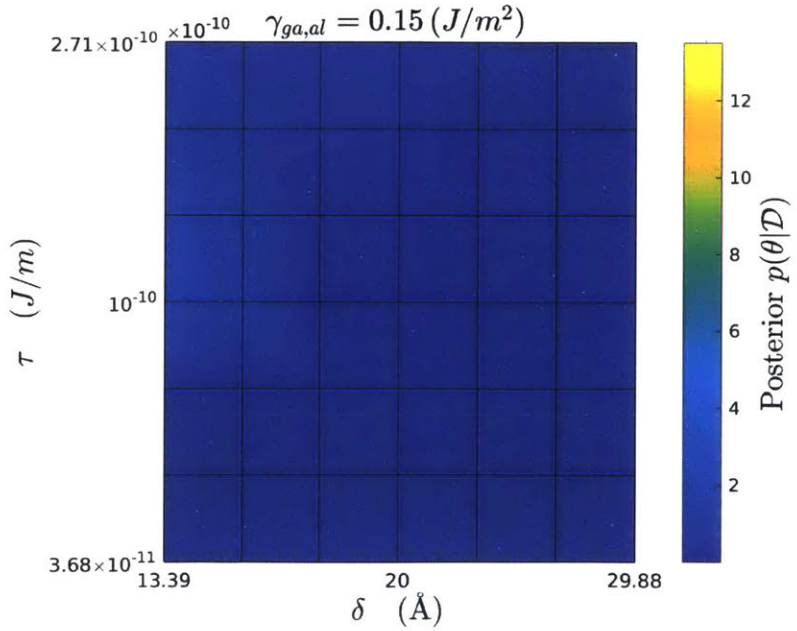

Figure 6-7: Posterior marginal for $(\gamma_{Ga,Al}, \delta, \tau)$, for $\gamma_{Ga,Al} = 0.15\,J/m^2$

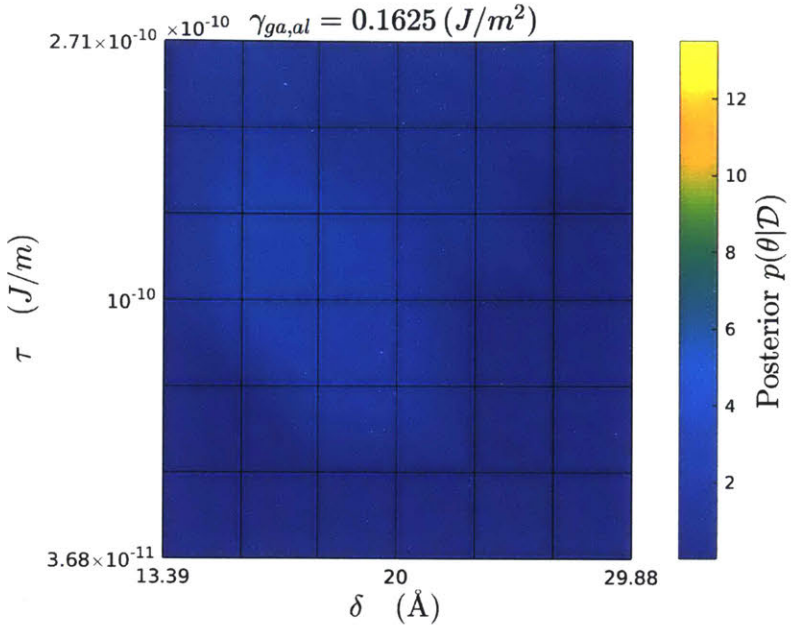

Figure 6-8: Posterior marginal for $(\gamma_{Ga,Al}, \delta, \tau)$, for $\gamma_{Ga,Al} = 0.1625\,J/m^2$

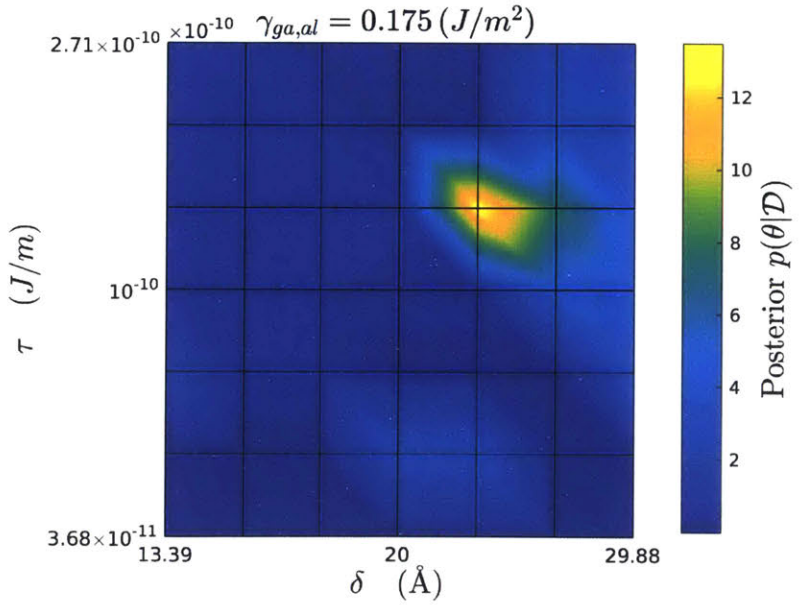

Figure 6-9: Posterior marginal for $(\gamma_{Ga,Al}, \delta, \tau)$, for $\gamma_{Ga,Al} = 0.175\,J/m^2$

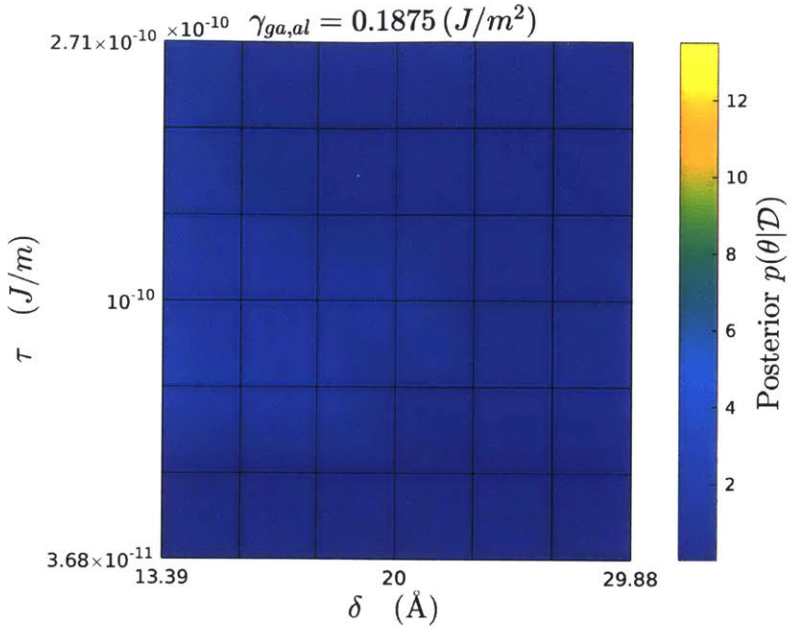

Figure 6-10: Posterior marginal for $(\gamma_{Ga,Al}, \delta, \tau)$, for $\gamma_{Ga,Al} = 0.1875\,J/m^2$

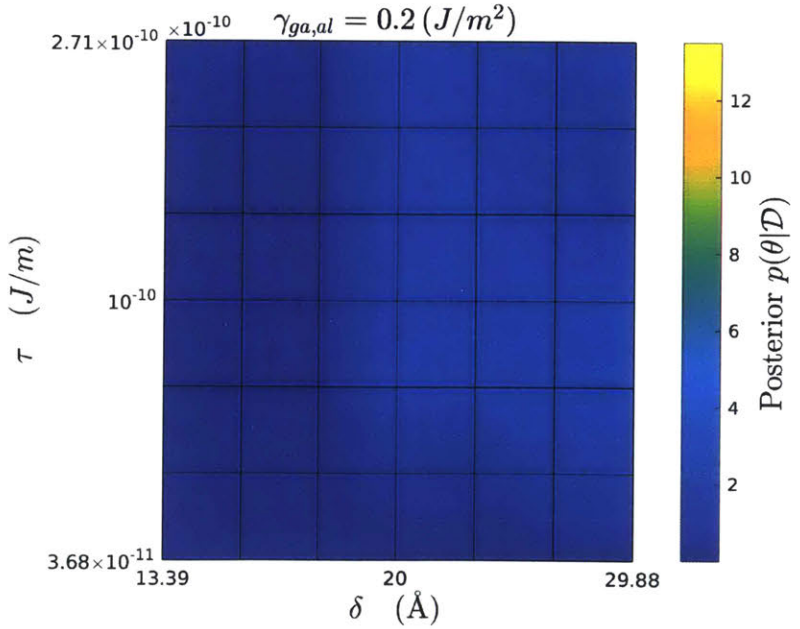

Figure 6-11: Posterior marginal for $(\gamma_{Ga,Al}, \delta, \tau)$, for $\gamma_{Ga,Al} = 0.2\,J/m^2$

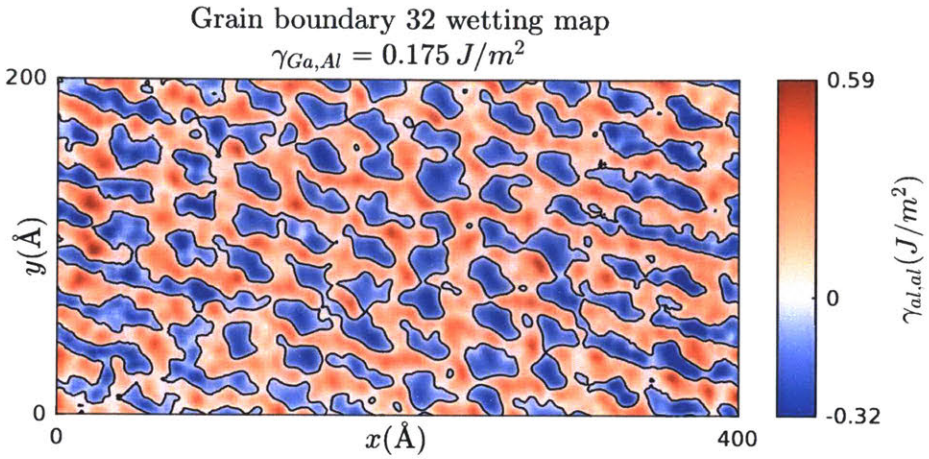

Figure 6-12: The grain boundary wetting map $\beta(\mathbf{x})$ used in figure 5-5.

6.4 Posterior predictive

We can use the Cahn-Hilliard model, and the results of the inference from the previous section to predict permeation velocities for the 17 grain boundaries used in the inference. For a given grain boundary, with an LDGBE map $\gamma_{Al,Al}(\mathbf{x})$, we can calculate the expected value of permeation speed as

$$\mathbb{E}[V_{Ga}|\mathcal{D}] = \int_{\theta} V_{Ga}(\theta, \gamma_{Al,Al}(\mathbf{x}))p(\theta|\mathcal{D})d\theta. \tag{6.33}$$

Here, θ are the parameters $(\gamma_{Ga,Al}, \delta, \tau, \mathcal{M})$, $V_{Ga}(\theta, \gamma_{Al,Al}(\mathbf{x}))$ is the permeation velocity calculated by the Cahn-Hilliard code, and $p(\theta|\mathcal{D})$ is the posterior distribution calculated in the previous section. This integral is approximated as

$$\mathbb{E}[V_{Ga}|\mathcal{D}] \approx \sum_{\theta*} V_{Ga}(\theta*, \gamma_{Al,Al}(\mathbf{x}))p(\mathcal{D}|\theta*). \tag{6.34}$$

Here, $\theta*$ is the set of all points on the four dimensional grid over which the posterior is calculated. Because of the spacing of the grid points in this grid, each point has the same prior probability $p(\theta)d\theta*$. This allows us to replace the term $p(\theta|\mathcal{D})d\theta$ in equation 6.33 with $p(\mathcal{D}|\theta*)$ in equation 6.34.

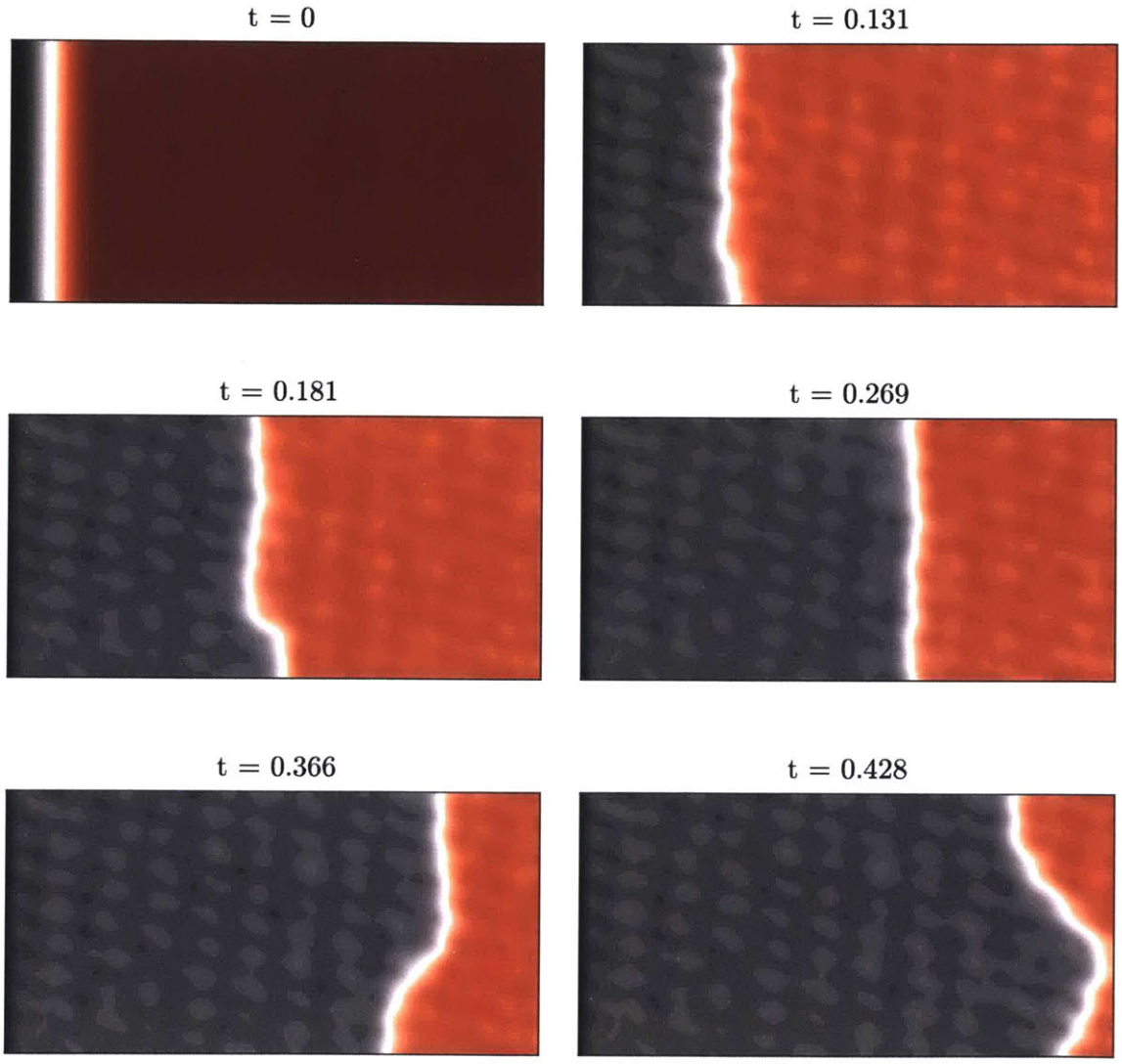

Figure 6-13: Permeation of gallium through grain boundary 32. The wetting map for this simulation is shown in figure 6-12. This simulation was performed at $\gamma_{Ga,Al} = 0.175\,J/m^2$, $\delta = 22.8\text{Å}$,$\tau = 1.4e-10\,J/m$, which corresponds to the point in the parameter space with maximum posterior density. The mechanism of permeation is front propagation.

We can also make uncertainty estimates for these predictions. There are two sources of uncertainty in the predictions. The first is from the noise model discussed in section 6.1. This noise model adds a log-normal noise to the estimated values, with mean $\mu = 0$ and $\sigma^2 = 2.25$. The second source of uncertainty arises from the uncertainty in the parameters θ. We have used a log-normal uncertainty to model this source as well, for all the justifications presented in section 6.1. To estimate the variance σ^2, we first calculated the expected value of *logarithm* of the velocity

$$\mathbb{E}[\log(V_{Ga})|\mathcal{D}] = \int_{\theta} \log(V_{Ga}) p(\theta|\mathcal{D}) d\theta \tag{6.35}$$

$$\approx \sum_{\theta*} \log(V_{Ga})(\theta*, \gamma_{Al,Al}(\mathbf{x})) p(\mathcal{D}|\theta*). \tag{6.36}$$

Next, we calculate the expected value of the *square* of the logarithm of the velocities

$$\mathbb{E}[\log(V_{Ga})^2|\mathcal{D}] = \int_{\theta} \log(V_{Ga})^2 p(\theta|\mathcal{D}) d\theta \tag{6.37}$$

$$\approx \sum_{\theta*} \log(V_{Ga})^2(\theta*, \gamma_{Al,Al}(\mathbf{x})) p(\mathcal{D}|\theta*). \tag{6.38}$$

From these two value, we can calculate the variance of the logarithm of velocity as

$$Var[\log(V_{Ga})^2|\mathcal{D}] = \mathbb{E}[\log(V_{Ga})^2|\mathcal{D}] - \mathbb{E}[\log(V_{Ga})|\mathcal{D}]^2 \tag{6.39}$$

Figure 6-14 shows these predicted values, and the uncertainty in these predictions along with the velocity values observed by Hugo and Hoagland. We can make the following observations from this figure

- The estimates, while not perfect, largely capture the trend in the velocities. Our model predicts low permeation velocities for grain boundaries with low observed permeation velocities.

- Our model under-predicts permeation velocities for grain boundaries which were observed to be permeated at high speeds. This can be seen as a 'saturation' in the estimated velocity values for large observed velocities.

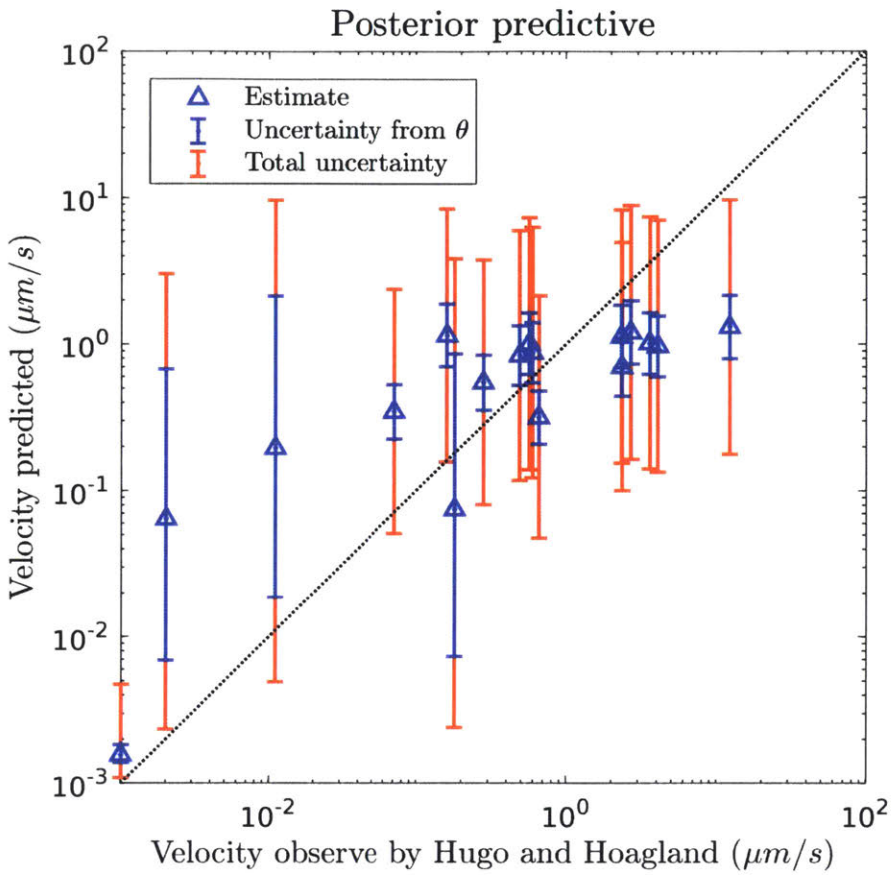

Figure 6-14: Comparison of the velocities predicted by our model and those observed by Hugo and Hoagland. We can see that the predicted velocities capture the trend in the observed velocities, but not perfectly. The uncertainty in the estimates from uncertainty in parameters θ can vary widely from grain boundaries to grain boundary.

- The magnitude of uncertainty in velocities from uncertainty in the parameters θ can vary widely. Some grain boundaries have large uncertainty in estimates from this source as compared to others. This suggests that some grain boundaries are more sensitive to the parameter $\gamma_{Ga,Al}$, δ, and τ.

Chapter 7

Discussion

The objective of this thesis was to develop a model for the gallium permeation of aluminum grain boundaries. This model was required to be able to simulate both front propagation, and diffusion and coalescence, the two potential mechanisms for gallium permeation of aluminum. We aimed to infer parameters of this model with existing experimental data collected by Hugo and Hoagland [30], and to infer the mechanism of permeation through these parameters.

Gallium permeation of aluminum has been studied both experimentally and numerically. In chapter 2, we reviewed the existing literature on gallium permeation of aluminum grain boundaries. Previous studies have shown that gallium permeation of aluminum is a complex phenomenon that is affected by factors such as grain boundary crystallography, grain boundary stress, and temperature.

In chapter 3, we introduced phase field methods as a simulation technique for this problem. We framed the gallium permeation of aluminum as a multi-phase physics problem. We showed how phase field methods simplify the simulation of gallium permeation of aluminum by using an order parameter field to represent the state of permeation of a grain boundary. Through the example of spinodal decomposition, we showed the effects of parameters of the phase field methods. We showed that we can control the thickness δ and tension τ of the interfaces between different phases by controlling parameters ϵ and α.

In chapter 4, we used previously unpublished data provided to us by Dr. Richard

Hugo to calculate grain boundary crystallography and permeation directions for the grain boundaries reported in [30]. The unpublished data consisted of Kikuchi diffraction patterns and bright field images of the grain boundaries studied. Using this data, we were able to calculate both crystallography, and permeation direction. We were able to match calculated crystallography value with those reported in [30] for 17 grain boundaries. This crystallography and permeation direction information was provided to our collaborator, Dr. Sanket S. Navale, who used atomistic simulations to calculate corresponding location dependent grain boundary energy maps $\gamma_{Al,Al}(\mathbf{x})$. We used Gaussian random fields to model and extrapolate the LDGBE maps beyond the size limits imposed by the atomistic simulations. These LDGBE maps, along with the gallium-aluminum planar interface energy $\gamma_{Ga,Al}$ were used to calculate wetting maps $\beta(\mathbf{x})$

In chapter 5, we used the Cahn-Hilliard equation with a modified potential function to simulate the gallium permeation of aluminum grain boundaries. We showed that this model could simulate both front propagation, and diffusion and coalescence permeation mechanisms through the change of parameters ϵ and α. These parameters had the effect of the changing the thickness δ and tension τ of the linear interfaces between permeated and unpermeated regions of the grain boundary.

In chapter 6, we used Bayesian inference to infer the model parameters $\gamma_{Ga,Al}$, δ, τ, and $\mathcal{M}$. We encoded our prior belief in the parameters using prior distributions. We constructed a likelihood to encode the discrepancy between velocity values predicted by our model and those observed experimentally. The posterior distribution encodes our belief in the parameters, conditioned on the observed data.

We found a peak in our posterior distribution at $\gamma_{Ga,Al} = 0.175\, J/m^2$, $\delta = 22.8$Å, $\tau = 1.4e-10\, J/m$. These values compare well with existing data in literature. Hugo and Hoagland estimated the gallium-aluminum $\gamma_{Ga,Al}$ to be greater than $0.26\, J/m^2$ [30]. We have inferred a value of $\gamma_{Ga,Al} = 0.175\, J/m^2$, which while being in the same order of magnitude, is *less* than the lower bound estimate made by Hugo and Hoagland. However, to estimate $\gamma_{Ga,Al}$, Hugo and Hoagland simply considered the grain boundary with the highest average energy which as not permeated, and set

$\gamma_{Ga,Al}$ to be half that average energy. This estimate therefore does not account for the ability of isolated obstacles to pin the gallium front. We have developed a model that can simulate this front being pinned by isolated obstacles, so it is understandable that we inferred a lower $\gamma_{Ga,Al}$ value.

There are no existing estimates for front thickness δ and front tension τ for us to compare our inferred values with. We can compare the inferred front tension $\tau = 1.4e-10\,J/m$ with the energy of dislocations in Aluminum. The strain energy per unit length of a dislocation scales as [32]

$$E = \frac{G\|b\|^2}{4\pi}\log\left(\frac{R}{r}\right) \tag{7.1}$$

$$\|b\| = \frac{a}{2}\sqrt{h^2+k^2+l^2} \tag{7.2}$$

Here, G is the shear modulus, b is the burger vector of the dislocation, a is the lattice constant, R is the size of the crystal, and r is the diameter of the dislocation. Using $G = 27\,Gpa$ for aluminum, $a = 4.046$Å, and $h,k,l \sim \mathcal{O}(1)$, $R = 1mm$, and $r = 20$Å, we get

$$E \sim 1.6e-9\,J/m \tag{7.3}$$

Our inferred value of $\tau = 1.4e-10\,J/m$ is smaller than the dislocation energy values for aluminum. This can be expected, since the gallium is a liquid at the temperatures at which these experiments are performed, and hence we would expect the gallium front to have a lower strain energy than dislocations in solid aluminum.

The inferred value of $\tau = 1.4e-10\,J/m$ strongly suggests that gallium permeates through aluminum with a front propagation mechanism. In this mechanism, the gallium front can be pinned by isolated obstacles in the aluminum grain boundary.

We used our model, and the inferred model parameters to predict permeation velocities. We compared these velocities with those observed by Hugo and Hoagland. Our predicted permeation velocities follow the same trend as the observed permeation velocities. However, our predictions are not perfect. This can be explained by a number of factors.

- We are not modeling all the parameters that affect gallium permeation of aluminum. Our model only takes into account the location dependent grain boundary energy in determining the permeation velocities. It does model factors such as grain boundary stress and grain boundary temperature in calculating the permeation velocities. These factors have been shown to affect the permeation velocities in our literature review in chapter 2. Our velocity predictions 'saturate', that is, we are under-predicting permeation velocities for grain boundaries which were permeated rapidly. It is possible that these grain boundaries were under tensile stress during experiments.

- In our model, we implicitly assume that gallium-aluminum interfaces are homogeneous, and that all gallium-aluminum interfaces have the same energy $\gamma_{Ga,Al}$. This assumption makes our inference problem tractable. Assigning different values of $\gamma_{Ga,Al}$ to different grain boundaries, or $\gamma_{Ga,Al}$ values that vary with spatial location would have made this a very high dimensional inference problem. However, it is possible that a $\gamma_{Ga,Al}$ that varies between grain boundaries can account for the discrepancy between predicted and observed permeation speeds.

Bibliography

[1] Mike P Allen and Dominic J Tildesley. *Computer simulation of liquids*. Oxford university press, 1989.

[2] Samuel M Allen and John W Cahn. Coherent and incoherent equilibria in iron-rich iron-aluminum alloys. *Acta Metallurgica*, 23(9):1017–1026, 1975.

[3] Samuel M Allen and John W Cahn. A microscopic theory for antiphase boundary motion and its application to antiphase domain coarsening. *Acta Metallurgica*, 27(6):1085–1095, 1979.

[4] KE Barrett, KD Ellis, CR Glass, GA Roth, MP Teague, and J Johns. Critical processes and parameters in the development of accident tolerant fuels drop-in capsule irradiation tests. *Nuclear Engineering and Design*, 294:38–51, 2015.

[5] S. Bechtle, M. Kumar, B.P. Somerday, M.E. Launey, and R.O. Ritchie. Grain-boundary engineering markedly reduces susceptibility to intergranular hydrogen embrittlement in metallic materials. *Acta Materialia*, 57(14):4148 – 4157, 2009.

[6] Sudipta Biswas, Daniel Schwen, Jogender Singh, and Vikas Tomar. A study of the evolution of microstructure and consolidation kinetics during sintering using a phase field modeling based approach. *Extreme Mechanics Letters*, 7:78–89, 2016.

[7] William J Boettinger and James A Warren. The phase-field method: simulation of alloy dendritic solidification during recalescence. *Metallurgical and materials transactions A*, 27(3):657–669, 1996.

[8] William J Boettinger, James A Warren, Christoph Beckermann, and Alain Karma. Phase-field simulation of solidification. *Annual review of materials research*, 32(1):163–194, 2002.

[9] Chandu Bolisetti, Justin Coleman, Mohamed Talaat, Philip Hashimoto, and Bentley Harwood. Advanced seismic fragility modeling using nonlinear soil-structure interaction analysis. Technical report, Idaho National Laboratory (INL), Idaho Falls, ID (United States), 2015.

[10] Walter Bollmann. *Crystal defects and crystalline interfaces*. Springer Science & Business Media, 2012.

[11] Jean Bragard, Alain Karma, Youngyih H Lee, and Mathis Plapp. Linking phase-field and atomistic simulations to model dendritic solidification in highly undercooled melts. *Interface Science*, 10(2):121–136, 2002.

[12] John W Cahn. On spinodal decomposition. *Acta metallurgica*, 9(9):795–801, 1961.

[13] John W Cahn. On spinodal decomposition in cubic crystals. *Acta metallurgica*, 10(3):179–183, 1962.

[14] John W Cahn and John E Hilliard. Free energy of a nonuniform system. i. interfacial free energy. *The Journal of chemical physics*, 28(2):258–267, 1958.

[15] JW Cahn and SM Allen. A microscopic theory for domain wall motion and its experimental verification in fe-al alloy domain growth kinetics. *Le Journal de Physique Colloques*, 38(C7):C7–51, 1977.

[16] Long-Qing Chen. Phase-field models for microstructure evolution. *Annual review of materials research*, 32(1):113–140, 2002.

[17] Pak-Kon Choi, Noriyuki Takahashi, and Makoto Takahashi. Gallium penetration into aluminum alloys detected using laser-generated rayleigh waves. *Materials Science and Engineering: A*, 442(1):187–190, 2006.

[18] Charles M Elliott and Zheng Songmu. On the cahn-hilliard equation. *Archive for Rational Mechanics and Analysis*, 96(4):339–357, 1986.

[19] David J Eyre. Unconditionally gradient stable time marching the cahn-hilliard equation. *MRS Online Proceedings Library Archive*, 529, 1998.

[20] Danan Fan and Long-Qing Chen. Topological evolution during coupled grain growth and ostwald ripening in volume-conserved 2-d two-phase polycrystals. *Acta materialia*, 45(10):4145–4154, 1997.

[21] Danan Fan, Chengwei Geng, and Long-Qing Chen. Computer simulation of topological evolution in 2-d grain growth using a continuum diffuse-interface field model. *Acta materialia*, 45(3):1115–1126, 1997.

[22] Kyle A Gamble, Anthony F Williams, Paul K Chan, and Diane Wowk. A feasibility study on the use of the moose computational framework to simulate three-dimensional deformation of candu reactor fuel elements. *Nuclear Engineering and Design*, 293:385–394, 2015.

[23] Derek Gaston, Chris Newman, Glen Hansen, and Damien Lebrun-Grandie. Moose: A parallel computational framework for coupled systems of nonlinear equations. *Nuclear Engineering and Design*, 239(10):1768–1778, 2009.

[24] Derek R Gaston, Cody J Permann, John W Peterson, Andrew E Slaughter, David Andrš, Yaqi Wang, Michael P Short, Danielle M Perez, Michael R Tonks, Javier Ortensi, et al. Physics-based multiscale coupling for full core nuclear reactor simulation. *Annals of Nuclear Energy*, 84:45–54, 2015.

[25] JM Haile. A primer on the computer simulation of atomic fluids by molecular dynamics. *Script, Clemson University, Clemson*, 1980.

[26] P Heilmann, WAT Clark, and DA Rigney. Computerized method to determine crystal orientations from kikuchi patterns. *Ultramicroscopy*, 9(4):365–371, 1982.

[27] Pierre C Hohenberg and Bertrand I Halperin. Theory of dynamic critical phenomena. *Reviews of Modern Physics*, 49(3):435, 1977.

[28] RC Hugo and RG Hoagland. In-situ tem observation of aluminum embrittlement by liquid gallium. *Scripta materialia*, 38(3):523–529, 1998.

[29] RC Hugo and RG Hoagland. Gallium penetration of aluminum: in-situ tem observations at the penetration front. *Scripta materialia*, 41(12):1341–1346, 1999.

[30] R.C. Hugo and R.G. Hoagland. The kinetics of gallium penetration into aluminum grain boundaries—in situ {TEM} observations and atomistic models. *Acta Materialia*, 48(8):1949 – 1957, 2000.

[31] D. Hull and D.J. Bacon. Chapter 9 - dislocation arrays and crystal boundaries. In D. Hull, , and D.J. Bacon, editors, *Introduction to Dislocations (Fifth Edition)*, pages 171 – 204. Butterworth-Heinemann, Oxford, fifth edition edition, 2011.

[32] Derek Hull and David J Bacon. *Introduction to dislocations*. Butterworth-Heinemann, 2001.

[33] NL Johnson, S Kotz, and N Balakrishnan. 14: lognormal distributions, continuous univariate distributions. vol. 1, 1994.

[34] AM Jokisaari, PW Voorhees, Jonathan E Guyer, J Warren, and OG Heinonen. Benchmark problems for numerical implementations of phase field models. *Computational Materials Science*, 126:139–151, 2017.

[35] Alain Karma and Wouter-Jan Rappel. Phase-field model of dendritic sidebranching with thermal noise. *Physical review E*, 60(4):3614, 1999.

[36] Ryo Kobayashi. Modeling and numerical simulations of dendritic crystal growth. *Physica D: Nonlinear Phenomena*, 63(3-4):410–423, 1993.

[37] CE Krill Iii and L-Q Chen. Computer simulation of 3-d grain growth using a phase-field model. *Acta materialia*, 50(12):3059–3075, 2002.

[38] Hiroaki Kurishita, Shunichi Kuba, Haruyoshi Kubo, and Hideo Yoshinaga. Misorientation dependence of grain boundary fracture in molybdenum bicrystals with various< 110> twist boundaries. *Transactions of the Japan institute of metals*, 26(5):332–340, 1985.

[39] J. S. Langer, M. Bar-on, and Harold D. Miller. New computational method in the theory of spinodal decomposition. *Phys. Rev. A*, 11:1417–1429, Apr 1975.

[40] E.M. Lehockey and G. Palumbo. On the creep behaviour of grain boundary engineered nickel 1. *Materials Science and Engineering: A*, 237(2):168 – 172, 1997.

[41] L.C. Lim and T. Watanabe. Fracture toughness and brittle-ductile transition controlled by grain boundary character distribution (gbcd) in polycrystals. *Acta Metallurgica et Materialia*, 38(12):2507 – 2516, 1990.

[42] W Ludwig and D Bellet. Penetration of liquid gallium into the grain boundaries of aluminium: a synchrotron radiation microtomographic investigation. *Materials Science and Engineering: A*, 281(1):198–203, 2000.

[43] Mel I Mendelson. Average grain size in polycrystalline ceramics. *Journal of the American Ceramic Society*, 52(8):443–446, 1969.

[44] Ho-Seok Nam and David J. Srolovitz. Molecular dynamics simulation of ga penetration along grain boundaries in al: A dislocation climb mechanism. *Phys. Rev. Lett.*, 99:025501, Jul 2007.

[45] Ho-Seok Nam and David J. Srolovitz. Effect of material properties on liquid metal embrittlement in the al–ga system. *Acta Materialia*, 57(5):1546 – 1553, 2009.

[46] Sirish Namilae, Balasubramaniam Radhakrishnan, and James R Morris. Atomistic simulation of the effect of ga on crack tip opening in al bicrystals. *Modelling and Simulation in Materials Science and Engineering*, 16(7):075001, 2008.

[47] Amy Novick-Cohen and Lee A Segel. Nonlinear aspects of the cahn-hilliard equation. *Physica D: Nonlinear Phenomena*, 10(3):277–298, 1984.

[48] G Pastore, SR Novascone, RL Williamson, JD Hales, BW Spencer, and DS STAFFORD. Modelling of fuel behaviour during loss-of-coolant accidents using the bison code. In *2015 LWR Fuel Performance MeetingâĂŤTop Fuel, Zurich, Switzerland*, 2015.

[49] E Pereiro-Lopez, W Ludwig, D Bellet, and J Baruchel. Grain boundary liquid metal wetting: A synchrotron micro-radiographic investigation. *Nuclear Instruments and Methods in Physics Research Section B: Beam Interactions with Materials and Atoms*, 200:333–338, 2003.

[50] E Pereiro-López, W Ludwig, D Bellet, and P Cloetens. Nanometric intergranular liquid layer penetration in the al/ga system: An x-ray projection microscopy investigation. *Nuclear Instruments and Methods in Physics Research Section B: Beam Interactions with Materials and Atoms*, 246(1):226–231, 2006.

[51] E Pereiro-Lopez, Wolfgang Ludwig, and D Bellet. Discontinuous penetration of liquid ga into grain boundaries of al polycrystals. *Acta materialia*, 52(2):321–332, 2004.

[52] E Pereiro-Lopez, Wolfgang Ludwig, D Bellet, P Cloetens, and C Lemaignan. Direct evidence of nanometric invasionlike grain boundary penetration in the al/ga system. *Physical review letters*, 95(21):215501, 2005.

[53] Thomas Poulet, Martin Paesold, and Manolis Veveakis. Multi-physics modelling of fault mechanics using redback: a parallel open-source simulator for tightly coupled problems. *Rock Mechanics and Rock Engineering*, 50(3):733–749, 2017.

[54] Thomas Poulet and Manolis Veveakis. A viscoplastic approach for pore collapse in saturated soft rocks using redback: an open-source parallel simulator for rock mechanics with dissipative feedbacks. *Computers and Geotechnics*, 74:211–221, 2016.

[55] Nikolas Provatas and Ken Elder. *Phase-field methods in materials science and engineering*. John Wiley & Sons, 2011.

[56] Carl Edward Rasmussen. Gaussian processes for machine learning. 2006.

[57] C Roques-Carmes, M Aucouturier, and P Lacombe. The influence of testing temperature and thermal history on the intergranular embrittlement and penetration of aluminium by liquid gallium. *Metal Science Journal*, 7(1):128–132, 1973.

[58] KB Rundman and JE Hilliard. Early stages of spinodal decomposition in an aluminum-zinc alloy. *Acta metallurgica*, 15(6):1025–1033, 1967.

[59] Daniel Schwen, Larry K Aagesen, John W Peterson, and Michael R Tonks. Rapid multiphase-field model development using a modular free energy based approach with automatic differentiation in moose/marmot. *Computational Materials Science*, 132:36–45, 2017.

[60] Devinderjit Sivia and John Skilling. *Data analysis: a Bayesian tutorial*. OUP Oxford, 2006.

[61] Andrew E Slaughter, John W Peterson, Derek R Gaston, Cody J Permann, David Andrš, and Jason M Miller. Continuous integration for concurrent moose framework and application development on github. *Journal of Open Research Software*, 3(1), 2015.

[62] Antti Takala, Päivi Takala, Jukka Seppälä, and Kalle Levon. Interdiffusion and spinodal decomposition in electrically conducting polymer blends. *Polymers*, 7(8):1410–1426, 2015.

[63] Ryo Tanaka, Pak-Kon Choi, Hirokazu Koizumi, and Shin ichi Hyodo. Fast penetration of liquid gallium in polycrystalline aluminum films. *MATERIALS TRANSACTIONS*, 42(1):138–140, 2001.

[64] Lloyd N Trefethen. *Spectral methods in MATLAB*. SIAM, 2000.

[65] James A Warren and William J Boettinger. Prediction of dendritic growth and microsegregation patterns in a binary alloy using the phase-field method. *Acta Metallurgica et Materialia*, 43(2):689–703, 1995.

[66] T Watanabe, H Fujii, H Oikawa, and KI Arai. Grain boundaries in rapidly solidified and annealed fe-6.5 mass% si polycrystalline ribbons with high ductility. *Acta Metallurgica*, 37(3):941–952, 1989.

[67] T Watanabe, S Shima, and S Karashima. inembrittlement by liquid and solid metals. *TMS-AIME, Warrendale, PA*, page 161, 1984.

[68] David B Williams and C Barry Carter. The transmission electron microscope. In *Transmission electron microscopy*, pages 3–17. Springer, 1996.

[69] Olga Wodo and Baskar Ganapathysubramanian. Modeling morphology evolution during solvent-based fabrication of organic solar cells. *Computational Materials Science*, 55:113–126, 2012.